

ROBUSTNESS AND EVOLVABILITY IN SYSTEMS  
BIOLOGY AND PLECTONEME FORMATION IN DNA  
SUPERCOILING

A Dissertation

Presented to the Faculty of the Graduate School

of Cornell University

in Partial Fulfillment of the Requirements for the Degree of

Doctor of Philosophy

by

Bryan C. Daniels

August 2010

© 2010 Bryan C. Daniels  
ALL RIGHTS RESERVED

ROBUSTNESS AND EVOLVABILITY IN SYSTEMS BIOLOGY AND  
PLECTONEME FORMATION IN DNA SUPERCOILING

Bryan C. Daniels, Ph.D.

Cornell University 2010

This thesis consists of two parts: (1) an exploration of robustness and evolvability in systems biology and how they are informed by recent developments in the study of parameter sensitivity in large multiparameter models, and (2) a study of the sudden formation of plectonemes (supercoiled structures) in DNA using an elastic rod model.

Robustness and evolvability are important ideas in systems biology, representing the surprising resilience and adaptability of living organisms. The study of “sloppy models” describes the degree to which changes in parameters change the behavior of complex models, and thus has implications for how robust or evolvable a model may be with regard to perturbations in parameters. We study these connections, finding that sloppiness provides a framework for understanding why multiparameter models often seem so robust. It also explains how robustness to external conditions can be more easily arranged than one might naively expect, and allows for diversity that could increase the evolvability of a population.

When overtwisted, DNA wraps around itself (supercoils) much like a garden hose or rubber band. As a single molecule of DNA is twisted, discontinuities have recently been experimentally observed for the first time that correspond to the sudden formation of a single supercoiled structure called a plectoneme. We study the sizes of these discontinuities with an elastic rod model and a simplified phenomenological model. We use these models to make predictions about a torque

jump and length dependence that have been experimentally verified. Experiments also observe thermal hopping at the transition between states with and without a plectoneme. We then investigate the dynamics of this plectoneme nucleation, using transition state theory and the elastic rod model to predict the rate of hopping. We obtain a rate about 1000 times faster than found in experiments, and attribute the discrepancy to an underestimate by elastic theory of the height of the energy barrier that impedes the transition. Finally, we review numerical methods used to implement the elastic rod model for DNA.

## BIOGRAPHICAL SKETCH

The author was born and raised near Dayton, Ohio, was hooked on science at an early age through frequent visits to the science museum, and remembers the excitement of learning to program his first computer in BASIC. He graduated from Ohio Wesleyan University in 2005 with a BA in physics and minors in mathematics and computer science. An IGERT fellowship at Cornell fostered an interest in interdisciplinary science and complex models that has led to work on neuroscience, systems biology, and DNA supercoiling. He joined Jim Sethna's group in 2007. After graduation, he plans to think about conflict dynamics for a while as a postdoc at the Santa Fe Institute.

To my parents.

## ACKNOWLEDGMENTS

It is with pleasure that I thank a few of the people who have helped me along the way. First, I consider myself quite lucky to have had a succession of such encouraging and inspiring mentors throughout my education. In roughly chronological order, Clifton Martin, Brad Trees, Kevin Ingersent, Randy Beer, and Ilya Nemenman have each shared with me a great excitement for science. Lastly, I want to emphasize how enjoyable it has been to have Jim Sethna as my graduate advisor — though he has taught me more about doing physics than I probably realize, I think what will stick with me most is how he consistently demonstrates that good science is fun.

I have greatly enjoyed working with and learning from my colleagues in Ithaca and elsewhere, including Chris Myers, Michelle Wang, Veit Elser, Scott Forth, Maxim Sheinin, Wiet de Ronde, Andrew Mugler, Ryan Gutenkunst, YJ Chen, Ben Machta, Mark Transtrum, and the rest of the growing Sethna group. Having these interesting people around has been invigorating for me and my research.

My interest in interdisciplinary science was discovered largely through Cornell's IGERT program in nonlinear systems, and I thank John Guckenheimer and the rest of the IGERT crowd (Bret Hanlon, Amina Kinkhabwala, Jordan Atlas, to name a few) for the stimulating environment they provided.

My graduate career has been much more happy thanks to the great friends that I've shared it with. It's a list too long to write here, but if you've lived in or visited the Estate, or danced in any of the sketches, thanks for the good times. And a special thank you goes to Chloë, who magically arrived just in time to keep me sane through the thesis writing process.

Finally, I dedicate this thesis to my parents, whose unwavering love and support have been crucial to my success. Thank you.

## TABLE OF CONTENTS

Biographical Sketch . . . . .	iii
Dedication . . . . .	iv
Acknowledgements . . . . .	v
Table of Contents . . . . .	vi
List of Tables . . . . .	viii
List of Figures . . . . .	ix
<b>1 Introduction</b>	<b>1</b>
1.1 Introduction to sloppy models . . . . .	1
1.2 Introduction to DNA supercoiling . . . . .	2
1.2.1 The conservation of linking number . . . . .	4
1.2.2 DNA as an elastic rod . . . . .	6
<b>2 Sloppiness, robustness, and evolvability in systems biology</b>	<b>8</b>
2.1 Abstract . . . . .	8
2.2 Introduction . . . . .	8
2.3 Environmental robustness and sloppiness . . . . .	13
2.4 Chemotype robustness and sloppiness . . . . .	17
2.5 Robustness, evolvability, and sloppiness . . . . .	20
2.6 Conclusion . . . . .	23
<b>3 Discontinuities at the DNA supercoiling transition</b>	<b>25</b>
3.1 Abstract . . . . .	25
3.2 Introduction . . . . .	25
3.3 Free energy of stretched state . . . . .	27
3.4 Scaling of coexisting state free energy and extension . . . . .	30
3.5 Model predictions . . . . .	34
3.6 Conclusion . . . . .	36
<b>4 Nucleation at the DNA supercoiling transition</b>	<b>38</b>
4.1 Introduction . . . . .	38
4.2 Nucleation rate calculation . . . . .	39
4.2.1 Saddle point energetics . . . . .	39
4.2.2 Transition state theory: the basic idea . . . . .	41
4.2.3 Dynamics of DNA in water: the diffusion tensor . . . . .	43
4.2.4 Transition state theory: full calculation . . . . .	45
4.3 Initial results and order of magnitude checks . . . . .	49
4.3.1 Initial results . . . . .	49
4.3.2 Order of magnitude estimates of the dynamical prefactor . .	50
4.3.3 Understanding the entropic factor . . . . .	52
4.3.4 Experimental estimate of the effective free energy barrier . .	53
4.4 Possible corrections . . . . .	56
4.4.1 Including intrinsic bends . . . . .	56

4.4.2	Uncertainties in elastic constants . . . . .	63
4.5	Discussion and conclusions . . . . .	63
<b>5</b>	<b>Numerical algorithms for DNA supercoiling</b>	<b>66</b>
5.1	Introduction . . . . .	66
5.2	Calculating the energy of a DNA configuration . . . . .	66
5.3	Transition state calculations . . . . .	68
5.3.1	Including disorder . . . . .	68
5.3.2	Changing to the correct coordinates . . . . .	73
5.3.3	Other subtleties . . . . .	75
5.3.4	Finding saddle points . . . . .	76
5.4	Numerical details . . . . .	77
5.4.1	Choosing $d$ . . . . .	77
5.4.2	Correcting for renormalization of $B$ due to repulsive interaction	77
5.4.3	Deriving rotation-invariant forms for bend and twist . . . . .	80
<b>A</b>	<b>Supplementary material for Chapter 2</b>	<b>83</b>
A.1	Contents . . . . .	83
A.2	Introduction . . . . .	83
A.2.1	Hessian at best fit parameters . . . . .	83
A.2.2	Figure 2.1: Sloppiness in the mapping of chemotypes to dynatypes . . . . .	84
A.3	Environmental robustness and sloppiness . . . . .	85
A.3.1	Figure 2.2: Sloppy parameter distributions: dependence on external conditions . . . . .	85
A.3.2	KaiC phosphorylation subnetwork model . . . . .	86
A.3.3	Figure 2.3: Sloppy model eigenvalues . . . . .	91
A.4	Chemotype robustness and sloppiness . . . . .	91
A.4.1	Derivation of robustness equation . . . . .	91
A.5	Robustness, evolvability, and sloppiness . . . . .	92
A.5.1	Derivation of chemotype evolvability . . . . .	92
A.5.2	RMS dynatype evolvability . . . . .	94
A.5.3	Figure 2.4: Evolvability and robustness in a sloppy system .	95
<b>B</b>	<b>Supplementary material for Chapter 3</b>	<b>97</b>
B.1	Behavior of extended DNA with fluctuations . . . . .	97
B.2	Derivation of linear expressions for $\mathcal{F}_{\text{CS}}$ and $z_{\text{CS}}$ . . . . .	98
B.3	Self-repulsion . . . . .	99
B.4	Extra terms in the circular end-loop model . . . . .	100
B.5	Calculating entropic contributions from fluctuations in plectoneme location, length, and linking number . . . . .	103
B.6	Independence of results on entropic effects . . . . .	107
<b>References</b>		<b>108</b>

## **LIST OF TABLES**

4.1	Parameter values for nucleation rate calculation . . . . .	42
5.1	Repulsive interaction parameters . . . . .	77

## LIST OF FIGURES

1.1	Twist and writhe in a ribbon . . . . .	4
1.2	Rubber band supercoil . . . . .	6
2.1	Sloppiness in the mapping of chemotypes to dynatypes . . . . .	12
2.2	Sloppy parameter distributions: dependence on external conditions	14
2.3	Sloppy model eigenvalues . . . . .	15
2.4	Evolvability and robustness in a sloppy system . . . . .	21
3.1	Extension and torque vs. linking number . . . . .	28
3.2	Direct measurement of torque jump . . . . .	29
3.3	Coexisting state parameters vs. applied force . . . . .	32
3.4	Length- and force-dependence of discontinuities . . . . .	33
4.1	The double-well . . . . .	39
4.2	Snapshots along the transition path . . . . .	47
4.3	Unstable mode at top of barrier . . . . .	51
4.4	Bound on free energy barrier from experimental extension distribution	54
4.5	The saddle state with increasing intrinsic bend disorder . . . . .	58
4.6	Hopping rate and effective free energy barrier vs. disorder magnitude	61
4.7	Hopping rate factors vs. disorder magnitude for different sequences	62
5.1	Local basis vectors . . . . .	66
5.2	Sensitivity of saddle energy to disorder . . . . .	71
5.3	Saddle energy vs. disorder strength . . . . .	72
5.4	Choosing $d$ . . . . .	78
5.5	Extrapolation of elastic constant renormalization . . . . .	79
5.6	Checking bend and twist expressions . . . . .	82
A.1	KaiC phosphorylation subnetwork . . . . .	87
A.2	KaiC phosphorylation network: temperature-compensated output .	88
A.3	KaiC phosphorylation network: temperature-compensation mechanism . . . . .	90
B.1	Testing entropic corrections . . . . .	101

# CHAPTER 1

## INTRODUCTION

This thesis focuses on two separate subjects. First, we examine robustness and evolvability in systems biology and how they connect to ideas about parameter sensitivity and so-called “sloppiness.” Second, we tackle the problem of modeling the supercoiling transition in DNA, inspired by single-molecule experiments that recently observed nucleation of supercoiled DNA for the first time.

### 1.1 Introduction to sloppy models

Models from systems biology tend to contain large numbers of components interacting in complicated ways to perform rather simple tasks. One such example is the NGF/EGF signalling cascade, which contains 28 interacting proteins with behavior characterized by 48 parameters, and provides the function of creating a certain output protein only if a certain hormone exists at the cell surface [6]. This property of having many parameters that combine to produce a simple function is, perhaps unsurprisingly, linked to the problem of ill-constrained parameters. Large subspaces of parameter space can fit the available experimental data sufficiently well, necessitating Bayesian sampling of parameter space to fully characterize a model’s predictions given data. Furthermore, these large dynamical models typically exhibit a characteristic hierarchy of widely-varying sensitivities in different parameter directions, a property dubbed “sloppiness” [7, 6].

The ability to change parameters in some directions without changing model behavior directly suggests connections to robustness, the ability to maintain a given function under perturbations. Also, the fact that the mapping from chemical rate

parameters (“chemotype”) to model dynamics (“dynatype”) seems ubiquitously sloppy hints that the mapping from genotype to phenotype may be sloppy as well — this suggests connections to evolvability, the ability to change to a more evolutionarily advantageous behavior.

In Chapter 2, we explore these connections between sloppiness, robustness, and evolvability. We find first that sloppiness can account for the seemingly large parameter robustness found in prior systems biology studies. It can also provide an explanation for the ease with which robustness to environmental changes can be arranged. Finally, we test the evolvability of a particular systems biology model, finding that sloppiness confers a larger evolvability on populations by allowing for a large diversity in the individual parameter sets that produce the same behavior.

## 1.2 Introduction to DNA supercoiling

DNA is a long molecule that must fit inside a small space. The necessity of compactification means that the mechanical properties of DNA, coupled with topological constraints, are important factors in understanding its biological functions. Single molecule experiments are becoming increasingly proficient in measuring DNA’s behavior under biologically-relevant forces and torques. In particular, the twisting of the DNA double helix into larger structures (supercoiling) has been under focus as an important aspect of DNA behavior.

A recent experiment performed by Forth et al. has shown a novel effect in DNA supercoiling: a discontinuity in the transition from extended to partially-supercoiled DNA [27] (see Figure 3.1). Using an optical trap, as the two ends of a single molecule of DNA are pulled with a constant force and slowly twisted,

there is a sudden jump in the distance between the two ends when the supercoiled structure is formed.

Similar experiments in the past (using longer strands of DNA manipulated with magnetic tweezers) have shown the same two regimes: relatively constant extension that transitions to a linear decrease in extension as linking number is increased [69]. But no previous studies reported a jump in the extension between the straight and supercoiled states. Theories have been successful in describing both the initial parabolic decrease due to bending fluctuations [54] and the subsequent linear decrease in extension due to supercoiling [59, 13] by treating the DNA as an inextensible elastic rod. To simultaneously describe both the straight and supercoiled regime, one successful simplified model allows for phase coexistence between straight and supercoiled DNA that differ in their effective twist stiffness [49]. None of these theories, however, explicitly predict discontinuities in the transition between the two states.

It was our goal to extend these theories to understand the recently observed discontinuity in extension at the transition between the straight and the supercoiled states. We find that a simple elastic theory does predict such a jump, due to the geometric necessity of a looped end in the formation of supercoiled DNA. We predict a jump in torque at the transition, and that both jumps in torque and in extension should be dependent on the total length of DNA. The expected torque jump is then resolved experimentally, and the length dependence of the extension jump has since been verified by another experimental group [8].

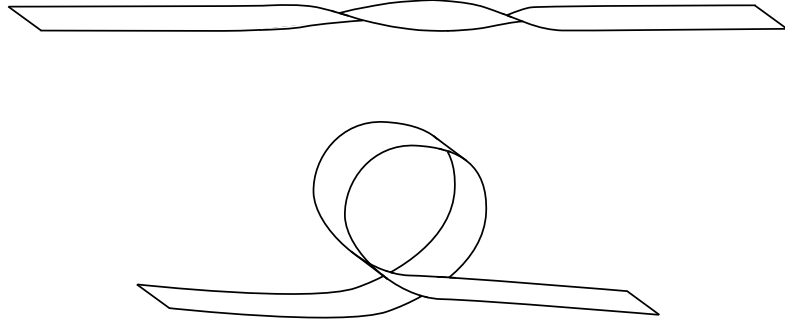


Figure 1.1: **Twist and writhe in a ribbon.** These two ribbons have the same linking number  $K = 1$ ; the top ribbon stores the linking number as twist, the bottom as writhe.

### 1.2.1 The conservation of linking number

Any circular piece of rope or ribbon has a topologically-invariant property known as the linking number. The linking number  $K$  corresponds to the number of full turns applied to the ends of an initially straight ribbon before pasting its ends together. For a linear strand, if the two ends are held with fixed orientations (and either end is not allowed to pass behind the other), the linking number is also conserved.

The linking number is conveniently partitioned into two parts known as twist (Tw) and writhe (Wr) by the White-Călugăreanu theorem [48, 23]:

$$K = \text{Tw} + \text{Wr}. \quad (1.1)$$

The twist is the intuitive number of turns around the tangent vector ‘‘backbone,’’

and the writhe keeps track of the three-dimensional curving (supercoiling) of the backbone around itself<sup>1</sup> — see Figure 1.1. Linking number can pass from twist to writhe and vice versa, but the total linking number is conserved.

The supercoiling of DNA is neatly described in this framework. Adding turns to a piece of DNA gives it torsional energy from excess twist and bending energy from writhe. Supercoiling occurs when linking number can be stored with less energy as writhe than as twist. At low linking number, all the turns will typically be stored as twist. At large enough linking number, however, supercoiling will always occur, since a writhe-storing bend will at some point have a lower energy cost than adding more twist. This phenomenon can be seen easily in a rubber band; turning the ends initially just twists the band along its axis, but eventually forms writhe-storing structures — see Figure 1.2.

Prokaryotic cells contain circular pieces of DNA (plasmids), which explicitly conserve linking number.<sup>2</sup> A typical single-molecule supercoiling experimental setup holds the two ends of a linear piece of DNA with fixed orientation; though the ends are allowed to move, linking number is conserved as long as neither end is allowed to pass behind and around the other.

DNA linking numbers are typically described as “excess” linking numbers above the relaxed B-DNA state, which contains an intrinsic number of turns in its DNA helix: one turn every  $h = 3.4$  nm. For the reader comparing the results in this thesis to previous studies, it will be useful to know that linking number densities

---

<sup>1</sup>Some authors describe writhe as the average number of crossings observed in all possible two-dimensional projections of the strand. A more abstract definition is  $1/(2\pi)$  times the total area circumscribed on the unit sphere by the filament’s unit tangent vector [48].

<sup>2</sup>Though eukaryotic DNA is linear, shorter parts of DNA can be constrained enough for linking number to be nearly conserved locally. (If it is long enough, a garden hose with free ends can still become supercoiled in the middle.) Supercoiling is known to occur here, too: one type of cancer treatment induces excess supercoiling, leading to cell death [41].

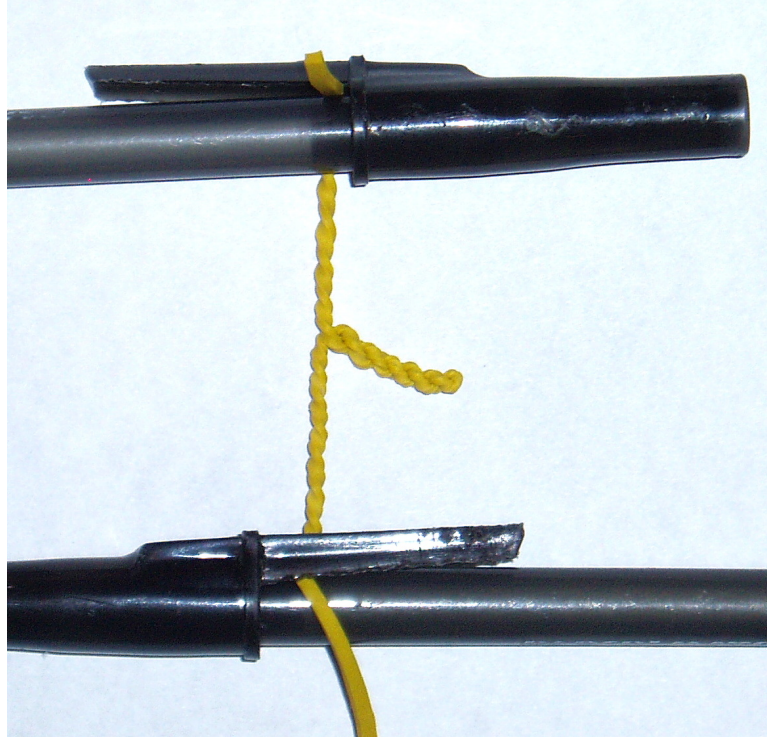


Figure 1.2: **Rubber band supercoil.** Some twist is relieved by the writhe stored in the plectonemic supercoil formed in this rubber band.

are conventionally normalized by this intrinsic linking number density:

$$\sigma = \frac{K}{L/h}. \quad (1.2)$$

### 1.2.2 DNA as an elastic rod

The physical properties of long DNA molecules have been found to be well-described by linear elastic theory (usually referred to as the “worm-like chain” model, especially in a statistical mechanics context; see, e.g., [77]). In this formulation, the DNA is modeled as a thin elastic rod, and the energy associated with deforming it from its natural relaxed state is the sum of local elastic bending, twisting, and stretching energies. The corresponding elastic constants are sensitive to experimental conditions such as the ionic concentration of the surroundings; in

our experimental setup, the bend and stretch elastic constants  $B$  and  $S$  can be measured by fitting force-extension curves, and the (renormalized) twist elastic constant  $C$  can be measured from the slope of the torque as a function of linking number. These values are listed in Table 4.1 [27]. For the low forces in the current experiment (which are in a biologically-relevant range [27]), the stretch elasticity can be safely ignored;<sup>3</sup> we thus treat our DNA as an *inextensible* elastic rod.

Parameterizing the rod by arclength  $s$ , its total elastic energy is then

$$E_{\text{elastic}} = \int_0^L ds \left[ \frac{B}{2} \beta(s)^2 + \frac{C}{2} \Gamma(s)^2 \right] \quad (1.3)$$

where  $\beta$  and  $\Gamma$  are the local bend and twist deformation angles, respectively, and  $L$  is the contour length of the rod. In order to form plectonemes, we will also need to add self-repulsion, which keeps the strand from passing through itself.

This is the model we will use to study the supercoiling transition, where a plectonemic structure is first formed as the DNA is twisted. In Chapter 3, we use the model and a more phenomenological phase coexistence picture to study the energetics of the transition and the discontinuities that arise in extension and torque at the transition. Next, in Chapter 4, we study the dynamics of nucleation of the plectonemic phase, using reaction rate theory to clarify the physical effects that control the rate of nucleation at the transition. Finally, in Chapter 5, we review the details of the numerical algorithms that we use in our calculations.

---

<sup>3</sup>At the highest force of 3.5 pN and a stretch elastic constant of 1200 pN [81], we expect a strain of 0.3%, corresponding to an energy density of 0.005 pN nm/nm. This is much smaller than the typical bending and twisting energy densities.

# CHAPTER 2

## SLOPPINESS, ROBUSTNESS, AND EVOLVABILITY IN SYSTEMS BIOLOGY

### 2.1 Abstract<sup>1</sup>

The functioning of many biochemical networks is often robust — remarkably stable under changes in external conditions and internal reaction parameters. Much recent work on robustness and evolvability has focused on the structure of neutral spaces, in which system behavior remains invariant to mutations. Recently we have shown that the collective behavior of multiparameter models is most often *sloppy*: insensitive to changes except along a few ‘stiff’ combinations of parameters, with an enormous sloppy neutral subspace. Robustness is often assumed to be an emergent evolved property, but the sloppiness natural to biochemical networks offers an alternative non-adaptive explanation. Conversely, ideas developed to study evolvability in robust systems can be usefully extended to characterize sloppy systems.

### 2.2 Introduction

Robustness and evolvability are major themes of systems biology, have been the subject of several recent books and reviews [79, 18, 37, 45, 25], and have been discussed alongside related phenomena such as canalization, homeostasis, stability, redundancy, and plasticity [39, 36, 80, 42]. Broadly construed, “robustness is

---

<sup>1</sup> This chapter and the supplemental material in Appendix A has been published in *Current Opinion in Biotechnology* with coauthors Yan-Jiun Chen, James P. Sethna, Ryan N. Gutenkunst, and Chris R. Myers [16].

the persistence of an organismal trait under perturbations” [25], which requires the specification of both traits of interest and perturbations under consideration. Recent work in systems biology has sought to distinguish between environmental robustness (e.g., temperature compensation in circadian rhythms [62, 72, 75]) and mutational robustness (e.g., parameter insensitivity in segment polarity patterning [78, 9]). Mutational robustness has a subtle relation to evolvability; while allowing survival under genetic alterations, robustness might seem to reduce the capacity for evolutionary adaptation on multigeneration time scales [45, 80].

Earlier robustness work focused on feedback and control mechanisms [3, 1, 83, 19, 28, 44]. Much recent work emphasizes neutral spaces and neutral networks: large regions in the space of sequences, parameters, or system topologies that give rise to equivalent (or nearly equivalent) phenotypic behaviors. Neutral spaces have been explored most extensively in the context of RNA secondary structure, where large neutral networks of RNA sequences (genotypes) fold into identical secondary structures (phenotypes) [65, 26, 70, 80]. More recently, similar ideas have been applied to neutral spaces underlying the robustness of gene regulatory networks [12, 11, 5], where different network topologies (genotypes) can result in identical gene expression patterns (phenotypes). Nontrivial niches in sequence spaces are also seen to emerge in molecular discrimination, a problem where neutral networks allow for biological communication in the presence of uncertainty akin to that found in engineered error-correcting codes [56]. Functional redundancies and degeneracies arise at many levels of biological organization [22], and it is an important open question as to how neutrality, redundancy, and robustness at different levels are organized and coupled across scales.

Despite these advances in understanding neutral networks connecting genotypes

in discrete spaces (e.g., sequences), much of systems biology is focused on chemical kinetic networks that are parameterized by continuous parameter spaces. Often one is interested in the steady-state behavior of a dynamical system, or in the input-output response relating only a subset of the chemical species of a network. In principle, however, one must characterize the full dynamical behavior of a network, in part because any given network may be coupled in unknown ways to other subsystems that are not included in the model. To more clearly delineate distinct levels of biological organization, we have chosen to refer the space of continuous kinetic parameters as a “chemotype” [31], and to the full dynamical response of a system as its “dynatype” (Figure 2.1). The chemotype-to-dynatype maps of interest here are embedded within larger genotype-to-phenotype maps, with chemotypes emerging from lower-level processes, and dynatypes contributing to phenotypes and ultimately fitnesses on which selection acts. Recently, there has been increased interest in characterizing the parametric sensitivity of the dynamics of biochemical network models, for two important reasons: (1) to probe system robustness by quantifying the size and shape of chemotype spaces that leave system behavior unchanged, and (2) to characterize system behavior and uncertainties for which precise values for rate constants and other kinetic parameters are typically not known.

Parameter estimation in multiparameter models has long been known to be ill-conditioned: the collective behavior usually cannot be used to infer the underlying constants. Recent work has shown that these models share striking universal features [7, 6, 32, 30], a phenomenon that we have labeled “sloppiness” (see Figures 2.1 and 2.2). Sloppiness refers to the highly anisotropic structure of parameter space, wherein the behavior of models is highly sensitive to variation along a few ‘stiff’ directions (combinations of model parameters) and more or less insensitive

to variation along a large number of ‘sloppy’ directions. A nonlinear least-squares cost function can be constructed:

$$C(\boldsymbol{\theta}) = \sum_i \frac{1}{2} \frac{(x(\boldsymbol{\theta}) - x_i)^2}{\sigma_i^2} = \sum_i \frac{1}{2} r_i^2, \quad (2.1)$$

where  $r_i = (x(\boldsymbol{\theta}) - x_i)/\sigma_i$  is the residual describing the deviation of a dynamical variable  $x$  from its measured values  $x_i$  with uncertainty  $\sigma_i$ . This cost reflects how well a model with a given set of parameters  $\boldsymbol{\theta}$  fits observed experimental data. Parametric sensitivities of the model are encoded in the Jacobian matrix  $J = \partial r_i / \partial \theta_j$ . The curvature of the cost surface about a best fit set of parameters is described by the Hessian  $H_{mn} = \partial^2 C / \partial \theta_m \partial \theta_n$  (or its approximation, the Fisher Information Matrix  $J^T J$ ). Stiff and sloppy directions are conveniently measured using an analysis of eigenvalues  $\lambda_n$  of the Hessian  $H$  (Figure 2.3); large eigenvalues correspond to stiff directions. For a broad range of multiparameter models (e.g., sixteen models drawn from the systems biology literature [32] and models from quantum Monte Carlo, radioactive decay, and polynomial fitting [82]) these eigenvalues are roughly uniformly spread over many decades, with many sloppy directions a thousand times less well determined than the stiffer, best constrained parameter combinations. Two consequences are that useful model predictions can be made even in the face of huge remaining parameter uncertainty, and conversely that direct measurements of the parameters can be inefficient in making more precise predictions [32]. Random matrix theory can be used to develop insight into the source of this type of eigenvalue spectrum and the nature of redundancies that appear to underlie sloppiness [82]. Our open-source code SloppyCell (<http://sloppycell.sourceforge.net>) provides tools for exploring parameter space of systems biology models [57].

Others have recently addressed similar questions motivated by the lack of detailed information about kinetic parameters. These include: the inference of prob-

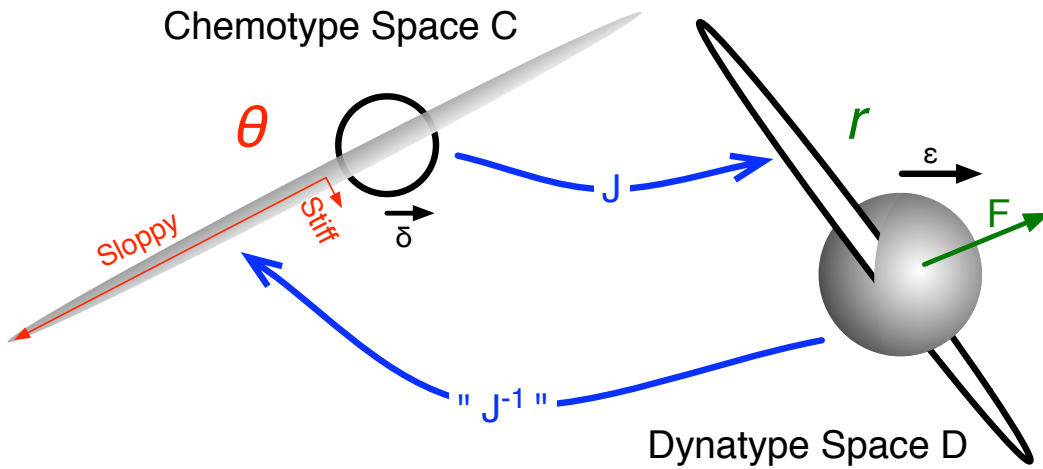


Figure 2.1: **Sloppiness in the mapping of chemotypes to dynatypes.** It is natural, at least for cellular regulation and metabolic networks, to refine the traditional dichotomy of genotype  $G$  to phenotype  $P$  by adding two intermediate levels of description,  $G \rightarrow C \rightarrow D \rightarrow P$ . Here  $C$  is the *chemotype* [31], a continuous description of the behavior in terms of chemical reaction parameters (reaction rates, barriers and prefactors, or Michaelis-Menten parameters).  $D$  is the *dynatype*, meant to describe the dynamical responses of the cell (usually the time series of all species in response to selected stimuli, often taken from experimental measurements). Mutations about a particular chemotype  $\theta$  occupy a region in chemotype space (here a circle of radius  $\delta$ ), whose image in dynatype space is given by the local Jacobian  $J$  of the mapping: mutations along stiff directions in chemotype space will yield large changes in dynatype, while mutations along sloppy directions will lead to small dynamical changes. Conversely, a population of individuals sharing nearly the same dynatype  $r$  (here a sphere of radius  $\epsilon$ ) will occupy a distorted region in chemotype space, with large variations in reaction parameters possible along sloppy directions (gray ellipse).

abilistic statements about network dynamics from probability distributions on parameter values [46]; the use of “structural kinetic modeling” to parameterize the Jacobian matrix  $J$  and thereby probe ensembles of dynamical behaviors [68, 29]; the construction of convex parameter spaces (“k-cones”) containing all allowable combinations of kinetic parameters for steady-state flux balance [24]; the use of ideas from control theory, worst-case analysis and hybrid optimization to measure the robustness of networks to simultaneous parameter variation [38], and exploration of correlated parameter uncertainties obtained via global inversion [61].

Can we connect sloppiness to robustness and evolvability? It is our contention that sloppiness — the highly anisotropic structure of neutral variation in the space of chemotypes — has important implications for how one characterizes robustness in systems biology models. In addition, insights developed in the study of robustness and evolvability suggest new and potentially useful ways of analyzing and interpreting sloppiness.

### 2.3 Environmental robustness and sloppiness

Organisms must thrive under many environmental conditions: changing temperatures, salt concentrations, pH, nutrient densities, etc. Many organisms have explicit control mechanisms to keep their internal state insensitive to these external changes — these control mechanisms (homeostasis, adaptation, etc.) have been a historical focus in the robustness literature [3, 67]. For variations in temperature, however, many organisms do not have such homeostatic control (with the exception of birds, mammals, and some plants) and must instead cope with the

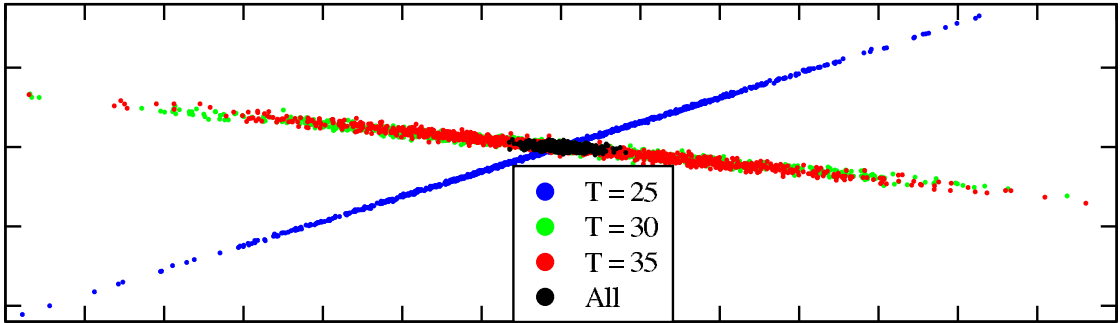


**Figure 2.2: Sloppy parameter distributions: dependence on external conditions.** Shown is a two-dimensional view of the parameter sets (free energy barriers and prefactors) that accurately predict the experimental phosphorylation dynamics [72] in a 36-parameter subnetwork of a model of circadian rhythms [75], within a harmonic approximation (see Appendix A). Shown are parameters valid at three different temperatures (colors) and valid for all temperatures simultaneously (black). The plot shows one ‘stiff’ direction in parameter space for each temperature which is tightly constrained by the data, and one ‘sloppy’ direction which has relatively large variations without change in behavior. Most of the 34 other directions in parameter space not shown are sloppy; the two-dimensional view was chosen to best align with the stiffest direction for each of the four ensembles. The black region models organisms that are robust to temperature changes in this range. The acceptable region rotates and shifts with temperature, but the sloppiness allows different temperatures to intersect (robust temperature compensation) even though all rates are strongly temperature dependent.

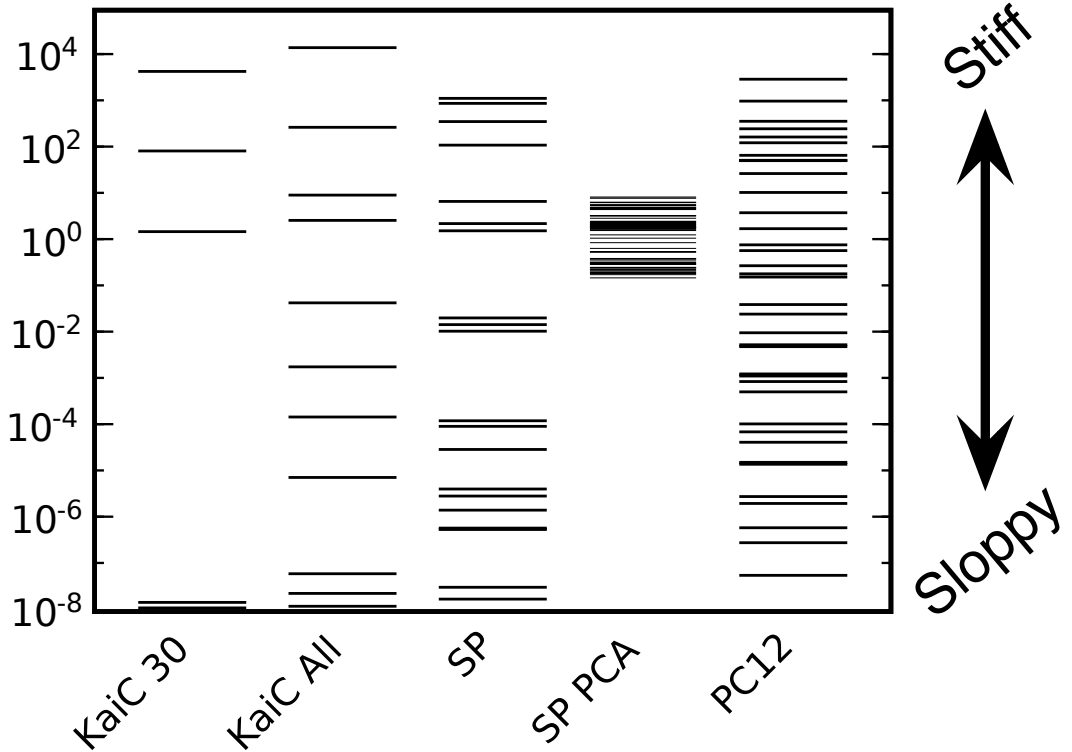


Figure 2.3: **Sloppy model eigenvalues.** Shown are the eigenvalues of the approximate Hessian  $J^T J$  for the goodness-of-fit  $C(\boldsymbol{\theta})$  (Equation 2.1) about the best fit. Large eigenvalues correspond to stiff directions; others are sloppy. Notice the enormous range on this logarithmic scale; not all eigenvalues (ranging down to  $10^{-20}$ ) are depicted.

- Columns *KaiC 30* and *KaiC All* are for the KaiC phosphorylation dynamics model (Figure 2.3), showing  $T = 30^\circ \text{ C}$  (yellow region in Figure 2.2) and simultaneous fits for all temperatures (black region). Notice that the ‘robust’ simultaneous fit has roughly one more stiff direction than the single temperatures.
- The *SP* and *SP PCA* columns are for the segment polarity model [78, 52]. *SP* is an eigenvalue analysis about one of the acceptable parameter sets, showing parameters that keep the behavior (dynatype) of the entire network preserved (time series for all components under all experimental conditions). *SP PCA* is a principal components analysis of the segment polarity ensemble that yields the wild-type phenotype, with parameters restricted to a relatively small range (roughly three decades each). Most directions in *SP* are sloppy enough to have fluctuations larger

than the sampled phenotype box in *SP PCA*; the sloppy dynatype *SP* already explains the robustness to all but a few stiff directions in parameter space. Conversely, the sensitivity of the dynatype *SP* to a few stiff directions does not preclude phenotypic robustness in those directions for *SP PCA*; the dynatype (all dynamical evolution) is far more restrictive than the phenotype (output patterning).

- *PC12* is for the EGF/NGF growth-factor signaling network [6, 32]; note that it too is sloppy. See Figure 2.4 for an analysis of evolvability and robustness for this model.

exponential Arrhenius temperature dependence of all their reaction rates by some sort of compensatory mechanism [64].

The prototypical example of temperature compensation is the 24-hour period of circadian rhythms [62]. Recent experiments have succeeded in replicating the circadian control network of cyanobacteria in the test tube using three Kai proteins, whose degree of phosphorylation oscillates with a temperature-compensated period in the range of 25 to 35° C. In addition, the phosphorylation dynamics of KaiC alone is found to be unchanged as the temperature varies in the same range [72]. This has been cited as a plausible explanation for the observed temperature compensation in the full network, presuming that all other rates are fast [75] and hence irrelevant to the period. (At least one other explanation of temperature compensation [34] also relies on constraining most rates to be irrelevant). Narrowing our focus to the KaiC phosphorylation subnetwork, however, still leaves the nontrivial task of explaining its temperature compensation mechanism, since estimated energy barriers [10] suggest that phosphorylation rates should be twice as fast at the higher temperature.

The dynamics of KaiC phosphorylation have been modeled using six phosphorylation sites and two conformational states (active and inactive) [75]. If each

of the 18 rates in this model roughly double between 25 and 35°C, can we adjust the corresponding energy barriers and prefactors such that the resulting net phosphorylation dynamics is temperature-independent?

Figure 2.2 shows a two-dimensional view of the acceptable parameter sets in the resulting 36-dimensional space of energy barriers and prefactors, explored in the harmonic approximation (see Appendix A). Notice that the region of acceptable parameters rotates and shifts as the temperature changes. Notice also that the system is sloppy: Figure 2.2 shows one stiff direction that is highly constrained by the data and one sloppy direction that is largely unconstrained. The eigenvalue analysis in Figure 2.3 confirms that most directions in parameter space are sloppy and unconstrained. This provides a natural explanation for robustness: the intersection of these large, flat hypersurfaces yields parameters that work at all temperatures.<sup>2</sup> In general, each external condition provides one constraint per stiff direction; since there are only a few stiff directions and many parameters in sloppy models, robust behavior under varying external conditions is easily arranged. Indeed, Figure 2.3 shows that the robust, temperature-independent fits for the KaiC model are themselves a sloppy system.

## 2.4 Chemotype robustness and sloppiness

In addition to robustness to environmental perturbation, biological networks are often robust to mutational perturbations; they maintain their function in the face of mutations that change one or perhaps more of their underlying rate parameters,

---

<sup>2</sup>In the particular case of KaiC, we find that successful chemotypes favor dephosphorylation in the active state and phosphorylation in the inactive state (see Appendix A), so the thermally robust solutions presumably increase the proportion of protein in the inactive state as temperature increases, compensating for the general speedup of all rates.

and thus change their location in chemotype space. Some authors have used this as a criterion for judging model plausibility [47]. The quintessential example of a system that is chemotypically robust is the *Drosophila* segment polarity gene network. Early in development, this network generates a periodic macroscopic phenotype: a pattern of gene expression across several cells that persists throughout development and guides later stages. Multiparameter models of this network [78, 9, 47, 35] find that a surprisingly large fraction of randomly chose parameter sets generate a pattern consistent with the observed patterning of three genes — the system exhibits chemotype robustness.

In the context of sloppy models, we may define chemotype robustness as the fraction of a given volume in parameter/chemotype space  $C$  that maps into a functional region of behavior/dynatype space  $D$  (Figure 2.1). This latter functional region represents behavior close to optimum (or close to that measured experimentally). For simplicity, let us consider it to be a hypersphere of radius  $\epsilon$  (i.e., a cost  $C(\boldsymbol{\theta}) = \sum r_i^2/2 < \epsilon^2/2$  in Equation 2.1); larger changes in behavior are considered significantly different, perhaps lowering the organism’s fitness. The given volume in chemotype space  $C$  might be (as for the segment polarity network) a hypercube of parameter ranges deemed reasonable, or (as a simple model of mutations) a hypersphere; let its scale be given by  $\delta$ . Our robustness is therefore the fraction of all points in the  $\delta$ -ball in  $C$  that map into the  $\epsilon$ -ball in  $D$  — in Figure 2.1 the fraction of the circle whose interior is colored gray. This fraction can be calculated (see Appendix A) and is approximately given by

$$R_c = \prod_{\lambda_n > \lambda_{crit}} \sqrt{\frac{\lambda_{crit}}{\lambda_n}}, \quad (2.2)$$

where  $\lambda_{crit} = \epsilon^2/\delta^2$ . This formula can be motivated by considering the robust subregion (gray needle intersecting the circle) to be a slab, with thickness  $\epsilon\sqrt{\lambda_n}$

along the eigendirection corresponding to each eigenvalue  $\lambda_n$ .<sup>3</sup> For sloppy directions with  $\lambda_n < \epsilon^2/\delta^2 = \lambda_{crit}$ , the slab is thicker than the circle and does not reduce the robust fraction; for each stiff direction with  $\lambda_n > \lambda_{crit}$ , the fractional volume is reduced roughly by a factor of the slab thickness  $\epsilon\sqrt{\lambda_n}$  over the sphere width  $\delta$ , leading to Equation (2.2).

In their model of segment polarity, von Dassow et al. found that approximately one in 200 randomly chosen parameter sets generated a wild-type expression pattern for three key genes [78]. This would naively seem amazing for a 48 parameter model like theirs; in an isotropic approximation, each parameter would be allowed only 6% chance of changing the wild-type pattern (since  $0.94^{48} \sim 1/200$ ). However, we have previously shown that the segment polarity model is sloppy [32]. That is, going far beyond restricting the output phenotype, the dynamical evolution of every component of the network is approximately preserved even with huge changes in parameter values: only a few stiff directions in chemotype space are needed to maintain the dynatypic (see column *SP* in Figure 2.3). Sloppiness hence provides a natural explanation for the wide variations in all but a few directions in parameter space.

The success rate of one in 200 is not nearly as striking if the dynamics is already known to be insensitive to all but perhaps four or five combinations of parameters:  $0.35^5 \times 1^{43} \sim 1/200$ . Column *SP PCA* in Figure 2.3 fleshes this picture out with a principal components analysis (PCA) of the robust region seen in von Dassow et al.’s original model, reconstructed using Ingeneue [52]. Note that these PCA eigenvalues are cut off from below by the parameter ranges chosen by the original authors for exploration (typically three decades per parameter).

---

<sup>3</sup>The cost for a small displacement of size  $\Delta\theta$  along the eigendirection  $n$  is  $\lambda_n\Delta\theta^2/2$ , which equals  $\epsilon^2/2$  when  $\Delta\theta = \pm\epsilon\sqrt{\lambda_n}$ .

While the overall scale of the dynatype sloppy-model eigenvalues in *SP* and the phenotype eigenvalues in *SP PCA* cannot be directly compared, it is clear that the vast majority of sloppy-model eigenvalues are too small to constrain the parameters within the explored region. The model is robust in these directions not because of evolution and fitness, but because the dynamics of chemical reaction networks is mathematically naturally dependent only on a few combinations of reaction parameters.

## 2.5 Robustness, evolvability, and sloppiness

Mutational robustness of systems would seem to be at odds with an ability to adapt and evolve, since robustness implies persistence of phenotype or function, which may inhibit the capacity for evolutionary change. The concept of neutral spaces has been used — most notably by Wagner and collaborators — to suggest a resolution of this apparent paradox, as demonstrated in model systems exploring various genotype-to-phenotype maps [80, 70, 12, 11]. The important insight is that neutral spaces and neutral networks enable systems to drift robustly in genotype space (i.e., without significant phenotypic change), while encountering new and different phenotypes at various points along that neutral space. This insight results from a distinction between the robustness and evolvability of any given genotype, and the robustness and evolvability of all genotypes consistent with a given phenotype [80].

Evolvability is postulated to reflect the range of possible different phenotypes that are possible under genotypic mutation. How does the sloppy connection between parameters and behavior impinge on the question of evolvability? Translating previous work on discrete genotype and phenotype spaces to the continuous

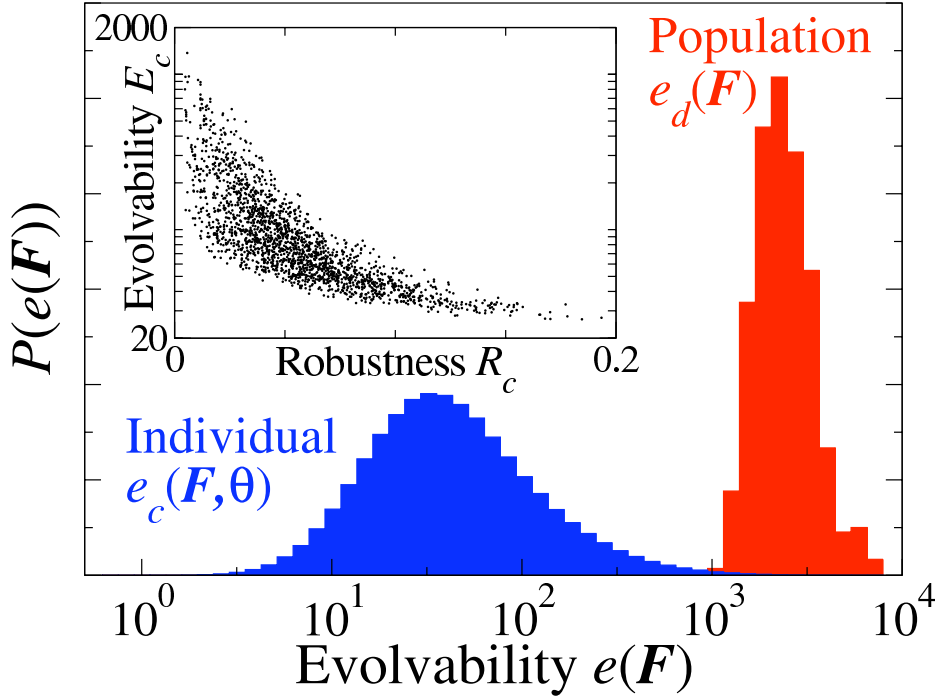


Figure 2.4: **Evolvability and robustness in a sloppy system.** Evolvability distributions, and evolvability versus robustness, for an ensemble of parameters for a model of an EGF/NGF signaling pathway fitted to experimental data in PC12 cells [32]. The histogram on the left is the distribution of individual/chemotype evolvabilities  $e_c(\mathbf{F}, \boldsymbol{\theta}_\alpha)$  (Equation 2.3), as  $\mathbf{F}$  (an evolutionary pressure in dynatype space) is randomly chosen in direction with uniform magnitude and  $\boldsymbol{\theta}_\alpha$  varies over the ensemble. The histogram on the right is the corresponding distribution of population/dynatype evolvabilities  $e_d(\mathbf{F})$  (Equation 2.4). Note that the population evolvabilities are significantly higher than the individual ones. The inset plots the RMS individual chemotype evolvability  $E_c(\boldsymbol{\theta}_\alpha)$  versus the robustness  $R_c(\boldsymbol{\theta}_\alpha)$  (Equation 2.2) for the ensemble. ( $\lambda_{crit}$  is chosen as the fourth-stiffest eigenvalue at the best fit: see Appendix A). Note that, for each individual, more robustness leads to less evolvability — individuals which rarely mutate to new forms can't evolve as readily. This need not apply to the population, insofar as we expect robust dynatypes to explore larger regions of parameter/chemotype space, and thus the ratio of dynatype to chemotype evolvability to increase with increasing robustness.

spaces of chemotypes and dynatypes is nontrivial. Since the dimensionality of the space of chemotypes is less than that of dynatypes, the volume of dynatype space accessible under changes in chemotype is zero, i.e., lies on a lower-dimensional subspace. To develop a sensible definition of evolvability in such systems, we postulate forces  $\mathbf{F}$  in dynatype space (Figure 2.1) that reflect evolutionary pressures due to changes in the environment, such that a change  $\mathbf{r}$  in dynatype leads to a change  $\mathbf{r} \cdot \mathbf{F}$  in fitness. An organism's evolvability is related to its capacity to respond to external forces through appropriate mutations in chemotype.

For a given force  $\mathbf{F}$ , the maximum fitness change among mutations of size  $\delta$  in chemotype space is given by:

$$e_c(\mathbf{F}, \boldsymbol{\theta}) = \sqrt{\mathbf{F}^T J J^T \mathbf{F}} \delta \quad (2.3)$$

which we call the chemotype evolvability distribution (see Supplemental Material). Refs. [6] and [32] generate ensembles of parameters (chemotypes) consistent with a given dynatype for an EGF/NGF signaling pathway in PC12 cells, where the dynatype is constrained to fit available experimental data. (The PC12 network is sloppy, see Figure 2.3.) Each member of such an ensemble  $\boldsymbol{\theta}_\alpha$  has a Jacobian  $J_\alpha$ . As in Ref. [80], which distinguishes between genotype and phenotype evolvability, we can distinguish between the chemotype  $e_c(\mathbf{F}, \boldsymbol{\theta}_\alpha)$  and dynatype

$$e_d(\mathbf{F}) = \max_{\boldsymbol{\theta}_\alpha} e_c(\mathbf{F}, \boldsymbol{\theta}_\alpha) \quad (2.4)$$

evolvability distributions. The first gives the distribution of adaptive responses to  $\mathbf{F}$  of individual chemotypes in a population, while the second gives the optimal response within the population. Figure 2.4 shows the chemotype and dynatype evolvability distributions, generated using the PC12 ensemble of Ref. [32] and a uniform distribution of force directions  $\mathbf{F}$  in dynatype space. Within a population sharing the same behavior, we find substantial variation of accessible behav-

ior changes, leading to a substantially larger population (dynatype) evolvability than individual (chemotype) evolvability. This echoes the finding of Wagner that phenotype evolvability is greater than genotype evolvability for RNA secondary structures [80].

It is natural to define an overall evolvability as the root-mean-square average of the evolvability distribution over a spherical distribution of environmental forces  $\mathbf{F}$  in dynatype space:

$$E_c(\boldsymbol{\theta}_\alpha) = \sqrt{\langle (e_c(\mathbf{F}, \boldsymbol{\theta}_\alpha)^2) \rangle_{\mathbf{F}}} \quad (2.5)$$

and correspondingly for the overall RMS dynatype evolvability. The inset to Figure 2.4 shows that the chemotype evolvability decreases as the chemotype robustness increases, closely analogous to Wagner’s discovery that genotype evolvability decreases as genotype robustness increases, except that his plot averages over phenotypes while ours represents variation within a dynatype. Thus we reproduce Wagner’s observation [80] that individual evolvability decreases with robustness and that population evolvability is significantly larger than individual evolvability.<sup>4</sup>

## 2.6 Conclusion

Our previous work aimed at developing predictive systems biology models in the face of parametric uncertainty has led us to formulate a theory of sloppiness in multiparameter models. The picture that emerges from this theory is of a highly anisotropic neutral space in which variation in parameters (chemotypes) can leave

---

<sup>4</sup>Unfortunately, we cannot reproduce Wagner’s final conclusion (that phenotype evolvability increases with phenotype robustness), since our ensemble (generated to match experimental behavior) is confined to the single PC12 species (dynatype).

system behavior (dynatypes) unchanged. This picture is reminiscent in many ways to the notion of neutral spaces and neutral networks that has been developed to explore the robustness and evolvability of biological systems. We have been motivated by those ideas to here reconsider sloppiness within that context, both to highlight implications of sloppiness for the study of robustness and evolvability, and to identify new methods for analyzing sloppy systems.

## CHAPTER 3

### DISCONTINUITIES AT THE DNA SUPERCOILING TRANSITION

#### 3.1 Abstract<sup>1</sup>

While slowly turning the ends of a single molecule of DNA at constant applied force, a discontinuity was recently observed at the supercoiling transition, when a small plectoneme is suddenly formed. This can be understood as an abrupt transition into a state in which stretched and plectonemic DNA coexist. We argue that there should be discontinuities in both the extension and the torque at the transition, and provide experimental evidence for both. To predict the sizes of these discontinuities and how they change with the overall length of DNA, we organize a phenomenological theory for the coexisting plectonemic state in terms of four parameters. We also test supercoiling theories, including our own elastic rod simulation, finding discrepancies with experiment that can be understood in terms of the four coexisting state parameters.

#### 3.2 Introduction

A DNA molecule, when overtwisted, can form a *plectoneme* [69, 15] (inset of Figure 3.1), a twisted supercoil structure familiar from phone cords and water hoses, which stores added turns (linking number) as ‘writhe.’ The plectoneme is not formed when the twisted DNA goes unstable (as in water hoses [74]), but in

---

<sup>1</sup> This chapter and the supplemental material in Appendix B has been published in *Physical Review E* with coauthors Scott Forth, Maxim Y. Sheinin, Michelle D. Wang, and James P. Sethna [17].

equilibrium when the free energies cross — this was vividly illustrated by a recent experiment [27] (Figure 3.2), which showed repeated transitions between the straight “stretched state” (SS, described by the worm-like chain model [51]), and a coexisting state (CS) of stretched DNA and plectoneme [49]. This transition, in addition to being both appealing and biologically important, provides an unusual opportunity for testing continuum theories of coexisting states. Can we use the well-established continuum theories of DNA elasticity to explain the newly discovered [27] jumps in behavior at the transition?

The recent experiment measures the extension (end-to-end distance) and torque of a single molecule of DNA held at constant force as it is slowly twisted [27]. A straightforward numerical implementation of the elastic rod model [23, 48, 59] for DNA in these conditions (with fluctuations incorporated via entropic repulsion [48]) leads to two quantitative predictions that are at variance with the experiment. First, the experiment showed a jump  $\Delta z$  in the extension as the plectoneme formed (Figure 3.1) that appeared unchanged for each applied force as the overall DNA length was varied from 2.2 kbp to 4.2 kbp, whereas the simulation showed a significant increase in  $\Delta z$  at the longer DNA length. Second, no discontinuity was observed in the (directly measured) filtered torque data (Figure 3.1), yet the simulation predicted a small jump.

Simulation is not understanding. Here we analyze the system theoretically, focusing on the physical causes of the behavior at the transition. We use as our framework Marko’s two-phase coexistence model [49, 50], which we generalize to incorporate extra terms that represent the interfacial energy between the plectoneme and straight regions of the DNA. We show that any model of the supercoiling transition in this parameter regime can be summarized by four force-dependent

parameters. After extracting these parameters directly from the experiments, we use them to predict the torque jump (which we then measure) and to explain why the extension jump appears length independent. Finally, we use our formulation to test various models of plectonemes, finding discrepancies mainly at small applied force.

The transition occurs at the critical linking number  $K^*$  when the two states have the same free energy  $\mathcal{F}$ , where  $\mathcal{F}$  is defined by the ensemble with constant applied force and linking number. We therefore need models for the free energy  $\mathcal{F}$  and extension  $z$  of the SS and CS.

### 3.3 Free energy of stretched state

The properties of stretched, unsupercoiled DNA are well-established. At small enough forces and torques that avoid both melting and supercoiling, DNA acts as a torsional spring with twist elastic constant  $C$  [49]:<sup>2</sup>  $\mathcal{F}_{\text{SS}}(K, L) = \frac{C}{2} \left(2\pi \frac{K}{L}\right)^2 L - F_{\text{eff}}L$ , where  $K$  is the added linking number,  $L$  is the overall (basepair) length of DNA, the effective force  $F_{\text{eff}} = F - kT\sqrt{F/B}$  [49] (see Appendix B),  $F$  is the force applied to the ends of the DNA,  $B = 43 \pm 3 \text{ nm} \times kT$  is the DNA's bending elastic constant,  $C = 89 \pm 3 \text{ nm} \times kT$ , and the thermal energy  $kT = 4.09 \text{ pN nm}$  for this experiment (at 23.5°C). Differentiating with respect to  $K$  gives the torque:  $\tau_{\text{SS}} = \frac{1}{2\pi} \frac{d\mathcal{F}_{\text{SS}}}{dK} = 2\pi C \frac{K}{L}$ . The extension of unsupercoiled DNA is shortened by thermal fluctuations, and in the relevant force regime is approximately given by

---

<sup>2</sup> As described in Ref. [54] (see also Appendix B),  $C$  is renormalized to a smaller value by bending fluctuations. We use  $C$  calculated from the torque measured in the experiment, which gives its renormalized value.

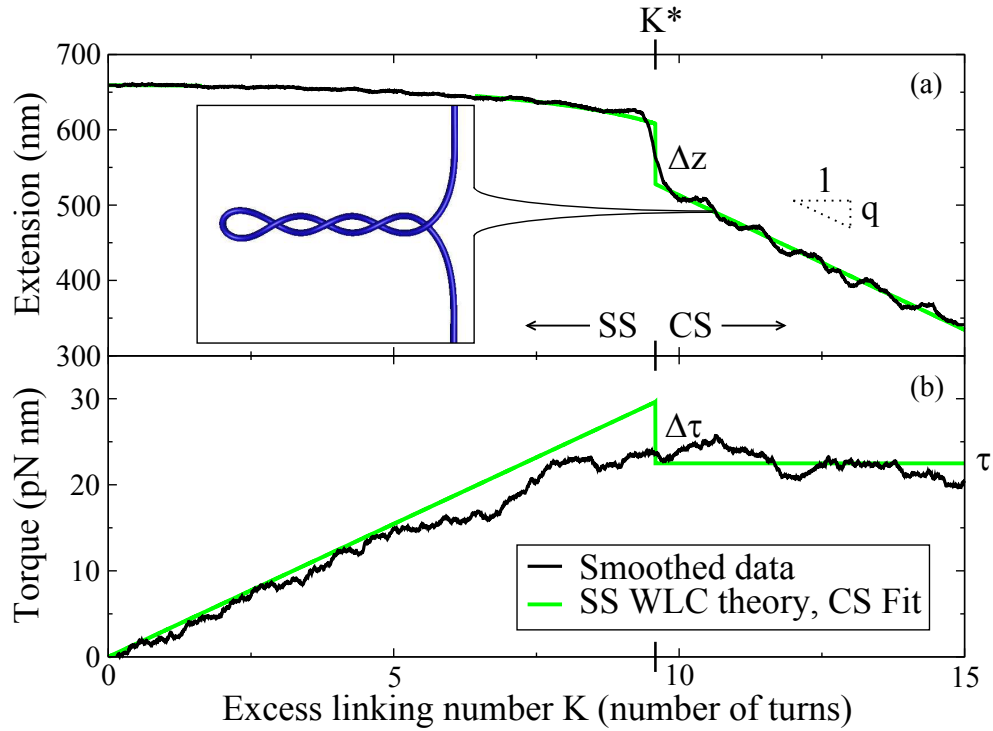


Figure 3.1: **Extension and torque vs. linking number.** Extension and torque as a function of linking number  $K$ , for  $L = 2.2$  kbp at  $F = 2$  pN. Black lines show data from Ref. [27], smoothed using a “boxcar” average of nearby points. The green (gray) lines show worm-like chain (WLC) predictions below the transition [in the unsupercoiled “stretched” state (SS)], and fits to the data after the transition [in the “coexisting” state (CS)], linear for the extension and constant for the torque. The size of the torque jump, not visible in the smoothed data, is implied by the coexisting torque  $\tau$ , the CS fit, and the transition linking number  $K^*$  in the extension data. Inset: Simulated DNA showing the CS of a plectoneme and straight DNA, ignoring thermal fluctuations. The ends are held with fixed orientation and pulled with a constant force  $F$ , here 2 pN.

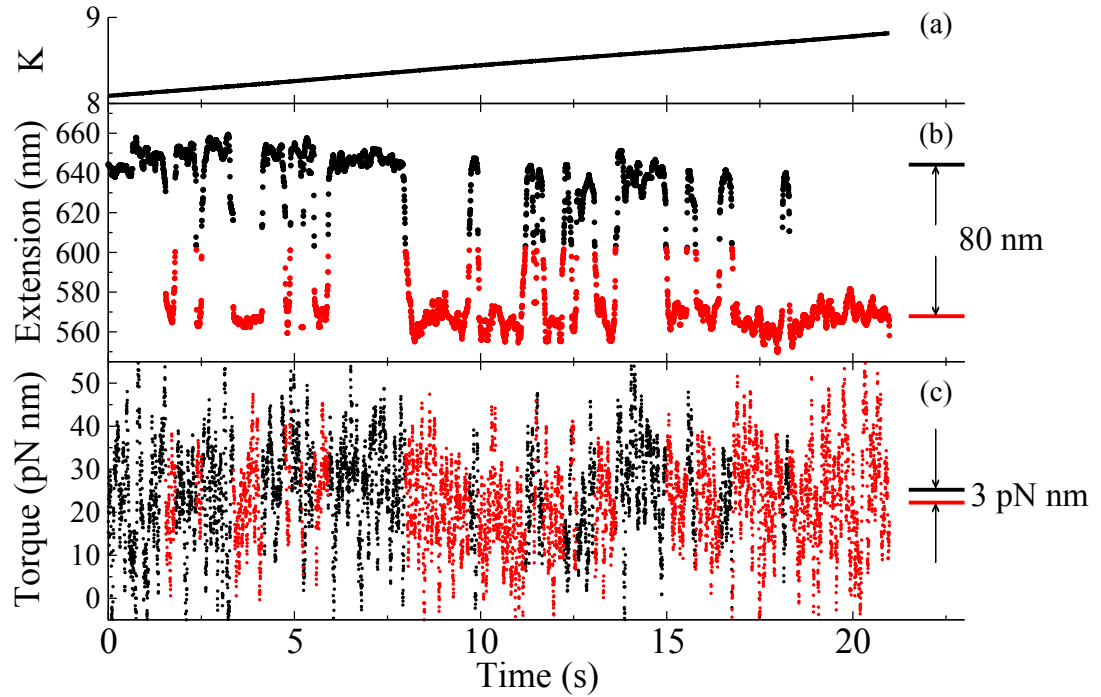


Figure 3.2: **Direct measurement of torque jump.** Directly measuring the torque jump by observing thermal hopping, for the same conditions as Figure 3.1. As linking number  $K$  is slowly increased near  $K^*$ , thermal fluctuations induce hopping between states with (CS) and without (SS) a plectoneme. Averaging over these two states gives a direct way of measuring the torque jump: analogously to a lock-in amplifier, we set a threshold in the extension signal to separately average the SS [black] and CS [red (gray)] data near the transition. Using multiple traces, we find an average torque jump of  $\Delta\tau = 2.9 \pm 0.7$  pN nm for  $L = 2.2$  kbp at  $F = 2$  pN. Additionally, this value of  $\Delta\tau$  implies (see text) that the transition should happen over a range of linking number  $K$  (a) of about 0.9 turns, as it does.

$z_{\text{SS}} = \xi(\tau_{\text{SS}})L$ , where [53]

$$\xi(\tau) = 1 - \frac{1}{2} \left[ \frac{BF}{(kT)^2} - \left( \frac{\tau}{2kT} \right)^2 - \frac{1}{32} \right]^{-1/2}. \quad (3.1)$$

### 3.4 Scaling of coexisting state free energy and extension

Since supercoiling theories must include contact forces, they are less amenable to traditional theoretical methods. Even so, many theories have been successful in predicting properties of the CS; such methods have included detailed Monte Carlo simulations [77], descriptions of the plectoneme as a simple helix [48, 59, 13], and a more phenomenological approach [49]. However, none of these theories has yet been used to predict discontinuities at the SS–CS transition. Here we connect the free energy and extension predictions from any given model to the corresponding predictions for discontinuities at the transition.

We will use the framework of two-phase coexistence adopted by Marko [49, 50] to describe the CS as consisting of two phases, each with constant free energy and extension per unit length of DNA.<sup>3</sup> Since phase coexistence leads to a linear dependence on  $K$  of the fraction of plectonemic DNA (keeping the torque fixed), in this model both  $\mathcal{F}_{\text{CS}}$  and  $z_{\text{CS}}$  are linear functions of added linking number  $K$  and length  $L$  (just as the free energy of an ice-water mixture is linear in the total energy, and the temperature remains fixed, as the ice melts). This linearity, along with the known properties of the SS, allows us to write  $\mathcal{F}_{\text{CS}}$  and  $z_{\text{CS}}$  as (see Appendix B)

$$\mathcal{F}_{\text{CS}}(K, L) = \mathcal{F}_0 + 2\pi\tau K - \left( \frac{\tau^2}{2C} + F_{\text{eff}} \right) L; \quad (3.2)$$

$$z_{\text{CS}}(K, L) = -z_0 - qK + \left( \xi(\tau) + \frac{\tau}{2\pi C} q \right) L, \quad (3.3)$$

---

<sup>3</sup> The language of phase coexistence is approximate in that the finite barrier to nucleation in one-dimensional systems precludes a true (sharp) phase transition.

where  $q$  is the slope of extension versus linking number and  $\tau$  is the CS torque. That is,  $\mathcal{F}_{\text{CS}}$  and  $z_{\text{CS}}$  are specified by four force-dependent values: their slopes with respect to  $K$  ( $\tau$  and  $q$ ), which describe how the plectonemic phase coexists with the stretched phase; and  $K = L = 0$  offsets ( $\mathcal{F}_0$  and  $z_0$ ), which describe the extra free energy and extension necessary to form the interface between the phases — the end loop and tails of the plectoneme.

The experimental observables can then be written in terms of these four values. Easiest are  $\tau$  and  $q$ , which are directly measured. Next, the linking number  $K^*$  at the transition is found by equating the CS free energy with that of the SS:  $\mathcal{F}_{\text{CS}}(K^*, L) = \mathcal{F}_{\text{SS}}(K^*, L)$  implies

$$K^* = \frac{L}{2\pi C}(\tau + \Delta\tau), \text{ with } \Delta\tau = \sqrt{\frac{2C}{L}\mathcal{F}_0}, \quad (3.4)$$

where  $\Delta\tau$  is the jump in the torque at the transition. Lastly, inserting  $K^*$  from Eq. (3.4) into Eq. (3.3), we find the change in extension at the transition:

$$\Delta z = z_0 + q\sqrt{\frac{L\mathcal{F}_0}{2\pi^2 C}} - L\left(\xi(\tau) - \xi(\tau + \sqrt{2C\mathcal{F}_0/L})\right). \quad (3.5)$$

To additionally include entropic effects, we can write  $\mathcal{F}_0 = \mu - TS$ , where  $\mu$  is the energy cost for the end-loop and tails, and  $S$  is the entropy coming from fluctuations in the location, length, and linking number of the plectoneme. Using an initial calculation of  $S$  that includes these effects (in preparation; see Appendix B), we find that  $S$  varies logarithmically with  $L$ , and that setting  $S = 0$  is a good approximation except when  $L$  changes by large factors.

Given experimental data ( $\tau$ ,  $q$ ,  $K^*$ , and  $\Delta z$ ), we can solve for the four CS parameters. The results from Ref. [27] are shown as circles in Figure 3.3 for the two overall DNA lengths tested. If we assume that the DNA is homogeneous, we expect the results to be independent of  $L$  (except for a logarithmic entropic

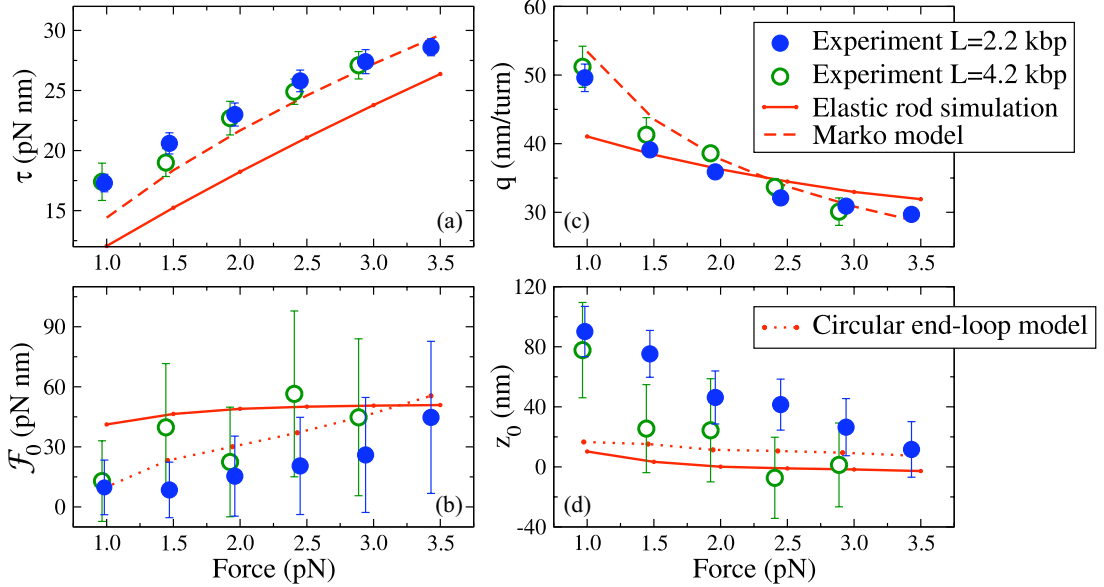


**Figure 3.3: Coexisting state parameters vs. applied force.** The four parameters describing the CS (coexisting torque  $\tau$ , extension versus linking number slope  $q$ , and the extra free energy  $\mathcal{F}_0$  and extension  $z_0$  necessary to form the end loop and tails of the plectoneme), as a function of applied force. The circles show values calculated from experimental data taken at two different overall DNA lengths  $L$ . Model predictions for our simulation<sup>4</sup> and Marko’s model [49] are shown as solid and dashed lines, respectively (using  $S = 0$  for  $\mathcal{F}_0$  predictions). The circular end-loop model uses average  $\tau$  and  $q$  values from the experiment to predict  $\mathcal{F}_0$  and  $z_0$ , shown as dotted lines.

correction to  $\mathcal{F}_0$  that would reduce it at the longer  $L$  by about  $kT \log 2 \approx 5$  pN nm; see Appendix B). We do expect  $\mathcal{F}_0$  and  $z_0$  to be sensitive to the local properties of the DNA in the end-loop of the plectoneme, so we suspect that the difference in  $z_0$  between the two measured lengths could be due to sequence dependence. With this data, we can also predict the length-dependence of the discontinuities, as shown in Figure 3.4 (left). Here we included entropic corrections to  $\mathcal{F}_0$  (see Appendix B),

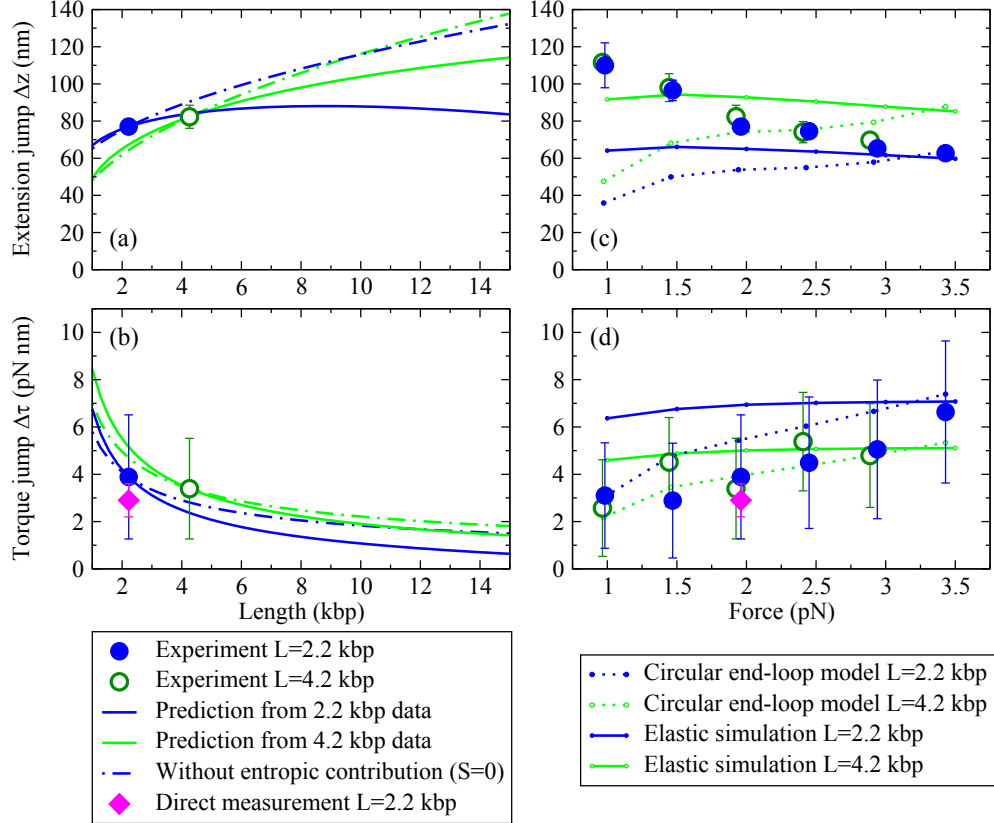


Figure 3.4: **Length- and force-dependence of discontinuities.** (a,b) Predicted length-dependence of the extension and torque jumps at  $F = 2$  pN. Using the CS parameters extracted from the experiment at two different lengths, Eqs. (3.4) and (3.5) predict the  $L$ -dependence of  $\Delta z$  and  $\Delta \tau$ . The circles show experimentally-measured values [with the torque jump here calculated from  $K^*$  using Eq. (3.4)]. Without entropic corrections to  $\mathcal{F}_0$  ( $S = 0$ ; dot-dashed lines)  $\Delta z$  depends noticeably on  $L$ , but including an initial estimate of  $S$  (solid lines) shows that entropic effects can significantly reduce this length-dependence. (c,d) Force-dependence of the extension and torque jumps, and predictions from two models. Disagreements with experimental data can be understood in terms of the four CS parameters in Figure 3.3. Also plotted as a diamond is  $\Delta \tau$  measured using the direct method depicted in Figure 3.2.

and we find that entropic effects significantly decrease the length-dependence of the extension jump.

Note that here we are solving for the experimental size of the torque jump using the observed  $K^*$  and  $\tau$  in Eq. (3.4). We also find direct evidence of  $\Delta\tau$  in the data by averaging over the torque separately in the SS and CS near the transition (Figure 3.2). With data taken at  $F = 2$  pN and  $L = 2.2$  kbp, we find  $\Delta\tau = 2.9 \pm 0.7$  pN nm, in good agreement with the prediction from  $K^*$  ( $3.9 \pm 2.6$  pN nm; see Figure 3.4). We can also predict the width of the range of linking numbers around  $K^*$  in which hopping between the two states is likely (where  $|\Delta\mathcal{F}| < kT$ ): expanding to first order in  $K - K^*$  gives a width of  $2kT/(\pi\Delta\tau)$ . This predicts a transition region width of about 0.9 turns for the conditions in Figure 3.2, agreeing well with the data.

### 3.5 Model predictions

We can now use various plectoneme models to calculate the four CS parameters, which in turn give predictions for the experimental observables. The results are shown as lines in Figure 3.3 and Figure 3.4 (right). As we expect entropic corrections to be small (changing  $\mathcal{F}_0$  by at most about 5 pN nm), we set  $S = 0$  for these comparisons.

First, we test Marko's phase coexistence model [49]. The plectoneme is modeled as a phase with zero extension and an effective twist stiffness  $P < C$ . Shown as dashed lines in Figure 3.3, the Marko model predicts the coexisting torque and extension slope well, with  $P$  as the only fit parameter (we use  $P = 26$  nm).

However, the Marko model (and any model that includes only terms in the free energy proportional to  $L$ ) produces  $\mathcal{F}_0 = 0$  and  $z_0 = 0$ .

In order to have a discontinuous transition, we must include the effects of the end loop and tails of the plectoneme. The simplest model assumes that the coexistence of stretched and plectonemic DNA requires one additional circular loop of DNA. Minimizing the total free energy for this circular end-loop model gives

$$\mathcal{F}_0 = 2\pi\sqrt{2BF_{\text{eff}}} - 2\pi\tau W_{\text{loop}}; \quad (3.6)$$

$$z_0 = 2\pi\xi(\tau)\sqrt{B/(2F_{\text{eff}})} - qW_{\text{loop}}, \quad (3.7)$$

where  $W_{\text{loop}}$  is the writhe taken up by the loop. For a perfect circle,  $W_{\text{loop}} = 1$ , and  $W_{\text{loop}} < 1$  for a loop with two ends not at the same location. We chose  $W_{\text{loop}} = 0.8$  as a reasonable best fit to the data. Using the experimentally measured  $\tau$  and  $q$ , the predictions are shown as solid lines in Figure 3.3 and Figure 3.4;  $\mathcal{F}_0$  is fit fairly well, but  $z_0$  is underestimated, especially at small applied forces.

In an attempt to more accurately model the shape of the plectoneme, we use an explicit simulation of an elastic rod, with elastic constants set to the known values for DNA. We must also include repulsion between nearby segments to keep the rod from passing through itself. Physically, this repulsion has two causes: screened Coulomb interaction of the charged strands and the loss of entropy due to limited fluctuations in the plectoneme. We use the repulsion free energy derived for the helical part of a plectoneme in Ref. [48], modified to a pairwise potential form (see Appendix B). We find that the simulation does form plectonemes (inset of Figure 3.1), and we can extract the four CS parameters, shown as solid lines in Figure 3.3.<sup>4</sup> Since  $\mathcal{F}_0$  and  $z_0$  are nonzero, we find discontinuities in the extension and torque at the transition; their magnitudes are plotted in Figure 3.4.

---

<sup>4</sup> We have also explored increasing the entropic repulsion by a constant factor of up to 3. Though this does bring the torques closer to the experiment, the only other significant change is

### 3.6 Conclusion

Both the circular loop model and the simulation produce torque and extension jumps of the correct magnitude, but in both cases  $\Delta z$  has an incorrect dependence on force and too much dependence on length. Our approach provides intuition about the causes of the discrepancies by singling out the four values (connected to different physical effects) that combine to produce the observed behavior. Specifically, we can better understand why the models' predictions are length-dependent: as displayed in Figure 3.4 (top left), the negligible length-dependence observed in experiment<sup>5</sup> is caused by a subtle cancellation of a positive length-dependence [smaller than either model, and described by Eq. (3.5)] combined with a negative contribution coming from entropic effects. One would expect, then, that any plectoneme model (even one that explicitly includes entropic fluctuations) might easily miss this cancellation. In general, without this intuition, it is difficult to know where to start in improving the DNA models.

The largest uniform discrepancy happens at small applied forces, where both models underestimate  $z_0$ ,<sup>6</sup> leading to an underestimate of  $\Delta z$ . We have examined various effects that could alter  $z_0$ , but none have caused better agreement (see also Appendix B). Adding to the circular end-loop model softening or kinking [21] at the plectoneme tip, or entropic terms from DNA cyclization theories [66, 60], uniformly *decreases*  $z_0$ . Increasing  $B$  in Eq. (3.6) by a factor of four (perhaps due to sequence dependence) does raise  $z_0$  into the correct range, but it also raises  $\mathcal{F}_0$  from Eq. (3.7) to values well outside the experimental ranges. Finally,  $z_0$  would

---

<sup>5</sup> After the publication of this chapter, a different experimental group has measured a length-dependence of the extension jump consistent with our results [8].

<sup>6</sup> Though the 4.2 kbp  $z_0$  data alone would be arguably consistent with the model predictions, the 2.2 kbp data highlights the discrepancy at small applied forces.

be increased if multiple plectonemes form at the transition, but we find that the measured values of  $\mathcal{F}_0$  are too large to allow for more than one plectoneme in this experiment.

## CHAPTER 4

### NUCLEATION AT THE DNA SUPERCOILING TRANSITION

#### 4.1 Introduction

As we have seen (Figure 3.2), holding DNA at the constant force, constant linking number supercoiling transition reveals two metastable states, with and without a plectoneme; these states are separated by a free energy barrier that is low enough to allow thermal fluctuations to populate the two states, but high enough that the characteristic rate of hopping is only about 10 Hz. Two experimental groups, using different methods to manipulate the DNA (one, an optical trap [27]; the other, magnetic tweezers [8]), have observed this nucleation at the transition and reported similar qualitative and quantitative results.

Reaction-rate theory predicts a rate of hopping related to the energy barrier between the two states. We perform a full calculation of the prefactor, including hydrodynamics, entropic factors, and sequence-dependent intrinsic bend disorder, to find which effects may contribute to this slow rate. We calculate a rate of order  $10^4$  Hz, about 1000 times faster than measured experimentally, and attribute the discrepancy to a theoretical energy barrier that is too small to match with experimental bounds from measured bistability at the transition.

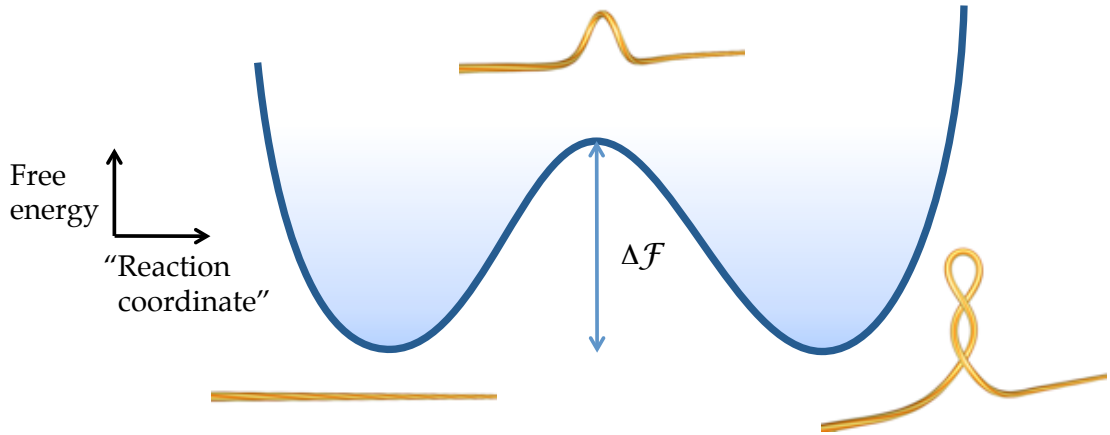


Figure 4.1: **The double-well.** A schematic one-dimensional representation of the two metastable states and the saddle point that separates them.

## 4.2 Nucleation rate calculation

### 4.2.1 Saddle point energetics

To understand the dynamics of nucleation, we must first find the saddle point DNA configuration that serves as the barrier between the stretched state and the plectonemic state. We will use the same elastic rod model for DNA as described in Chapter 3 [17]. For this model, without any repulsive interactions to stabilize plectonemes, Fain and coworkers used variational techniques to characterize the extrema of the elastic energy functional;<sup>1</sup> this revealed a “soliton-like excitation” as the lowest-energy solution with nonzero writhe [23]. They found that the soliton solution’s energy differed from that of the straight state by a finite amount in the infinite-length limit. This soliton state, depicted at the top of the barrier in Figure 4.1, is the one we identify as the saddle configuration.

The shape of the saddle configuration is controlled by the bend and twist elastic

---

<sup>1</sup> They take the infinite length limit, using fixed linking number and force boundary conditions.

constants  $B$  and  $C$ , as well as the torque  $\tau$  and force  $F$  applied as boundary conditions. Defining the lengths

$$a \equiv \sqrt{\frac{B}{F}} \quad (4.1)$$

$$b \equiv \frac{2B}{\tau} \quad (4.2)$$

$$\ell \equiv (a^{-2} - b^{-2})^{-1/2}, \quad (4.3)$$

we can write the Euler angles characterizing the saddle configuration as [23]

$$\begin{aligned} \cos \theta(s) &= 1 - 2 \left( \frac{a}{\ell} \right)^2 \left[ 1 - \tanh^2 \left( \frac{s}{\ell} \right) \right] \\ \phi(s) &= + \frac{s}{b} + \tan^{-1} \left[ \frac{b}{\ell} \tanh \left( \frac{s}{\ell} \right) \right] \\ \psi(s) &= \frac{s}{C/\tau} - \frac{s}{b} + \tan^{-1} \left[ \frac{b}{\ell} \tanh \left( \frac{s}{\ell} \right) \right], \end{aligned} \quad (4.4)$$

where  $s$  is arclength along the DNA backbone.

For the experiments in which we are interested,  $L/\ell \gg 1$  (the soliton ‘‘bump’’ is much smaller than the length of the DNA), such that we can safely remove the soliton from the infinite length solution and still have the correct boundary conditions:  $\theta = 0$  at the ends of the DNA, such that the tangent vector  $\hat{t}$  points along the  $z$  axis. In this case, the linking number in the saddle state is given by [23]

$$\begin{aligned} K_s &= \frac{1}{2\pi} [\phi(L/2) - \phi(-L/2) + \psi(L/2) - \psi(-L/2)] \\ &= \frac{\tau L}{2\pi C} + W_s(\tau), \end{aligned} \quad (4.5)$$

where we have separated the linking number into twist (the first term) and writhe:

$$W_s(\tau) = \frac{2}{\pi} \tan^{-1} \left[ \frac{b}{\ell} \tanh \left( \frac{L}{2\ell} \right) \right]. \quad (4.6)$$

To find the saddle configuration's torque at the supercoiling transition,<sup>2</sup> we numerically solve Eq. (4.5) for  $\tau$  using the experimentally observed critical linking number  $K_s^*$ .<sup>3</sup>

The energy barrier  $\Delta E$  is the difference in elastic energy between the saddle and straight states at the same linking number  $K_s$ . We find<sup>4</sup>

$$\Delta E = \frac{8B}{\ell} \tanh\left(\frac{L}{2\ell}\right) - 2\pi W_s \left(\tau + \frac{\pi C}{L} W_s\right). \quad (4.7)$$

Inserting the experimental values listed in Table 4.1 into Eq. (4.7), we calculate an energy barrier

$$\Delta E = 6 \text{ } kT. \quad (4.8)$$

This barrier would seem surprisingly small considering that typical atomic rates are on the order of  $10^{13}$  Hz: a simple estimate would give  $10^{13}e^{-6} = 10^{10}$  Hz for the hopping rate. The next sections present a more careful calculation, which shows that the timescale for motion over the barrier is in fact many orders of magnitude smaller due to the larger length scales involved, but also that the entropy from multiple available nucleation sites significantly lowers the barrier.

#### 4.2.2 Transition state theory: the basic idea

When, as in our case, the energy barrier is much larger than the thermal energy  $kT$ , the rate of nucleation is suppressed by the Arrhenius factor  $\exp(-\Delta E/kT)$ . Going beyond this temperature dependence to an estimate of the full rate, however, requires a more detailed calculation. We will follow the prescription from

---

<sup>2</sup> Note that this is not the same as the torque before or after the transition.

<sup>3</sup> We could alternatively use  $K_s^* = 8.1$  from our theory in Chapter 3, but finding the transition involves the complications of the full plectonemic state, including entropic repulsion, that are less well-understood than the elastic properties. Using this alternative  $K_s^*$  increases  $\Delta E$  by about  $1 \text{ } kT$ , which does not significantly alter our conclusions.

<sup>4</sup> Taking  $L \rightarrow \infty$ , this agrees with Eq. (19) of Ref. [23] if their  $F/L$  is replaced by  $\sqrt{2FB}$ .

Table 4.1: Parameter values for nucleation rate calculation.

Symbol	Description	Value
$B$	bend elastic constant	(43 nm) $kT$ [27]
$C$	twist elastic constant	(89 nm) $kT$ [27]
$F$	applied force	1.96 pN [27]
$kT$	thermal energy at 23.5°C	4.09 pN nm
$L$	basepair length of DNA strand	740 nm [27]
$K_s^*$	critical linking number	8.7 [27]
$\tau$	saddle point torque [Eq. (4.5)] <sup>5</sup>	25 pN nm
$\ell$	soliton length scale [Eq. (4.3)] <sup>5</sup>	13 nm
$R$	bead radius	250 nm
$\eta$	viscosity of water at 23.5°C	$9.22 \times 10^{-10}$ pN s / nm <sup>2</sup>
$N$	number of segments	740
$d$	length of segment	1 nm
$r_D$	DNA hydrodynamic radius	1.2 nm
$\zeta$	translation viscosity coeff. [Eq. (4.12)]	$1.54 \times 10^{-9}$ pN s / nm <sup>2</sup>
$\lambda$	rotation viscosity coeff. [Eq. (4.13)]	$1.67 \times 10^{-8}$ pN s

Kramers' spatial-diffusion-limited reaction-rate theory [33] to calculate the rate of hopping. The requirements are that (1) the timescales involved in motion within the two metastable wells are much faster than the timescale of hopping, and (2) (for Kramers' "spatial-diffusion-limited" theory) the system is overdamped, in the sense that the ratio of damping strength to the rate of undamped motion over the barrier top is large. We check that these requirements are met after the calculation in Section 4.2.4.

---

<sup>5</sup> These values have been calculated using  $B_m = B$ , that is, for disorder  $D = 0$ . See Eq. (4.28).

Under these conditions, Kramers' reaction-rate theory tells us that the rate of hopping over the barrier is controlled only by the rate of motion through the “narrow pass” at the top of the barrier, since it is much slower than any other timescale in the system. This means that the hopping rate should be the characteristic rate of motion across the barrier top times the probability of finding the system near the barrier top, which, in terms of the curvature in the unstable direction away from the saddle point, we can write schematically as

$$\begin{aligned} k_{\text{hopping}} &= (\text{Characteristic rate of motion at barrier top}) (\text{Prob. of being at top}) \\ &= \left( \frac{\text{Energy curvature}}{\text{Damping}} \right) (\text{Prob. of being at top}). \end{aligned} \quad (4.9)$$

#### 4.2.3 Dynamics of DNA in water: the diffusion tensor

To find the rate of motion over the barrier top, we need to know the microscopic dynamics. We will be treating the DNA strand as a series of cylindrical segments, parametrized by the Cartesian coordinates  $(x_n, y_n, z_n)$  of one end of each segment plus the Euler angle  $\psi_n$  that controls local twist (see section 5.3.2 for a discussion about the choice of coordinates). Assuming overdamped motion such that we can neglect inertial terms, we will write the equations of motion in the form [with  $\vec{r}_n = (x_n, y_n, z_n, \psi_n)$ ,  $i, j$  labeling coordinates, and  $m, n$  labeling segments] [33]

$$\frac{d\vec{r}_{mi}}{dt} = -M_{mi,nj} \frac{dE}{d\vec{r}_{nj}}; \quad (4.10)$$

$M$  is the diffusion tensor, which transforms forces to velocities.

The simplest diffusion tensor produces motion proportional to the local forces, making it diagonal in segment number  $n$  and coordinate  $i$ :

$$M_{mi,nj}^{\text{diagonal}} = \begin{cases} \frac{1}{d\zeta} \delta_{mn} \delta_{ij} & \text{for } i, j \in \{x, y, z\} \\ \frac{1}{d\lambda} \delta_{mn} & \text{for } i = j = \psi \end{cases} \quad (4.11)$$

The viscous diffusion constants are set so they reproduce the known diffusion constant for a straight cylinder of length  $B/kT$  (the bending persistence length) and radius  $r_D = 1.2$  nm: [2, 14]

$$\zeta = \frac{2\pi\eta}{\ln(B/(kT r_D))} \quad (4.12)$$

$$\lambda = 2\pi\eta r_D^2, \quad (4.13)$$

where the viscosity of water  $\eta = 9.22 \times 10^{-10}$  pN s/nm<sup>2</sup> at the experimental temperature of 23.5° C.

It is important to note that the DNA in this experiment is attached to a large bead (with radius  $R \approx 250$  nm) that must also be pulled through the water during the transition.<sup>6</sup> We take this into account by setting the translational diffusion constant for the final segment in the chain according to Stokes' Law:

$$M_{Ni,Nj} = \delta_{ij}/(6\pi\eta R) \quad \text{for } i, j \in \{x, y, z\}. \quad (4.14)$$

Hydrodynamic effects may also be important, which introduce interactions between segments: as segments move, they change the velocity of the water around them, and this change propagates to change the viscous force felt by other nearby segments. Following Ref. [40], we incorporate hydrodynamic effects by using a Rotne-Prager tensor for the translational diffusion, modeling the strand as a string

---

<sup>6</sup> It is also known that the presence of a surface (the glass plate to which the DNA is attached) leads to an enhanced hydrodynamic diffusion on the bead that depends on the distance  $z$  from the surface; for motion perpendicular to the surface [15],  $\zeta_{\text{eff}} = \zeta[1 + R/z + R/(2R + 6z)]$ . For our typical  $z$  and  $R$ , this increases  $\zeta$  for the bead by a factor of about 1.6, which does not significantly change our conclusions, so we choose not to include this correction.

of beads:<sup>7</sup>

$$M_{mi,nj}^{\text{Rotne-Prager}} = \begin{cases} D_0 \frac{3a}{4r_{mn}} \left[ \delta_{ij} + \frac{r_{mn,i}r_{mn,j}}{r_{mn}^2} + \frac{2a^2}{3r_{mn}^2} \left( \delta_{ij} - 3\frac{r_{mn,i}r_{mn,j}}{r_{mn}^2} \right) \right] & \text{for } r_{mn} \geq 2a, m \neq n \\ D_0 \left[ \left( 1 - \frac{9}{32} \frac{r_{mn}}{a} \right) \delta_{ij} + \frac{3}{32} \frac{r_{mn,i}r_{mn,j}}{a r_{mn}} \right] & \text{for } r_{mn} \leq 2a, m \neq n \\ D_0 \delta_{ij} & \text{for } m = n \end{cases} \quad (4.15)$$

for  $i, j \in \{x, y, z\}$ , where  $D_0 = (6\pi\eta a)^{-1}$  and  $a$  is an effective bead radius chosen such that a straight configuration of Kuhn length  $L_K = 2B/kT$  (with a number of beads  $L/L_K$ ) has the same total diffusion constant as a cylinder of length  $L$  and radius  $r_D$  (see [40]). With the parameters in Table 4.1, we use  $a = 0.98$  nm.

#### 4.2.4 Transition state theory: full calculation

In the full multidimensional space inhabited by our model, the saddle configuration will have a single unstable direction that locally defines the “reaction coordinate” depicted in Figure 4.1. The direction of the unstable mode can be found numerically by locally solving the equations of motion Eq. (4.10). First, the local quadratic approximation to the energy is provided by the Hessian

$$H_{mi,nj} = \frac{d^2 E}{dr_{mi} dr_{nj}}, \quad (4.16)$$

where the derivatives are taken with respect to the unitless variables  $\vec{r} = x/\ell_0, y/\ell_0, z/\ell_0, \psi$  (where  $\ell_0$  is an arbitrary length scale;<sup>8</sup> see also section 5.3.2).

---

<sup>7</sup> The Rotne-Prager tensor (also known as the Rotne-Prager-Yamakawa tensor [20]) is a regularized version of the Kirkwood-Riseman diffusion tensor (also known as the Oseen-Burgers tensor [20]) that is modified at short distances such that it becomes positive definite, producing stable dynamics [63].

<sup>8</sup> Choosing these units for our variables makes the path integral partition function unitless:

$$Z = \int \prod_n \frac{dx_n dy_n dz_n d\psi_n}{l_0^3} e^{-E(\{x, y, z, \psi\})/kT}.$$

Inserting the quadratic form defined by  $H$  at the saddle point into Eq. (4.10), we then diagonalize the matrix  $MH_{\text{saddle}}$  to find the dynamical normal modes of the system; the single mode  $u$  with a negative eigenvalue  $-\lambda_b$  is the unstable mode at the top of the barrier:

$$M_{li,mj} H_{mj,nk}^{\text{saddle}} u_{nk} = -\lambda_b u_{li}, \quad (4.17)$$

and  $\lambda_b$  defines the characteristic rate of Eq. (4.9). We can check that we have found the correct saddle configuration and unstable mode  $u$  by perturbing forward and backward along  $u$  and numerically integrating the dynamics of Eq. (4.10) — one case should end in the straight state well and the other in the plectonemic state well. This generates the transition path connecting the two wells, as illustrated in Figure 4.2.

To find the probability of being near the top of the barrier in the multidimensional case, we need to know not only the energy barrier  $\Delta E$ , but also the entropic factors coming from the amounts of constraint in the other directions in phase space,<sup>9</sup> which are controlled by the remaining eigenvalues of  $H_{\text{saddle}}$  and the Hessian  $H_{\text{straight}}$  of the straight state. The full result from spatial-diffusion limited multidimensional transition state theory is (to lowest order in  $kT$ ) [33]

$$k_{\text{hopping}} = \frac{\lambda_b}{2\pi} \sqrt{\frac{\det H_{\text{straight}}/(2\pi kT)}{|\det H_{\text{saddle}}/(2\pi kT)|}} e^{-\Delta E/kT}; \quad (4.18)$$

or, in terms of the eigenvalues of each Hessian,

$$k_{\text{hopping}} = \frac{\lambda_b}{2\pi} \sqrt{\frac{\prod_{i=1}^{4(N-2)} \lambda_i^{\text{straight}}/(2\pi kT)}{|\prod_{i=1}^{4(N-2)} \lambda_i^{\text{saddle}}/(2\pi kT)|}} e^{-\Delta E/kT}. \quad (4.19)$$

These are correct if each eigenvalue is sufficiently large such that the local quadratic form is a good approximation where  $E \lesssim kT$ .

---

<sup>9</sup> The rate will be slower if the system must traverse a more narrow “pass” at the saddle point.

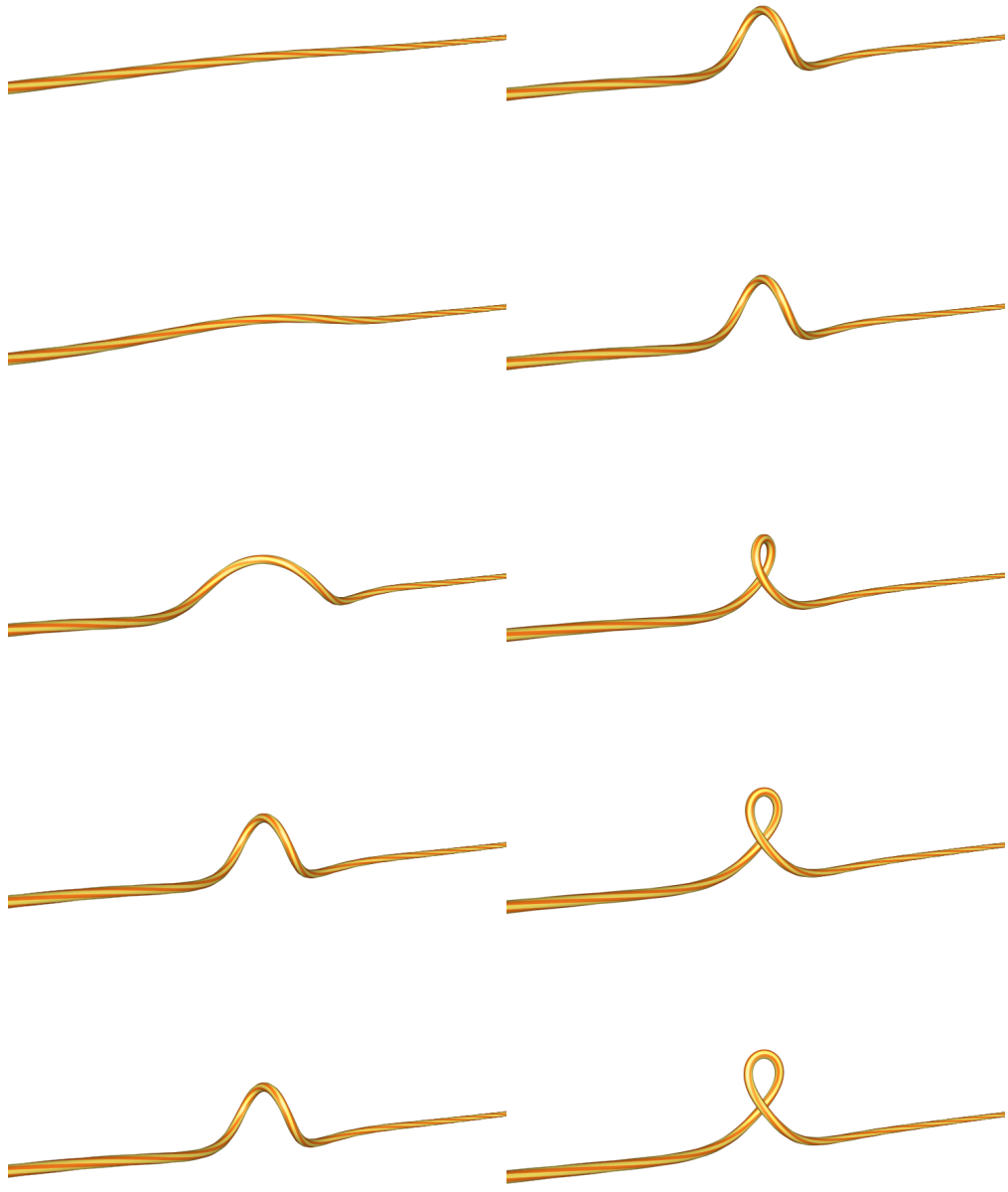


**Figure 4.2: Snapshots along the transition path.** After perturbing the saddle state along the unstable direction  $u$  (bottom left and top right snapshots), we integrate the equations of motion in Eq. (4.10) to follow the unstable dynamics into the two metastable wells. Here, we use Rotne-Prager dynamics with  $D = 0$ , the timestep between frames is  $1.5 \times 10^{-6}$  s, and other parameters are as given in Table 4.1.

In our case, we must deal separately with the two zero modes due to invariance with respect to location  $s_s$  and rotation angle  $\rho_s$  of the saddle configuration's bump. Extracting these directions from the saddle integral, we have

$$\begin{aligned} k_{\text{hopping}} &= \frac{\lambda_b}{2\pi} \left( \int J_s J_\rho \frac{ds_s}{\ell_0} d\rho_s \right) \sqrt{\frac{\prod_{i=1}^{4(N-2)} \lambda_i^{\text{straight}} / (2\pi kT)}{|\prod_{i=3}^{4(N-2)} \lambda_i^{\text{saddle}} / (2\pi kT)|}} e^{-\Delta E/kT} \\ &= \frac{\lambda_b}{2\pi} \left( 2\pi \frac{L}{\ell_0} J_s J_\rho \right) \frac{1}{2\pi kT} \sqrt{\frac{\det H_{\text{straight}}}{|\det' H_{\text{saddle}}|}} e^{-\Delta E/kT}, \end{aligned} \quad (4.20)$$

where the Jacobians  $J_s = |\vec{dr}_s/ds_s|$  and  $J_\rho = |\vec{dr}_s/d\rho_s|$ , and  $\det'$  represents the determinant without the two zero modes (but including the unstable mode). Numerically,  $J_s$  and  $J_\rho$  are calculated using the known forms for derivatives of the saddle point's Euler angles  $\alpha_s$  [Eqs. (4.4)] with respect to  $s_s$  and  $\rho_s$ :  $J_s = |[J^T(\vec{r}_s)]^{-1} d\vec{\alpha}_s/ds_s|$  and  $J_\rho = |[J^T(\vec{r}_s)]^{-1} d\vec{\alpha}_s/d\rho_s|$ , where  $J$  is defined in Eq. (5.29).

We can now check that we meet the requirements for using Kramers' theory set out in Section 4.2.2. First, we check condition (1) by looking at the smallest nonnegative eigenvalue of  $MH$ . The slowest mode is transverse motion with wavelength  $2L$ , and since the bead has much higher viscosity than the rest of the DNA chain, it sets the damping for this motion; this produces a frequency  $F/(6\pi\eta RL) \approx 600$  Hz, much faster than the timescale of hopping. We can check (2) by comparing the characteristic rate for undamped barrier motion to the characteristic damping rate. In the spirit of Section 4.3.2, we are dealing with a portion of DNA of length  $\ell_B$ , such that it has a mass  $\mu\ell_B$ , where  $\mu = 3.3 \times 10^{-21}$  g/nm is the linear mass density of DNA [55], and the energy curvature at the barrier top is on the order of  $\pi^4 B/\ell_B^3$ . Then the damping coefficient is  $\zeta/\mu = 5 \times 10^{11}$  s $^{-1}$ , and the rate for undamped barrier motion is  $\sqrt{(\pi^4 B/\ell_B^3)/(\mu\ell_B)} = 4 \times 10^8$  s $^{-1}$ . Since the ratio of these values is much greater than one, we are firmly in the overdamped regime, and Kramers' rate theory applies [33].

## 4.3 Initial results and order of magnitude checks

### 4.3.1 Initial results

We calculate the rate in Eq. (4.20) using numerical methods described in Chapter 5.

We will quote the results of the calculation by looking individually at the factors that contribute to the rate. Writing the rate in various simple forms,

$$k_{\text{hopping}} = \frac{\lambda_b}{2\pi} e^{-\Delta E/kT + S/k} \quad (4.21)$$

$$= \frac{\lambda_b}{2\pi} e^{-\Delta\mathcal{F}/kT}; \quad (4.22)$$

$S$  encapsulates the entropic factors coming from fluctuations in the straight and saddle configurations, and the effective free energy barrier  $\Delta\mathcal{F} = \Delta E - TS$  provides the relative probability of being near the top of the saddle [33].

For the experimental parameters in Table 4.1, using Rotne-Prager dynamics,<sup>10</sup> we find  $\lambda_b/2\pi = 4.0 \times 10^4$  Hz,  $\Delta E/kT = 5.5$ , and  $S/k = 5.8$ , such that  $\Delta\mathcal{F}/kT = -0.3$ . There are two surprises here: (1) the characteristic rate of motion over the barrier is very slow compared to typical atomic timescales, and (2) the entropic factors are so large that they completely erase the energy barrier.

We consider these issues in more detail in the next three sections.

---

<sup>10</sup> Using  $M^{\text{diagonal}}$  [Eq. (4.11)] produces a comparable unstable mode rate of  $\lambda_b/2\pi = 5.6 \times 10^4$  Hz. We use the more physical  $M^{\text{Rotne-Prager}}$  [Eq. (4.15)] here and in all further calculations.

### 4.3.2 Order of magnitude estimates of the dynamical prefactor

#### Motion of atomic object subject to atomic forces

Typically, rates for atomic scale systems have prefactors on the order of  $10^{13}$  Hz, which with an energy barrier of size  $6 kT$  would give an answer  $10^9$  times too fast. Indeed, inserting typical atomic length scales ( $\text{\AA}$ ) and energy scales (eV) into the simple rate equation Eq. (4.9), and using Stokes' law for an angstrom sized bead in water, the energy curvature is  $1 \text{ eV}/\text{\AA}^2$ , and the damping is  $(6\pi\eta r_a)^{-1} = 10^{-13} \text{ eV s}/\text{\AA}^2$ , producing a dynamical prefactor of  $10^{13}$  Hz.

#### Motion of elastic rod in viscous fluid

Why, then, is our dynamical prefactor of order  $10^4 - 10^5$  Hz? It turns out that the relevant length and energy scales for the DNA supercoiling transition are not atomic. For the saddle state, we are dealing with length scales on the order of tens of nanometers (much larger than single atoms), and energy scales related to the elastic constants ( $B/\ell \approx 10 \text{ pN nm} < 0.1 \text{ eV}$ ).

To arrive at a better estimate, we can approximate the saddle energetics from bending energies only. Consider approximating the saddle state as a straight configuration with a single planar sinusoidal bump of length  $\ell_B$  and amplitude  $A$ . Since the elastic bending energy is  $E_B = \frac{B}{2} \int (\frac{dt}{ds})^2 ds$ , where the relevant component of the tangent vector is in this case  $t = Ak_t \cos(k_t s)$  for wavenumber  $k_t = \pi/\ell_B$ , the total bending energy for the bump is  $E_B = \frac{B\ell_B}{2} k_t^4 A^2 = \frac{\pi^4 B}{\ell_B^3} \frac{A^2}{2}$ ; this leads to an energy curvature with respect to amplitude of  $d^2 E_B / dA^2 = \frac{\pi^4 B}{\ell_B^3}$ . The viscous

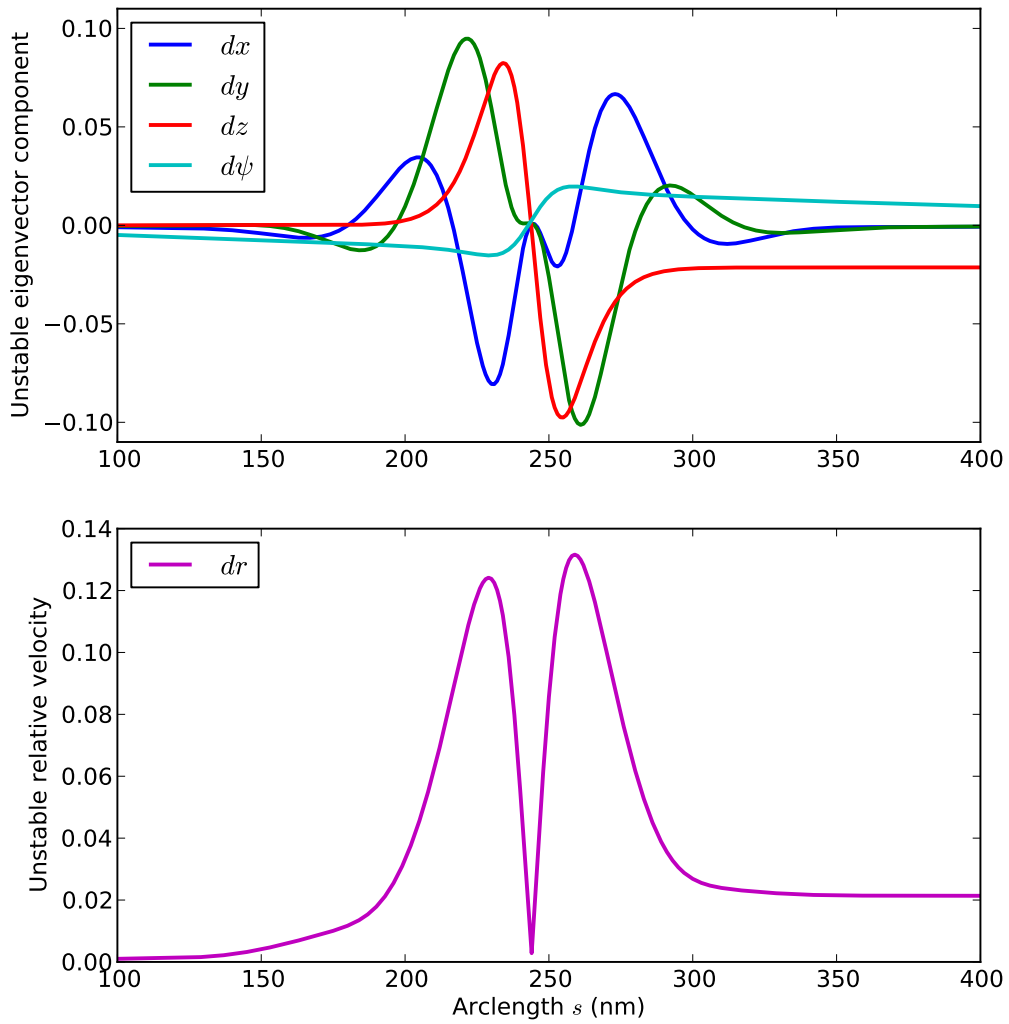


Figure 4.3: **Unstable mode at top of barrier.** (top) The four components of the unstable mode eigenvector as a function of arclength  $s$  along the DNA strand. (bottom) Plot of  $dr = \sqrt{dx^2 + dy^2 + dz^2}$ ; the peaks show the locations where the (Cartesian) motion of the DNA is greatest when traversing the barrier. Note that the width of the peak is about 75 nm — inserting this length scale into Eq. (4.23) produces a prefactor  $\sim 10^5$  Hz.

damping coefficient corresponding to a rod of radius  $r_D$  and length  $\ell_B$  moving sideways through water is  $\ell_B \zeta$ , with  $\zeta$  given by Eq. (4.12). Putting this together, our back-of-the-envelope estimate for the prefactor is [see Eq. (4.9)]

$$\frac{\text{Energy curvature}}{\text{Damping}} \sim \frac{\pi^4 B}{\ell_B^4 \zeta}. \quad (4.23)$$

We see that the prefactor is strongly dependent on the length scale  $\ell_B$  of the bending of DNA in the unstable mode motion. This length scale should be related to the length  $\ell \sim 10$  nm, defined in Eq. (4.3), characterizing the shape of the saddle configuration. As shown in Figure 4.3, we can check the amount of DNA involved in the unstable mode motion by looking at the unstable mode eigenvector. This reveals that a better estimate for  $\ell_B$  is in fact 75 nm; inserting this into Eq. (4.23) gives a prefactor  $\sim 10^5$  Hz, agreeing with the order of magnitude found in the full calculation. This simple calculation shows, then, how the 8 orders of magnitude separating the atomic scale rates from that of our full DNA calculation arise from the smaller energy scales and larger length scales involved.

### 4.3.3 Understanding the entropic factor

We calculate an entropy  $S$  that entirely cancels the energy barrier  $\Delta E$ . What sets the size of  $S$ ? Comparing Eq. (4.20) and Eq. (4.21), we see that the entropic factor

$$e^{(S/k)} = \left(2\pi \frac{L}{\ell_0} J_s J_\rho\right) \frac{1}{2\pi kT} \sqrt{\frac{\det H_{\text{straight}}}{|\det' H_{\text{saddle}}|}}. \quad (4.24)$$

This factor comes from comparing the size of fluctuations in the normal modes of the straight and saddle states. We expect that most of the modes will be similarly constrained in the two states, except for the two zero modes that appear in the saddle state. These zero modes create a family of equivalent saddle points at

different locations and rotations along the DNA, each of which contributes to the final rate. Imagining counting the number of equivalent saddle points along  $2\pi$  radians in  $\rho$  and  $L$  nanometers in  $s$ , we can write the entropic factor in the form

$$e^{(S/k)} = \frac{2\pi}{\rho_0} \frac{L}{s_0}, \quad (4.25)$$

where  $\rho_0$  and  $s_0$  define how far one must move the soliton bump along  $\rho$  and  $s$  to get to an independent saddle point.<sup>11</sup> We expect that  $\rho_0$  should be about  $\pi$  radians (giving two independent saddle points at each  $s$ ), and  $s_0$  should be of the order of the length scale of the soliton,  $\ell \approx 10$  nm, producing  $\rho_0 s_0 \sim 30$  nm. And indeed, using  $S/k = 5.8$  found in the full calculation, Eq. (4.25) gives  $\rho_0 s_0 = 14$  nm. Thus the size of the entropic factor makes sense: it is large because there are many equivalent locations along the DNA where the plectoneme can form.

#### 4.3.4 Experimental estimate of the effective free energy barrier

The effective free energy barrier in our calculation is reduced to near zero. This is due to the entropic factor, which favors the saddle state due to the location and rotation zero modes.<sup>12</sup> With a free energy barrier this small, though, plectonemes would form spontaneously even at zero temperature, and with no barrier to nucleation, no bistability would be observed — indeed, this would violate our original assumptions necessary for the use of transition state theory itself. However, the fact that bistability *is* observed in experiment [27, 8] assures us that the effective

---

<sup>11</sup> Planck's constant plays an analogous role in quantum statistical mechanics. Also, we define similar quantities  $L_0$  and  $K_0$  in Section B.5.

<sup>12</sup> In the infinite length limit, entropy will always win, smearing out the transition.

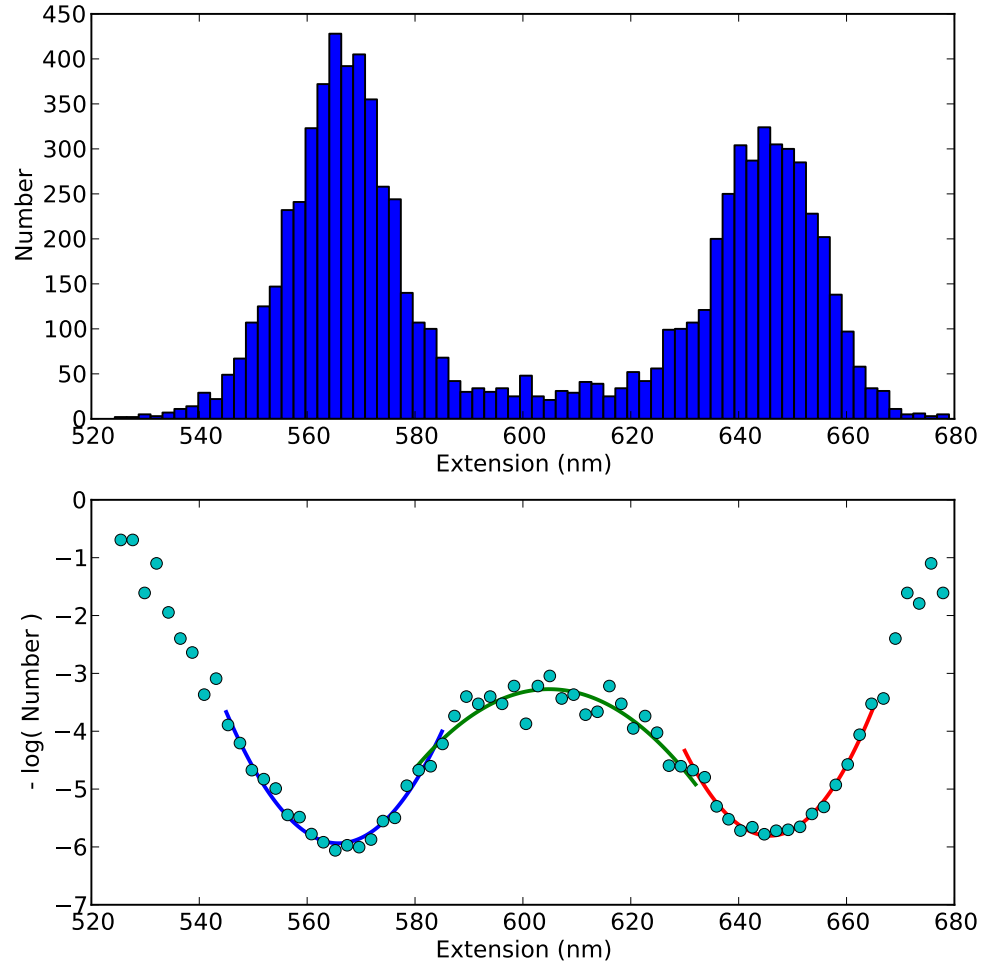


**Figure 4.4: Bound on free energy barrier from experimental extension distribution.** (top) A histogram of measured extensions near the supercoiling transition, for  $F = 2$  pN,  $L = 2.2$  kbp [27, 17], clearly demonstrating bistability. (bottom) Fitting the negative logarithm of the probability density to three quadratic functions indicates that there is a free energy barrier separating the straight state (longer extensions) from the supercoiled state (shorter extensions) of at least  $2 kT$ .

free energy barrier is in reality nonzero; furthermore, the degree of bistability can give us a reasonable bound on the size of the barrier.

Two separate experimental groups have directly measured the distribution of extensions observed for many seconds near the supercoiling transition; one such histogram [27, 17] is shown in the top of Figure 4.4, and the distributions measured by the other group [8] appear remarkably similar. Taking the logarithm of this probability density produces an effective free energy landscape, shown in the bottom of Figure 4.4.

To compare the free energy barrier apparent from the extension data to the one from our calculation [defined in Eq. (4.21)], there are two subtleties to consider. First, the measurements with extension near the middle, between the two peaks, are not guaranteed to correspond to configurations that are traversing the saddle between the two wells (that is to say, extension is not the true reaction coordinate). Since adding extra probability density unrelated to the transition near the saddle point would lower the measured effective free energy barrier, we will only be able to put a lower bound on the true  $\Delta\mathcal{F}$ . Second, looking at the transition state rate equation for one-dimensional dynamics [33],

$$k_{1D} = \frac{\lambda_b}{2\pi} \sqrt{\frac{\lambda_{\text{well}}}{\lambda_{\text{saddle}}}} e^{-\Delta E/kT}, \quad (4.26)$$

we see the entropic factor coming from the ratio of energy curvatures in the saddle and well states.<sup>13</sup> Comparing this to Eq. (4.22), we see that the comparable effective free energy barrier should be corrected by this entropic ratio, such that

$$\Delta\mathcal{F}/kT = \Delta E/kT - \frac{1}{2} \ln \frac{\lambda_{\text{well}}}{\lambda_{\text{saddle}}}, \quad (4.27)$$

where the  $\lambda$ s are the curvatures the well and saddle states. As shown in the bottom

---

<sup>13</sup> If the wells become much narrower than the barrier, they are entropically disfavored, and the barrier-crossing rate increases.

of Figure 4.4, we can use fit parabolas to estimate this entropic correction, finding  $0.5 kT$ . Using the heights of the parabolic fits, we find that  $\Delta E = 2.5 kT$ , such that our lower bound on the effective free energy barrier is about  $2 kT$ .

## 4.4 Possible corrections

### 4.4.1 Including intrinsic bends

DNA with a random basepair sequence is not perfectly straight, but has intrinsic bends coming from the slightly different preferred bond angles for each basepair. This can profoundly affect our calculation by both providing pinning sites for plectonemes and changing the relevant effective viscosity.

#### History of intrinsic bend measurements

Since thermal fluctuations also bend DNA, the degree of intrinsic bend disorder is difficult to measure, but can be estimated using specific DNA sequences that are intrinsically nearly straight. The contribution to the bend persistence length from quenched disorder alone ( $P$ ) can be found using the relation [4]  $(B/kT)^{-1} = P_{\text{eff}}^{-1} = P_m^{-1} + P^{-1}$ :  $P_m$  is found using an intrinsically straight sequence (such that  $P^{-1} = 0$ ) and compared to  $P_{\text{eff}}$  from a random sequence.

Using estimates of wedge angles along with sequence information, Trifonov et al. estimated  $P = 216 \text{ nm}$  [73, 58]. An experiment using cryo-electron microscopy [4] found  $P_m \approx 80 \text{ nm}$  and  $P_{\text{eff}} \approx 45 \text{ nm}$ , giving an intrinsic bend persistence length of  $P \approx 130 \text{ nm}$ . More recently, a group using cyclization efficiency measurements

found  $P_m = 49.5 \pm 1$  nm and  $P_{\text{eff}} = 48 \pm 1$  nm, from which they conclude that  $P > 1000$  nm [76], in striking contrast with the previous estimates.

We include intrinsic bend disorder in our simulations by shifting the zero of bending energy for each segment by a random amount, parameterizing the disorder strength by  $D = P^{-2}$  (see Section 5.3.1 for a detailed description). We are able to locate the new saddle point including disorder, as illustrated in Figure 4.5, using numerical methods described in Section 5.3.4. Due to the disagreement in the literature about the correct value of  $P$ , we treat it as an adjustable parameter and examine the effects of disorder in a range from  $P = 1000$  nm to  $P = 130$  nm ( $D = 0.03$  nm $^{-1/2}$  to  $D = 0.09$  nm $^{-1/2}$ ).

### Renormalization of DNA elastic parameters

It is important to note that the measured elastic constants  $B$  and  $C$  are effective parameters that have been renormalized by both thermal fluctuations and intrinsic bend disorder. Our simulations do not explicitly include thermal fluctuations, but incorporate them by using the measured effective elastic constants. When we explicitly include bend disorder, however, we must use microscopic constants  $B_m$  and  $C_m$  so they create the same large-scale (measured) effective constants. Nelson has characterized the first-order effect of disorder on the elastic constants [58]; correspondingly, we use microscopic elastic parameters

$$B_m = \frac{B}{1 - B/(kTP)}, \quad (4.28)$$

$$C_m = C. \quad (4.29)$$

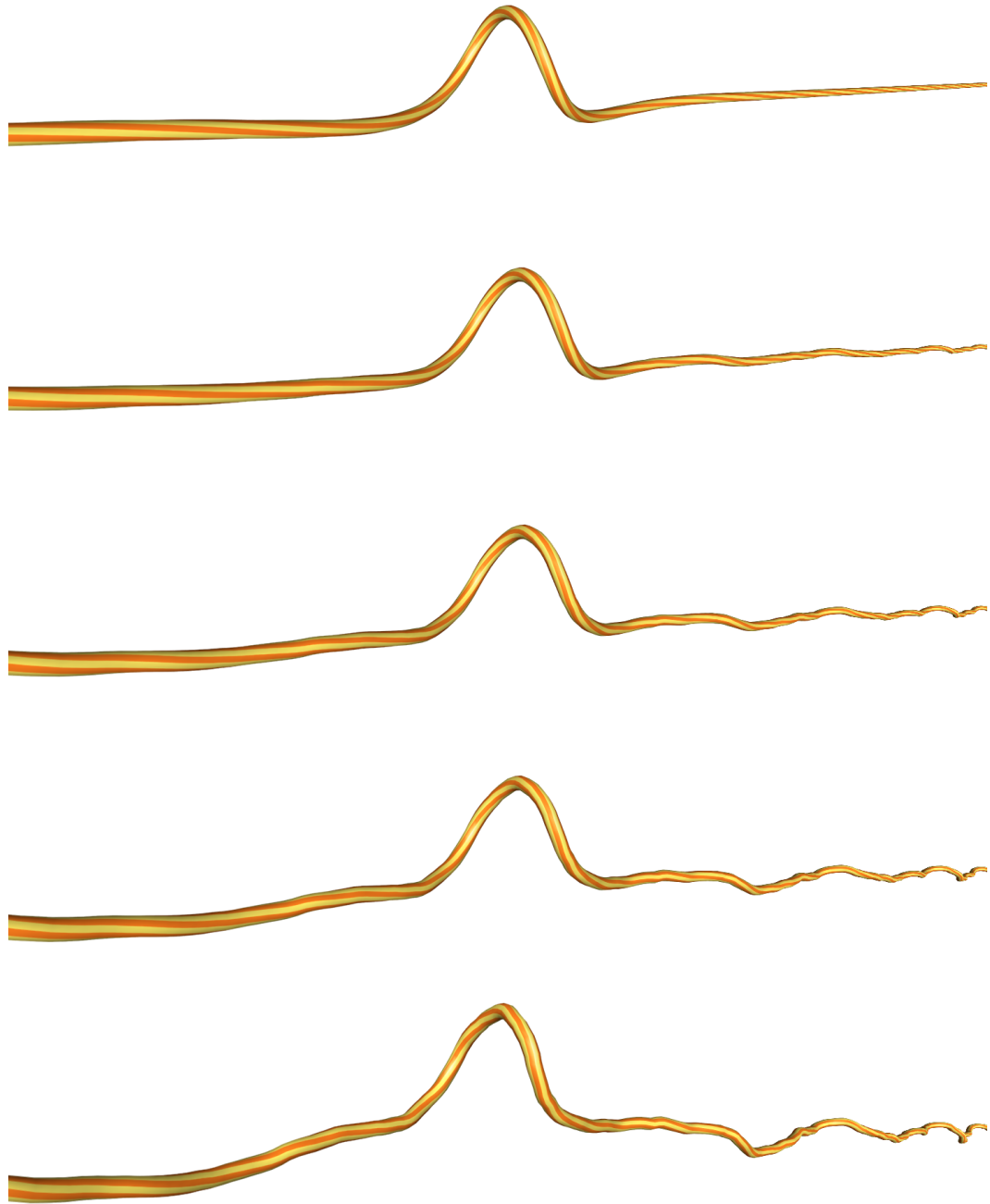


Figure 4.5: **The saddle state with increasing intrinsic bend disorder.** From top to bottom,  $D = (0, 0.02, 0.04, 0.06, 0.088) \text{ nm}^{-1/2}$ , corresponding to persistence lengths  $P = (\infty, 2500, 625, 278, 130) \text{ nm}$ , respectively. The saddle state is located numerically by searching locally for zero force solutions.

## Rate equation with disorder

If the disorder is large enough, plectoneme formation will be strongly pinned to one or more locations along the DNA. In this case, the zero modes have vanished, and we find the total rate by adding the contributions from each saddle point at each location  $s_j$ . Using Eq. (4.18),

$$k_{\text{hopping}} = \sum_j \frac{\lambda_{b,j}}{2\pi} \sqrt{\frac{\det H_{\text{straight}}}{|\det H_{\text{saddle}}|}} e^{-(E_{\text{saddle},j} - E_{\text{straight}})/kT}. \quad (4.30)$$

We can determine when this approximation will be valid by checking that fluctuations in the saddle point position  $s_j$  are small compared to the spacing between locations. The size of fluctuations in  $s_j$  can be found in the quadratic approximation as

$$\Delta s_j = \sqrt{kT \left/ \frac{d^2}{ds_j^2} E_{\text{saddle}}(s_j) \right.} \approx \sqrt{kT \left/ \frac{d^2}{ds_j^2} \left( D \frac{dE_{\text{saddle}}(s_j)}{dD} \right) \right.}, \quad (4.31)$$

where we have replaced  $E_{\text{saddle}}$  by its first-order approximation at low disorder  $D$  (see Section 5.3.1). Calculating the second derivative numerically at the pinning sites using Eq. (5.18), we find  $\frac{d^2}{ds_j^2} \frac{dE_{\text{saddle}}(s_j)}{dD} \approx 0.5 \text{ pN/nm}$ . The large disorder limit becomes valid when the fluctuations in  $s_j$  are much smaller than the average distance between pinning sites, about 75 nm (see Figure 5.2). Setting  $\Delta s_j < 75 \text{ nm}$  in Eq. (4.31) then produces a lower bound on the disorder strength  $D$  (or, equivalently, an upper bound on the intrinsic bend disorder persistence length  $P$ ):

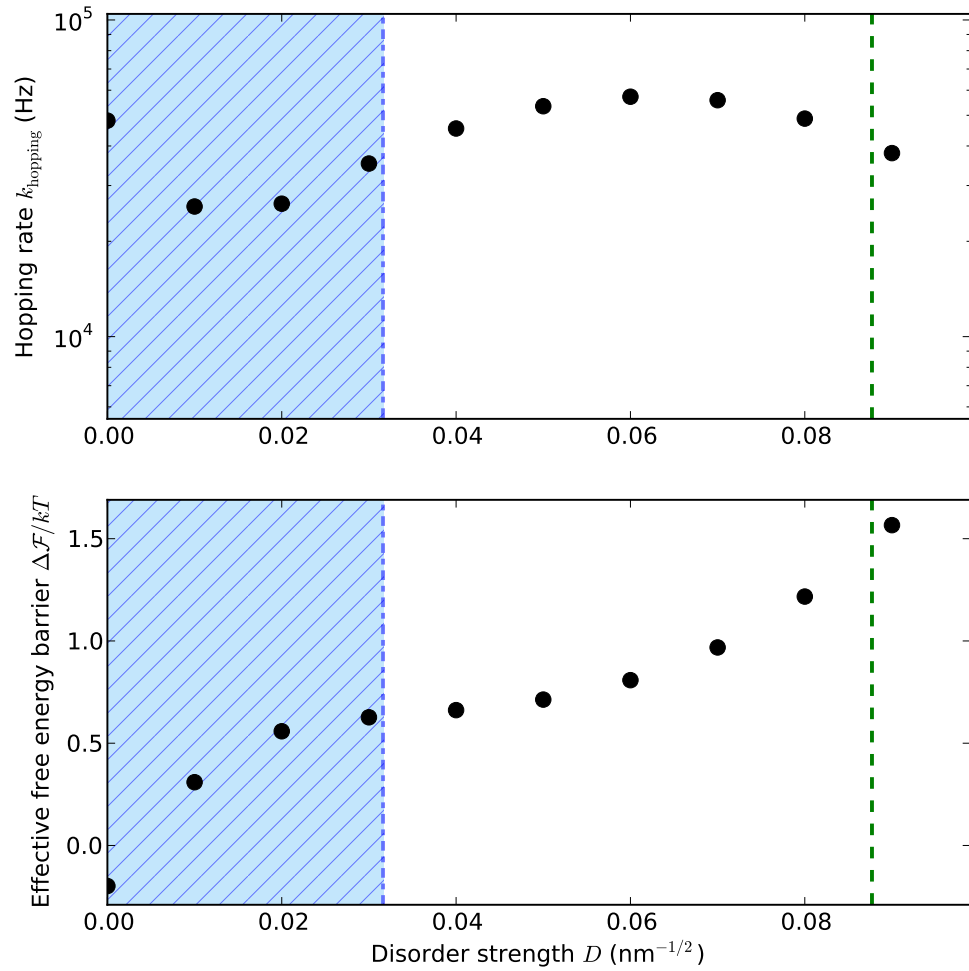
$$D > 10^{-3} \text{ nm}^{-1/2}, \text{ or } P < 10^6 \text{ nm}. \quad (4.32)$$

The experimental estimates for the persistence length  $P$  are typically much smaller than this bound (hundreds to thousands of nanometers), so the large disorder limit [Eq. (4.30)] should be valid for our calculation.

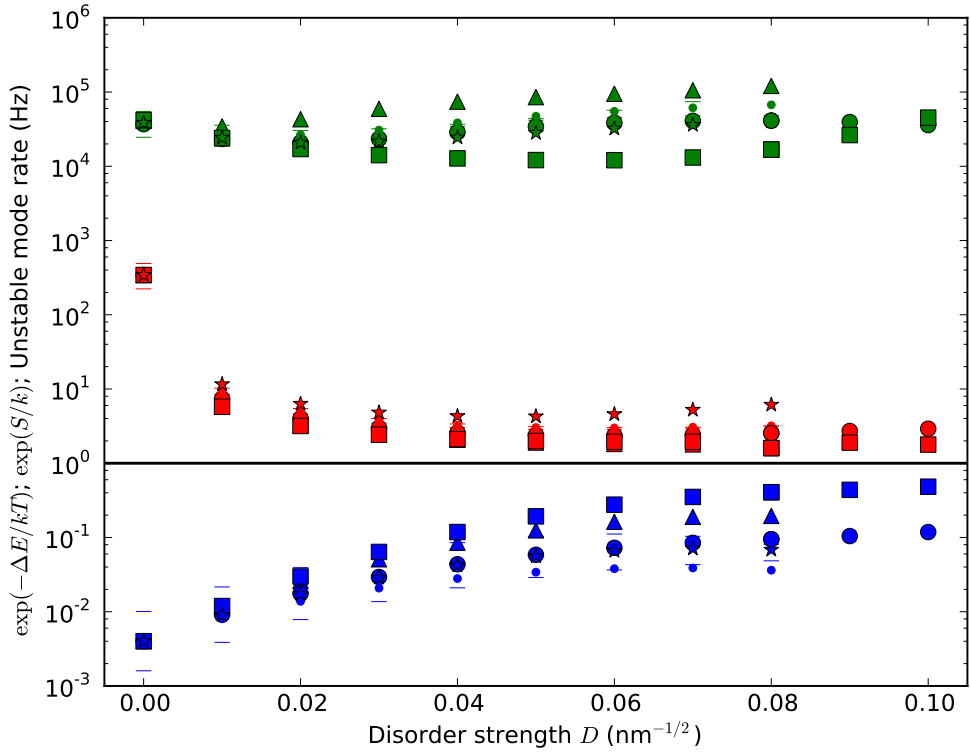
## Results with disorder

Figure 4.6 displays our results for the hopping rate and effective free energy barrier as a function of the intrinsic bend disorder strength  $D$ , for  $D$  in the range corresponding to experimental estimates of the persistence length  $P$ . The hopping rate is calculated using Eq. (4.20) at zero disorder and Eq. (4.30) with disorder (in this case summing over 10 saddle points — see Section 5.3.4 for details). The effective free energy barrier is calculated using Eq. (4.22) (using the average  $\lambda_b$  over the 10 saddle locations). We see first that the nucleation rate is not significantly altered by the intrinsic disorder, remaining between  $10^4$  and  $10^5$  Hz. The effective free energy barrier, however, rises with increasing disorder, though it remains slightly below our lower bound of  $2 kT$  even at the larger experimental estimate for intrinsic disorder (green dashed line). Thus disorder makes our calculation more physically plausible, but the rate remains too fast, and the free energy barrier too low.

In Figure 4.7, we plot the components that contribute to the rate, defined in Eq. (4.21): the dynamic factor  $\lambda_b$  (green), the entropic factor  $\exp(S/k)$  (red), and the energetic factor  $\exp(-\Delta E/kT)$  (blue). To explore the variance caused by sequence dependence, we calculate these factors for five different random intrinsic bend sequences, for a single plectoneme location  $s$  (here, the location  $s^*$  predicted to have the lowest energy barrier by first-order perturbation theory; see Section 5.3.1). Though the sequence dependence does create some spread in the factors, it is not alone enough to explain the discrepancy with the experimental hopping rate, especially since two groups using presumably different DNA sequences found similar results.



**Figure 4.6: Hopping rate and effective free energy barrier vs. disorder magnitude.** The green dashed line corresponds to one experimental estimate of the bending order persistence length,  $P = 130$  nm [4], and the blue hatched region corresponds to another,  $P > 1000$  nm [76]. The hopping rate  $k_{\text{hopping}}$  (top) does not change significantly with the addition of intrinsic bend disorder. The effective free energy barrier  $\Delta\mathcal{F}$  (bottom) increases, coming closer to but not crossing the lower bound of  $2 kT$  found using the distribution in Figure 4.4.



**Figure 4.7: Hopping rate factors vs. disorder magnitude for different sequences.** (Blue) Energetic factor  $\exp(-\Delta E/kT)$ ; (Red) entropic factor  $\exp(S/k)$  (for the one best plectoneme location  $s^*$  when  $D > 0$ ); (Green) dynamic factor  $\lambda_b/2\pi$ , in Hz. Different solid markers correspond to five different random seeds (five different basepair sequences). Horizontal bars correspond to varying the bend elastic constant  $B$  for one of the sequences by adding and subtracting the uncertainty in its measurement,  $(3 \text{ nm})kT$ . On this log scale, adding the three distances from the horizontal line at  $10^0$  produces the final contribution to the rate from location  $s^*$ . Note that the entropic factor (which is further increased by including multiple plectoneme locations) largely cancels the slowing from the energy barrier factor. Note also that we do not expect the variance from sequence dependence or uncertainty in the elastic constants to explain the three orders of magnitude difference between theory and experiment.

#### 4.4.2 Uncertainties in elastic constants

Since the hopping rate is exponentially sensitive to energy scales at the transition, it will be important to carefully consider our knowledge of the true elastic constants  $B$  and  $C$ . Our values [  $B = (43 \pm 3 \text{ nm})kT$  and  $C = (89 \pm 3 \text{ nm})kT$  ] were obtained directly from the same experimental setup that produced the hopping data [27], and come from fitting force-extension data to the worm-like chain model [81]. The uncertainties in parameters correspond to ranges of rate predictions — we numerically check these ranges by performing the rate calculation using both the upper and lower limits of the ranges for the quoted value of the two elastic constants. We find that changes in the elastic constants mainly affect the rate through the energy barrier  $\Delta E$  [Eq. (4.7)], which is much more sensitive to  $B$  than to  $C$ . The horizontal bars in Figure 4.7 show the results of changing  $B$  from its lower to its upper limit; we see that the uncertainty in the bending elastic constant produces variations on the same scale as the sequence dependence. This is, again, not enough to explain the discrepancy with experiment, though combined with the bound on the free energy barrier mentioned above, it hints that a better understanding of the energetics at the barrier is needed.<sup>14</sup>

### 4.5 Discussion and conclusions

To calculate the rate for plectoneme nucleation at the supercoiling transition, we use an elastic rod theory to characterize the saddle state corresponding to the barrier to hopping. Using reaction rate theory, we then calculate the rate prefactor,

---

<sup>14</sup> We note in passing that increasing the microscopic bend elastic constant  $B_m$  by a factor of nearly 2 to  $(80 \text{ nm})kT$  raises the energy barrier above  $10 \text{ kT}$  and lowers the hopping rate to about 20 Hz for  $D = 0.03 \text{ nm}^{-1/2}$ . This rate agrees with experiments, but we do not know of a reason that  $B_m$  would need to be increased this much above the experimentally measured  $B$ .

including entropic factors and hydrodynamic effects. We also analyze the effect of intrinsic bend disorder, which simultaneously lowers the energy barrier and increases the entropic barrier. We find a hopping rate that is about 1000 times faster than what is seen in experiments.

Insight is gained by studying the factors that contribute to the rate. First, the energy barrier is calculated analytically using elastic theory [Eq. (4.7)]. Second, the rate of motion at the barrier top can be obtained in the full calculation, and the order of magnitude ( $10^5$  Hz) agrees with the expected rate of motion of a rod in a viscous fluid when inserting the appropriate length and energy scales. Third, the entropic contribution to the prefactor lowers the free energy barrier to small values (at most about  $1.5 kT$ ), in a way directly related to the saddle configuration's translational zero mode. Finally, from the experimental observations of bistability, we know that the size of the barrier should be larger than our theory predicts (Figure 4.4). This contributes to the faster hopping rate resulting from our calculation.

Exploring possible corrections to the calculation, we developed a method to include intrinsic bends by numerically locating the saddle point configurations. Intrinsic bends do not significantly change the hopping rate, though they do slightly increase the effective free energy barrier (Figure 4.6). Both sequence dependence and uncertainties in the elastic parameters produce variations in the rate, but they are not large enough to slow the hopping rate by three orders of magnitude.

We have a good understanding of the components that contribute to the rate: the energy barrier is straightforwardly computable, the rates of dynamics for the unstable mode agree with order-of-magnitude estimates, and the entropic terms are of a reasonable magnitude. Our results suggest that there is something more

fundamentally incorrect about our understanding of the energetics of DNA bending at the scale of the soliton bump ( $\ell \sim 10$  nm). Specifically, based on both the slow rate and the magnitude of bistability, we conclude that the energy of the saddle state predicted by elastic theory is incorrectly small.

CHAPTER 5  
NUMERICAL ALGORITHMS FOR DNA SUPERCOILING

## 5.1 Introduction

As described in Section 1.2.2, we model DNA as an inextensible elastic rod. This chapter describes the numerical algorithms used to calculate energy and forces on DNA configurations, as well as the methods used to incorporate intrinsic DNA bends and locate transition state saddle points.

## 5.2 Calculating the energy of a DNA configuration

In our numerical calculations, we approximate the continuous elastic rod as a discretized chain of segments, each with fixed length  $d$ . The orientation of each segment is described by the rotations necessary to transform the global Cartesian axes onto the local axes of the segment. When minimizing the (free) energy, we

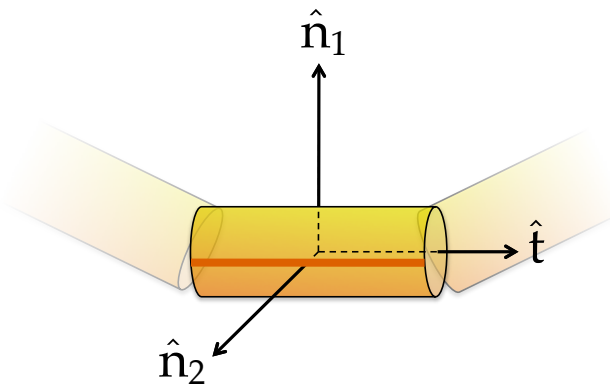


Figure 5.1: Local basis vectors.

find it convenient to use Euler angles<sup>1</sup>  $\phi, \theta$ , and  $\psi$ , since any set of Euler angles specifies a valid configuration.<sup>2</sup> However, writing the energy in terms of differences of Euler angles can lead to numerical problems near the singularities at the poles. When calculating energies and forces, we therefore instead use the full rotation matrix  $R$ .  $R$  rotates a segment lying along the  $z$ -axis to its final orientation;  $R$ 's columns are thus the two normal unit vectors followed by the tangent unit vector:

$$R^{(n)} = \begin{bmatrix} \hat{n}_1^{(n)} & \hat{n}_2^{(n)} & \hat{t}^{(n)} \end{bmatrix} \quad (5.1)$$

$$\begin{aligned} \hat{n}_1 = & (\cos \phi \cos \psi - \cos \theta \sin \phi \sin \psi, \\ & -\cos \psi \sin \phi - \cos \theta \cos \phi \sin \psi, \\ & \sin \theta \sin \psi), \\ \hat{n}_2 = & (\cos \theta \cos \psi \sin \phi + \cos \phi \sin \psi, \\ & \cos \theta \cos \phi \cos \psi - \sin \phi \sin \psi, \\ & -\cos \psi \sin \theta), \\ \hat{t} = & (\sin \theta \sin \phi, -\cos \psi \sin \theta, \cos \theta). \end{aligned} \quad (5.2)$$

There are three degrees of freedom in the “hinge” between each segment that determine the local elastic energy: the two components of bending  $\beta_1$  and  $\beta_2$  (along  $\hat{n}_1$  and  $\hat{n}_2$ , respectively), and the twist  $\Gamma$ . In terms of the rotation matrix

$$\Delta^{(n)} \equiv (R^{(n)})^T R^{(n+1)}, \quad (5.3)$$

which measures the rotation between adjacent segments, mapping the  $n$ th segment's axes onto those of the  $(n+1)$ th, the bends and twist can be written in an

---

<sup>1</sup> We use the ‘z-x-z’ convention:  $\psi$  rotates about the original  $z$ -axis,  $\theta$  rotates about the original  $x$ -axis, and  $\phi$  rotates about the new  $z$ -axis.

<sup>2</sup> Other parameterizations with more degrees of freedom (such as rotation matrices or Cartesian coordinates paired with a local twist) would require constraints to ensure a valid configuration with no stretching.

explicitly rotation-invariant form: to lowest order in the angles (see Section 5.4.3),

$$\beta \cdot \hat{n}_1 = \beta_1 = (\Delta_{23} - \Delta_{32})/2 \quad (5.4)$$

$$\beta \cdot \hat{n}_2 = \beta_2 = (\Delta_{31} - \Delta_{13})/2 \quad (5.5)$$

$$\Gamma = (\Delta_{12} - \Delta_{21})/2, \quad (5.6)$$

where the  $(n)$  superscripts have been omitted. The above forms are useful when the sign of a given component is necessary.<sup>3</sup> Otherwise, the following squared forms may be used, which have the advantage of a larger range of validity away from zero (see Section 5.4.3):

$$\vec{\beta}^2 = \beta_1^2 + \beta_2^2 = 2(1 - \Delta_{33}) \quad (5.7)$$

$$\Gamma^2 = 1 - \Delta_{11} - \Delta_{22} + \Delta_{33}. \quad (5.8)$$

Our energy function is then the discretized version of Eq. (1.3):

$$E_{\text{elastic}} = \frac{1}{2d} \sum_m B \vec{\beta}_m^2 + C \Gamma_m^2, \quad (5.9)$$

or, separating the bend into its two components,

$$E_{\text{elastic}} = \frac{1}{2d} \sum_m B(\vec{\beta}_m \cdot \hat{n}_1^{(m)})^2 + B(\vec{\beta}_m \cdot \hat{n}_2^{(m)})^2 + C \Gamma_m^2. \quad (5.10)$$

### 5.3 Transition state calculations

#### 5.3.1 Including disorder

As discussed in Section 4.4.1, we need to include DNA's intrinsic bend disorder to understand the energetics of the saddle point barrier crossing. To accomplish this,

---

<sup>3</sup> We will use this, for example, when we break the symmetry between positive and negative bends with the introduction of intrinsic bend disorder.

we shift the zero of the elastic bend energy for each hinge; generalizing Eq. (5.10),

$$E_{\text{bend}} = \frac{B}{2d} \sum_m ((\vec{\beta}_m - \sigma_b \vec{\xi}_m) \cdot \hat{n}_1^{(m)})^2 + ((\vec{\beta}_m - \sigma_b \vec{\xi}_m) \cdot \hat{n}_2^{(m)})^2. \quad (5.11)$$

For each  $i$ , we choose each of the two components of  $\xi$  from a normal distribution with unit standard deviation. We then need to relate  $\sigma_b$  to the resulting intrinsic bend persistence length  $P$ . The persistence length is defined by the decay of orientation correlations:

$$\langle \hat{t}(0) \cdot \hat{t}(s) \rangle = \langle \cos \theta(s) \rangle = e^{-s/P}, \quad (5.12)$$

where  $\theta(s)$  is the angle between segments separated by arclength  $s$  [4]. For small  $s$  [and thus small  $\theta(s)$ ], Eq. (5.12) becomes

$$1 - \frac{1}{2} \langle \theta(s)^2 \rangle = 1 - \frac{s}{P}. \quad (5.13)$$

At zero temperature and zero force, the size of  $\langle \theta(s)^2 \rangle$  is set by the intrinsic bends  $\xi_m$  only; we are doing a random walk in two dimensions with one step of root-mean-square size  $\sqrt{2}\sigma_b$  taken for every segment of length  $d$ . Thus  $\langle \theta(s)^2 \rangle = 2\frac{s}{d}\sigma_b^2$ , which when inserted into Eq. (5.13) gives the desired relation between persistence length  $P$  and the size of individual random bends  $\sigma_b$ :

$$P = \frac{d}{\sigma_b^2}. \quad (5.14)$$

We will also define a convenient parameter  $D$  controlling disorder strength that is independent of the segment length  $d$ :

$$D \equiv \frac{\sigma_b}{\sqrt{d}}, \quad (5.15)$$

such that

$$P = D^{-2}. \quad (5.16)$$

## First order changes in the energy barrier

How does disorder change the energy of the saddle point? Since the disorder changes only the bending energy, we can find the lowest order change from the zero disorder energy by taking the derivative of Eq. (5.11) with respect to disorder strength  $\sigma_b$  at  $\sigma_b = 0$ :

$$\begin{aligned} \frac{dE}{d\sigma_b} \Big|_{\sigma_b=0} &= \frac{dE_{\text{bend}}}{d\sigma_b} \Big|_{\sigma_b=0} = -\frac{B}{d} \sum_m (\vec{\beta}_m \cdot \hat{n}_1^{(m)}) (\vec{\xi}_m \cdot \hat{n}_1^{(m)}) + (\vec{\beta}_m \cdot \hat{n}_2^{(m)}) (\vec{\xi}_m \cdot \hat{n}_2^{(m)}) \\ &= -\frac{B}{d} \sum_m \vec{\beta}_m \cdot \vec{\xi}_m, \end{aligned} \quad (5.17)$$

or, in terms of disorder strength  $D$  defined in Eq. (5.15),

$$\frac{dE}{dD} \Big|_{D=0} = -\frac{B}{\sqrt{d}} \sum_m \vec{\beta}_m \cdot \vec{\xi}_m. \quad (5.18)$$

We will specifically be interested in the derivative of the saddle configuration's energy, which will depend on its location  $s$  and rotation  $\rho$ . Noting that  $\rho$  will simply rotate the bend vector  $\vec{\beta}$ , we can write down the form of the dependence on  $\rho$ :

$$E'_{\text{saddle}}(s, \rho) \equiv \frac{dE_{\text{saddle}}(s, \rho)}{dD} \Big|_{D=0} = -A(s) \cos(\rho - \rho^*(s)) \quad (5.19)$$

for some  $A(s)$  and  $\rho^*(s)$ .  $A(s)$  gives the maximum derivative (sensitivity to disorder) at position  $s$ , and  $\rho^*(s)$  is the preferred rotation of the saddle that gives the maximum (negative) derivative. We can find  $A(s)$  and  $\rho^*(s)$  numerically using the derivative calculated at two values of  $\rho$  separated by  $\pi/2$ :

$$A(s) = \sqrt{(E'_{\text{saddle}}(s, 0))^2 + (E'_{\text{saddle}}(s, \pi/2))^2} \quad (5.20)$$

$$\rho^*(s) = \arctan \left( \frac{E'_{\text{saddle}}(s, \pi/2)}{E'_{\text{saddle}}(s, 0)} \right). \quad (5.21)$$

Figure 5.2 shows a typical  $A$  as a function of  $s$ . Figure 5.3 compares the first-order approximation to the saddle energy at the location  $s^*$ , given by  $DA(s^*)$ ,

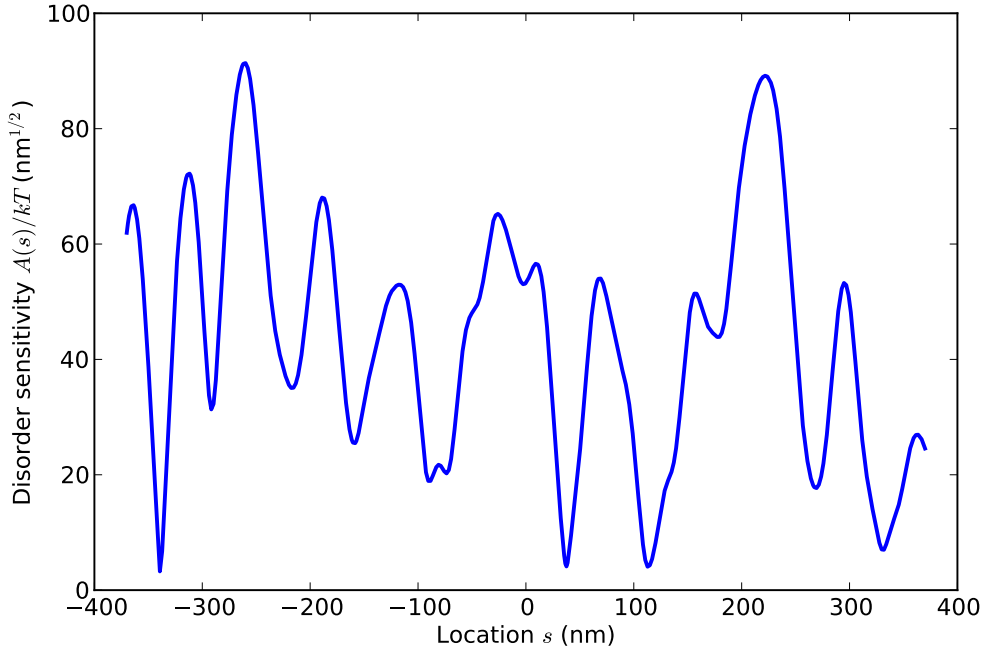


Figure 5.2: **Sensitivity of saddle energy to disorder.** Typical sensitivity of saddle energy to disorder strength as a function of position, for  $L = 740$  nm. Peaks indicate positions where plectoneme nucleation is energetically favored.

to  $E_{\text{saddle}}$  calculated numerically by zeroing forces (see Section 5.3.4). We see that the approximation correctly predicts the scale of the change for the disorder sizes in which we are interested, but overestimates the change by many  $kT$  for large disorder. We therefore use the first-order approximation to find the likely locations of the lowest energy saddle points [at the peaks of  $A(s)$ ], and then zero the forces numerically.

To estimate the typical size of this sensitivity to disorder, we first note that the bend magnitude for the saddle configuration is [inserting Eqs. (4.4) into Eq. (5.32)]

$$|\vec{\beta}_{\text{saddle}}| = \frac{2d}{\ell} \operatorname{sech}\left(\frac{s}{\ell}\right). \quad (5.22)$$

Approximating the function  $\operatorname{sech}(x)$  as 1 in the range  $-2 < x < 2$  and 0 elsewhere,

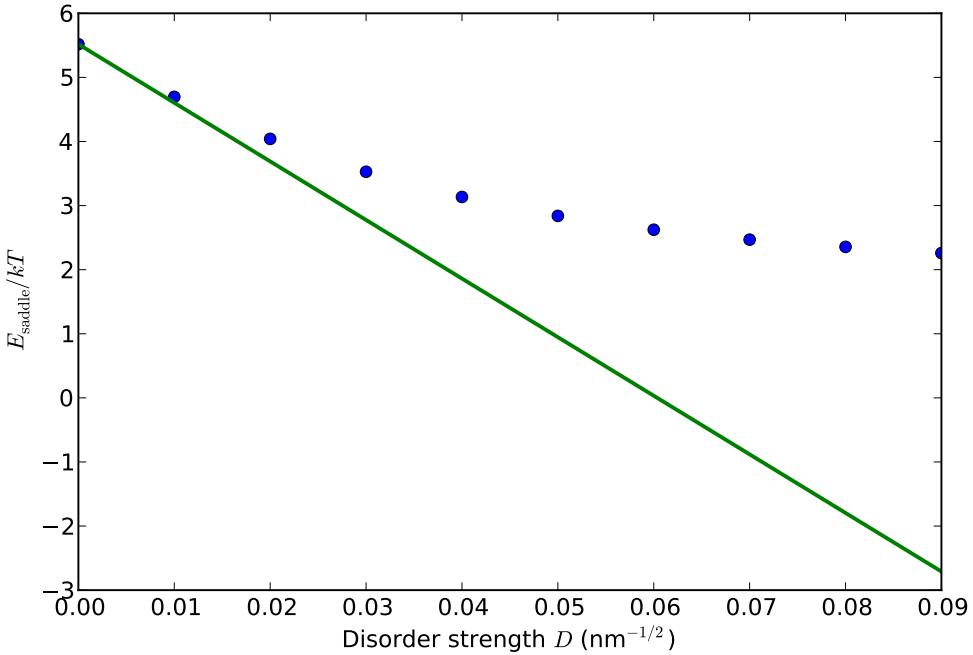


Figure 5.3: **Saddle energy vs. disorder strength.** The lowest saddle energy as a function of disorder strength  $D$ . The blue dots are the true saddle energies, calculated by numerically zeroing forces on the saddle configuration. The green line represents the first-order approximation given by  $DA(s^*)$ ; we see that the approximation correctly predicts the scale of the change, but overestimates it by many  $kT$  at large disorder.

Eq. (5.18) becomes

$$\left. \frac{dE_{\text{saddle}}}{dD} \right|_{D=0} \approx -\frac{B}{\sqrt{d}} \frac{2d}{\ell} \sum_{n=0}^{4\ell/d} \xi_m \quad (5.23)$$

for randomly distributed  $\xi$  with unit variance, which produces

$$\sqrt{\langle \left( \frac{dE_{\text{saddle}}}{dD} \right)^2 \rangle} \approx \frac{4B}{\sqrt{\ell}}. \quad (5.24)$$

Inserting  $B = (43 \text{ nm})kT$  and  $\ell \approx 10 \text{ nm}$  gives a typical sensitivity of about  $(50 \text{ nm}^{1/2})kT$ , agreeing with the scale found in the full calculation, as shown in Figure 5.2.

### 5.3.2 Changing to the correct coordinates

So far, we have used Euler angles  $(\phi, \theta, \psi)$  to parametrize the DNA configuration. We can easily calculate energy derivatives with respect to these coordinates. However, the hopping rate calculation requires that we do our path integral in the same coordinates as the dynamics, given in Section 4.2.3, which are defined in Cartesian space with a local twist  $[\vec{r} = (x, y, z, \psi)]$ . To efficiently calculate the correct hessian, then, we need to convert energy derivatives to  $\vec{r}$  space.

First, we note that there is one less coordinate in Euler angle space: this comes from the inextensibility constraint, which  $\vec{r}$  space does not have. Thus we add a coordinate  $\Delta$  to the Euler angles specifying the length of each segment (which will usually be set to a constant  $d$ ); we will call this set of coordinates  $\vec{\alpha} = (\phi, \theta, \psi, \Delta)$ . Also,  $\vec{r}$  has  $N + 1$  elements, each defining the location of one end of a segment, while  $\vec{\alpha}$  has  $N$  elements, each defining the Euler angles and length of each segment. To match the number of degrees of freedom, we remove center of mass motion and set constant orientation boundary conditions by fixing the location of the first segment's two ends and fixing the last segment's orientation along  $\hat{z}$ :  $\vec{r}(0) = \vec{0}$ ,  $\vec{r}(1) = d\hat{z}$ ,  $\vec{r}(N+1) = \vec{r}(N) + d\hat{z}$ . This gives a total of  $4(N - 2)$  degrees of freedom.

The Jacobian we would like to calculate is

$$J_{mi,nj} = \frac{d\vec{\alpha}_{mi}}{d\vec{r}_{nj}}, \quad (5.25)$$

where  $m$  and  $n$  label segments and  $i$  and  $j$  label components. First writing the

Euler angles for a given segment  $n$  in terms of  $\vec{t}_n = (x, y, z)_{n+1} - (x, y, z)_n$ ,

$$\phi = \arctan(-t_y/t_x) \quad (5.26)$$

$$\theta = \arccos\left(t_z/\sqrt{t_x^2 + t_y^2 + t_z^2}\right) \quad (5.27)$$

$$\Delta = \sqrt{t_x^2 + t_y^2 + t_z^2}. \quad (5.28)$$

We then take derivatives with respect to Cartesian coordinates to produce the  $\phi$ ,  $\theta$ , and  $\Delta$  rows in the Jacobian. A subtlety arises in finding expressions for derivatives of the Euler angle  $\psi$  with respect to Cartesian coordinates. We would like the derivative to correspond to rotating the adjacent segments to accommodate the change in the location of their connecting ends. Due to the way in which Euler angles are defined, this rotation does not in general leave  $\psi$  unchanged, as one might naively expect. We therefore obtain the derivatives of  $\psi$  by first writing the rotation matrix corresponding to infinitesimal motion in Cartesian space and then calculating the corresponding change in  $\psi$ . This produces the nonzero terms in the  $\psi$  row of  $J_1$  below.

In the end, we have

$$J_{mn} = \delta_{m,n} [J_1(m) + J_2] - \delta_{m,n+1} J_1(m), \quad (5.29)$$

where (including the names of the components for clarity)

$$J_1(n) \equiv \begin{array}{c|cccc} & x & y & z & \psi \\ \hline \phi & -t_y/p & t_y/p & 0 & 0 \\ \theta & t_x t_z/p \Delta^2 & t_y t_z/p \Delta^2 & -p/\Delta^2 & 0 \\ \psi & t_y t_z/p^2 \Delta & -t_x t_z/p^2 \Delta & 0 & 0 \\ \Delta & t_x/\Delta & t_y/\Delta & t_z/\Delta & 0 \end{array}, \quad (5.30)$$

$p \equiv \sqrt{\Delta^2 - t_z^2}$ ,  $J_2 \equiv \delta_{\psi,\psi}$ , and all the components are evaluated at location  $n$ .

We use this Jacobian to transform forces with respect to angles  $\vec{\alpha}$  to forces with

respect to  $\vec{r}$ , which are then used to assemble the Hessian for use in calculating the unstable mode and the entropic factors for the transition state calculation in Section 4.2.4.

### 5.3.3 Other subtleties

Since derivatives in  $\vec{r}$  space will in general couple to  $\Delta$  (changing the lengths of segments), we also include an extra stretching energy:

$$E_{\text{stretching}} = \frac{S}{2} \sum_n (\Delta_n - d)^2. \quad (5.31)$$

This avoids problems with extra zero modes corresponding to changing  $\Delta$ . We may choose the stretch elastic constant  $S$  to match DNA (in which case it should be about 1000 pN [81]); but since  $S$  is so large compared to the other elastic constants, the stretching modes have much higher energy and are the same for the straight and saddle configurations, canceling in the rate equation [e.g. Eq. (4.19)]. Thus we find that our results are insensitive to the exact value of  $S$ , as expected.

As can be seen by inserting  $\vec{t} = (0, 0, 1)$  into Eq. (5.30), there are singularities in the Jacobian when  $\vec{t}$  points along the  $z$ -axis. This corresponds to the singularity in the Euler angle representation at the poles (when  $\theta = 0$ ,  $\phi$  and  $\psi$  are degenerate). This is a problem for our formulation because our usual boundary conditions hold the ends in the  $\hat{z}$  direction. As pointed out in Ref. [43], a simple way to avoid this problem is to rotate the system away from the singularity (rotating the direction of the force as well). When performing calculations that require the Jacobian, we therefore rotate the system about the  $y$ -axis by an angle  $\beta$  and modify the external force term in the energy from  $-F \cos \theta$  to  $-F(\cos \beta \cos \theta + \sin \beta \sin \theta \sin \phi)$ . This

more general formulation also permits an explicit check that our energies and derivatives are rotation invariant.

The Hessian is constructed by taking numerical derivatives of forces, which can be calculated analytically. This gives the Hessian as a  $4(N - 2) \times 4(N - 2)$  matrix, which is diagonalized to find eigenvalues for the entropic calculation [Eq. (4.19)]. At zero disorder, the zero modes must first be removed; numerically, we find that the zero modes show up conveniently as the two modes with smallest eigenvalues, a few orders of magnitude smaller than any others.

### 5.3.4 Finding saddle points

With large disorder, the saddle points must be found numerically. We start by estimating the set of saddle locations  $\{s^*\}$  and rotations  $\{\rho^*\}$  using first order perturbation theory (Section 5.3.1). We find the local maxima of  $A(s)$  using a one-dimensional local search method starting from a set of points spaced by the saddle configuration length scale  $\ell$ . This gives  $\{s^*\}$ , from which  $\{\rho^*\}$  can be found using Eq. (5.21). For each  $s^*$  and corresponding  $\rho^*$ , we create a zero-disorder saddle configuration [Eqs. (4.4)], and then use this as the starting point for a multidimensional equation solver (`scipy.fsolve`) that numerically locates the saddle with disorder by finding solutions with zero net force on each segment.

We also find that at zero disorder, the analytical saddle configurations from Eqs. (4.4) do not produce states with precisely zero forces — we attribute this to the effects of discretization. We therefore first minimize the forces using the same procedure even at zero disorder.

Table 5.1: Repulsive interaction parameters.

Symbol	Description	Value
$\nu$	effective # of electron charges per unit length	8.4 nm <sup>-1</sup> [48]
$\lambda_D$	Debye screening length	0.8 nm [48]
$e_-^2/\epsilon$	squared electron charge / permittivity of water	2.9 pN nm <sup>2</sup> [48]
$B_{\text{eff,entropic}}$	Entropic repulsion effective bend modulus	26.8 pN nm <sup>2</sup>
$B_{\text{eff,coulomb}}$	Coulomb repulsion effective bend modulus	16.6 pN nm <sup>2</sup>
$B_{\text{eff}}$	Total repulsion effective bend modulus	43.4 pN nm <sup>2</sup>

## 5.4 Numerical details

### 5.4.1 Choosing $d$

As shown in Figure 5.4, we must be careful to choose our discretization length (the length  $d$  of each segment) such that our energy calculations are sufficiently accurate. We can check the accuracy of the discretized energy calculation by comparing with the analytical energy barrier in Eq. (4.7). Choosing  $d = 1$  nm produces energy barriers within 0.2 $kT$  of the continuum limit (corresponding to 20% changes in the hopping rate) with reasonable memory and time expenditure.

### 5.4.2 Correcting for renormalization of $B$ due to repulsive interaction

As described in Section B.3, we use both electrostatic and effective entropic repulsive interactions between each segment in the strand for the calculations in

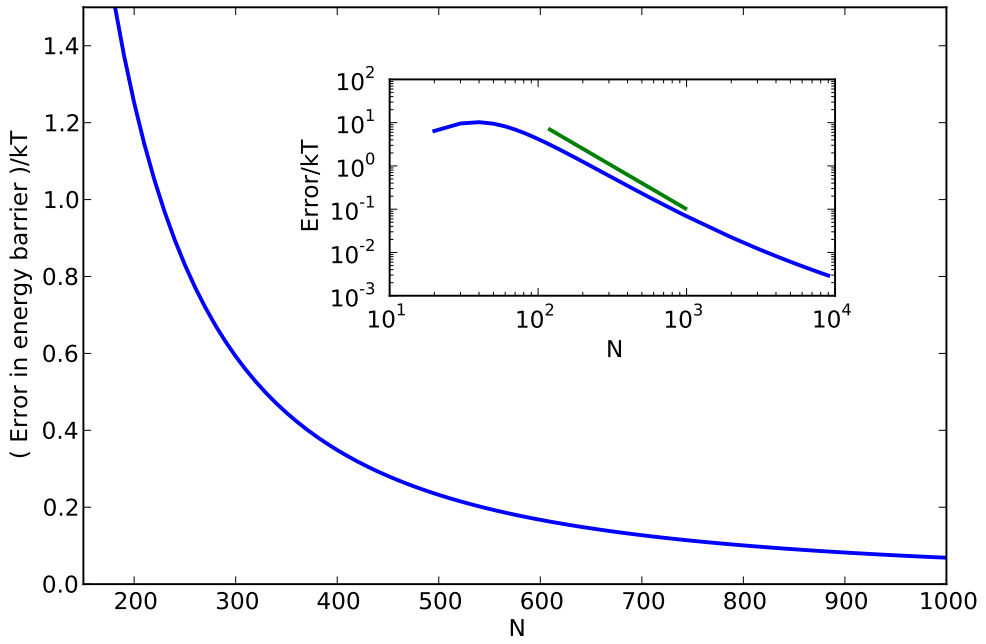


Figure 5.4: **Choosing  $d$ .** Error in the discretized energy barrier [comparing to the exact result in Eq. (4.7)] as a function of the number of discrete segments  $N$  (for  $L = 740$  nm and other parameters as in Table 4.1). Inset: the same data on a log-log plot. The green line has a slope of  $-2$ , showing convergence proportional to  $1/N^2$ . We choose  $N = 740$  ( $d = 1$  nm) as a good trade-off between accuracy and required computational resources.

Chapter 3, such that two segments of the strand cannot pass through each other. The presence of short-range repulsive interactions also creates a local force encouraging the strand to straighten, renormalizing the bend elastic constant. To correct for this effect, we subtract off the effective bend elastic constants arising from the electrostatic and entropic repulsion alone. First imposing sinusoidal bends with wavenumber  $k$  and amplitude  $A$ , we numerically measure the repulsive energy as either  $k$  or  $A$  is varied. Fitting to  $E = A^2 k^2 L B_{\text{eff}}/2$ , we find the effective bend elastic constant  $B_{\text{eff}}$  — we then use  $B - B_{\text{eff}}$  as the microscopic bend elastic constant when repulsive interactions are used, to give the correct total renormalized

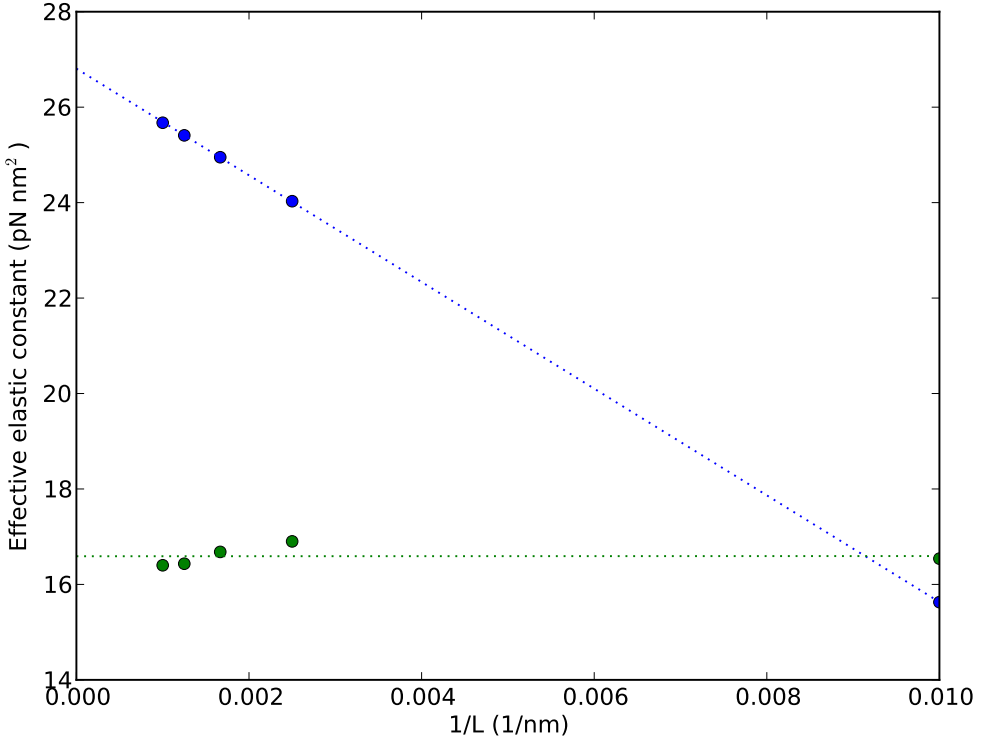


Figure 5.5: **Extrapolation of elastic constant renormalization.** The effective elastic constants produced by entropic repulsion alone (blue) and Coulombic repulsion alone (green) are plotted as circles as a function of  $1/L$ . Linear fits (dotted lines) extrapolate to the infinite length values (at  $1/L = 0$ ) that are given in Table 5.1 and used to correct for the renormalization caused by the repulsive terms.

value. Since this procedure depends in general on the length  $L$  of the strand used, we (numerically) take the  $L \rightarrow \infty$  limit, as shown in Figure 5.5. This results in the values listed in Table 5.1. Note that these values depend on the discretization length  $d$ , here 1 nm.

### 5.4.3 Deriving rotation-invariant forms for bend and twist

The amount of local bend and twist can be measured by differences in the rotation matrices of adjacent segments. We would like expressions in terms of the rotation matrices that are correct to lowest order in the bend or twist angle and that are explicitly rotation invariant. Our procedure will be to form rotation invariant terms and, writing them in terms of Euler angles and their derivatives, check what they measure in terms of bend and twist.

We can first write the bend and twist in terms of derivatives of the local basis vectors (see Figure 5.1) or Euler angles [23]:

$$\beta^2 = \left[ \dot{\vec{t}} \right]^2 = \dot{\phi}^2 \sin^2 \theta + \dot{\theta}^2 \quad (5.32)$$

$$\Gamma^2 = \left[ (\vec{n} \times \dot{\vec{n}}) \cdot \vec{t} \right]^2 = \left( \dot{\phi} \cos \theta + \dot{\psi} \right)^2. \quad (5.33)$$

We then form rotation-invariant terms from rotation matrices and compare their Taylor series expansions with respect to bend and twist angles to Eq. (5.32) and Eq. (5.33). First checking  $\text{Tr}[(R^{(n+1)} - R^{(n)})^T (R^{(n+1)} - R^{(n)})]$ , we find that

$$\beta^2 + \Gamma^2 = \frac{1}{2} \left( R_{\alpha\beta}^{(n)} - R_{\alpha\beta}^{(n+1)} \right) \left( R_{\alpha\beta}^{(n)} - R_{\alpha\beta}^{(n+1)} \right) = 3 - \Delta_{11} - \Delta_{22} - \Delta_{33}. \quad (5.34)$$

Next we check the dot product of the difference in the tangent unit vector  $\hat{t}$ :

$$\beta^2 = \delta \hat{t} \cdot \delta \hat{t} = \left( R_{\alpha 3}^{(n)} - R_{\alpha 3}^{(n+1)} \right) \left( R_{\alpha 3}^{(n)} - R_{\alpha 3}^{(n+1)} \right) = 2(1 - \Delta_{33}). \quad (5.35)$$

Eq. (5.34) and Eq. (5.35) produce Eq. (5.7) and Eq. (5.8).

To find expressions for signed  $\beta$  and  $\Gamma$ , we notice that the above use only the diagonal elements of  $\Delta$ ; we can also form rotation invariant terms using the

off-diagonal elements, producing (with the Levi-Civita symbol  $\varepsilon$ )

$$\beta_1 = \varepsilon_{1\gamma\delta} \Delta_{\gamma\delta}/2 = (\Delta_{23} - \Delta_{32})/2 \quad (5.36)$$

$$\beta_2 = \varepsilon_{2\gamma\delta} \Delta_{\gamma\delta}/2 = (\Delta_{31} - \Delta_{13})/2 \quad (5.37)$$

$$\Gamma = \varepsilon_{3\gamma\delta} \Delta_{\gamma\delta}/2 = (\Delta_{12} - \Delta_{21})/2. \quad (5.38)$$

We can see the benefit of using the squared forms [Eq. (5.7) and Eq. (5.8)] by checking their dependence on pure bending or twisting rotations. For example, with two segments differing only in twist, such that  $\psi^{(n+1)} = \psi^{(n)} + \alpha$ , we find that Eq. (5.6) and Eq. (5.8) produce, respectively,<sup>4</sup>  $\Gamma = \sin \alpha$  and  $\Gamma^2 = 2(1 - \cos \alpha)$ . Plotting  $\Gamma^2$  for the two cases (Figure 5.6) demonstrates that they have the same curvature near  $\alpha = 0$  (by design), but using the non-squared version in Eq. (5.6) leads to a second minimum at  $\alpha = \pi$ : we find that, especially when including intrinsic bend disorder, this can cause the numerical minimizer to allow  $\psi$  to slip by  $\pi$  to the next minimum, unphysically removing linking number. For this reason, we use the squared forms unless otherwise necessary.

---

<sup>4</sup> These are straightforwardly evaluated by noting that, e.g.,  $\Delta_{12} = \hat{n}_1^{(n)} \cdot \hat{n}_2^{(n+1)}$ .

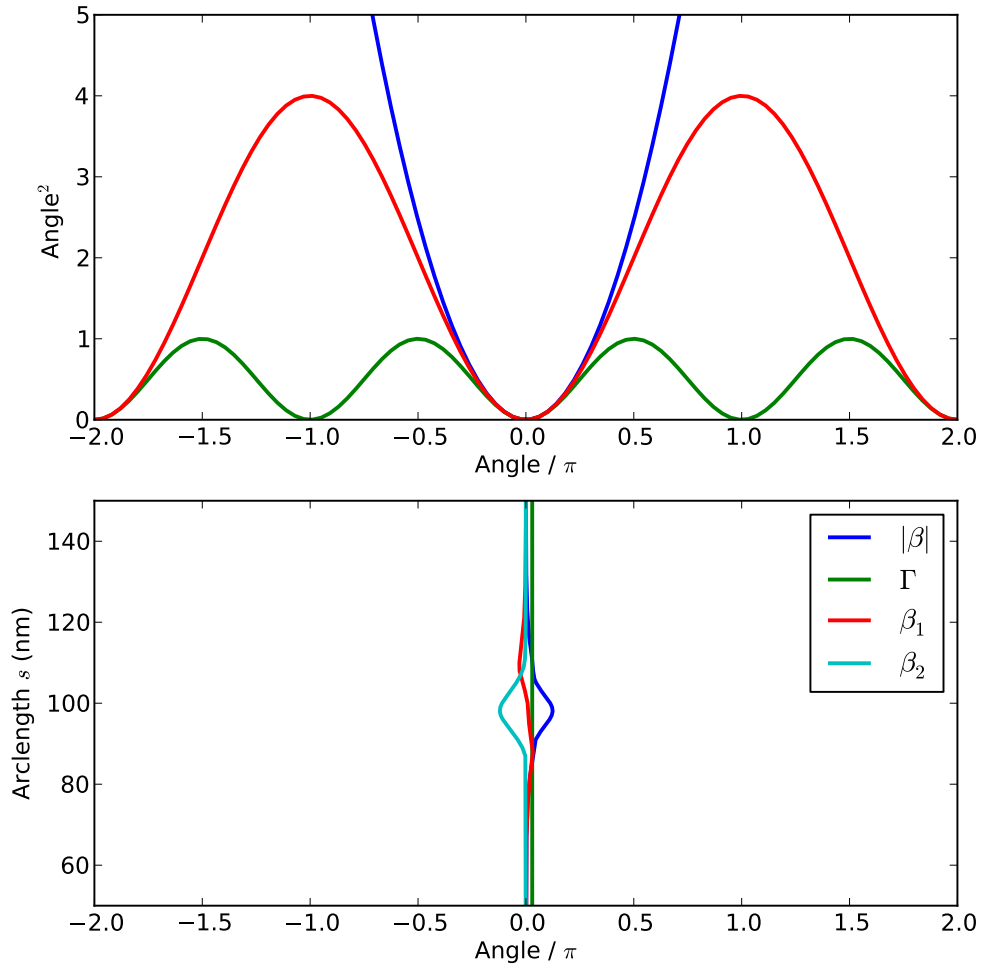


Figure 5.6: **Checking bend and twist expressions.** (top) Two different rotation-invariant approximations to the bend or twist angle squared (green and red) compared to the actual angle squared (blue). Using the non-squared version (green) leads to a smaller range of validity. (bottom) Typical magnitude of bend and twist angles for a plectoneme (for  $F = 2$  pN,  $d = 1$  nm). Note that the bend and twist angles stay within the region where either approximation should be valid.

APPENDIX A  
**SUPPLEMENTARY MATERIAL FOR CHAPTER 2**

## A.1 Contents

The contents of the supplemental material are organized corresponding to the order of Chapter 2. Included in the supplemental material are derivations of mathematical results and details of the specific models mentioned in Chapter 2.

We have also posted the data files and computer codes for the models discussed, at <http://www.lassp.cornell.edu/seethna/Sloppy>. For the KaiC, PC12, and segment polarity models, this includes:

1. Equations in L<sup>A</sup>T<sub>E</sub>X, Python, and C
2. SBML (system biology markup language) files
3. Parameter ensembles
4. Best-fit Hessian and  $J^T J$ , and their eigenvectors and eigenvalues

## A.2 Introduction

### A.2.1 Hessian at best fit parameters

In the introduction we mention that “the curvature of the cost surface about a best fit set of parameters is described by the Hessian  $H_{mn}$ .” Examining the behavior of  $H_{mn}$  is a standard method for nonlinear least squares models when fitting data.

Formally,  $H_{mn}$  is written as:

$$H_{mn} = \frac{\partial^2 C}{\partial \theta_m \partial \theta_n} = \sum_i \frac{\partial r_i}{\partial \theta_m} \frac{\partial r_i}{\partial \theta_n} + r_i \frac{\partial^2 r_i}{\partial \theta_m \partial \theta_n}. \quad (\text{A.1})$$

If the model fits the data well so that  $r_i \approx 0$  (or perfectly, Ref. [32]) then

$$H_{mn}(\boldsymbol{\theta}^*) \approx \sum_i \frac{\partial r_i}{\partial \theta_m} \frac{\partial r_i}{\partial \theta_n} = (J^T J)_{mn}. \quad (\text{A.2})$$

If  $H$  and the cost are used (as in this review) to describe changes in model behavior from  $\boldsymbol{\theta}^*$ , then  $\mathbf{r} \equiv 0$  at  $\boldsymbol{\theta}^*$  and Equation (A.2) is exact. Notice also that  $H$  reflects the sensitivity of the fit to changes in parameters; in fact, its inverse is the covariance matrix. The diagonal elements of the covariance matrix are proportional to the uncertainties in the parameters, while the off-diagonal elements are estimates of parameter uncertainty correlations.

### A.2.2 Figure 2.1: Sloppiness in the mapping of chemotypes to dynatypes

Shown in Figure 2.1 is the mapping of chemotypes  $C$  to dynatypes  $D$ . The mapping between  $C$  and  $D$  is described with  $J$  and “ $J^{-1}$ ”. It is typical that  $\dim(C) \ll \dim(D)$ , since there are typically more data points constraining the dynatype than there are parameters defining a chemotype. Therefore, the inverse of  $J$  is not well-defined. In Figure 2.1, the gray ellipse in  $C$  represents the inverse image of the  $\epsilon$ -ball,  $B_\epsilon$ , in  $D$  under  $J$ . That is, “ $J^{-1}$ ” acting on  $B_\epsilon$  is the set  $\{\mathbf{c} \in C \text{ s.t. } J \cdot \mathbf{c} \in B_\epsilon\}$ .

Note also that the stiff and sloppy eigendirections in  $C$  and their images in  $D$  can be described by the singular value decomposition of the Jacobian  $J$ . Since  $\lambda_n$  are eigenvalues of  $J^T J$ ,  $\sqrt{\lambda_n}$  are the singular values of  $J$ . Furthermore, writing

$J = U \sum V^T$ , we see that the columns of  $V$  are stiff/sloppy eigenparameters in  $C$  (shown in red in the figure), and the columns of  $U$  are images of stiff and sloppy eigenparameters (divided by  $\lambda_n$ ) in  $D$ .

### A.3 Environmental robustness and sloppiness

#### A.3.1 Figure 2.2: Sloppy parameter distributions: dependence on external conditions

In Figure 2.2, the plane onto which the ensembles are projected is the one that aligns best with the stiffer eigenparameter of each of the four ensembles. To accomplish this, the vertical and horizontal axes in Figure 2.2 are, respectively, the first and second singular vectors in the singular value decomposition of the set of stiffer eigenparameters  $\{\mathbf{v}_0^{25}, \mathbf{v}_0^{30}, \mathbf{v}_0^{35}, \mathbf{v}_0^{All}\}$ . In a way analogous to principal components analysis, this gives the plane that passes through the origin and comes closest to passing through the heads of unit vectors pointing in the stiffer eigendirections.

Each ensemble of parameter sets shown in Figure 2.2 is chosen from the probability distribution corresponding to the local quadratic approximation of the cost near the best-fit parameters  $\boldsymbol{\theta}^*$ :

$$P(\boldsymbol{\theta}^* + \Delta\boldsymbol{\theta}) \propto \exp(-\Delta\boldsymbol{\theta} J^T J \Delta\boldsymbol{\theta}/2). \quad (\text{A.3})$$

This local approximation to the cost was used to generate the ensembles instead of the full nonlinear cost function due to difficulties in generating equilibrated ensembles: the thin curving manifolds of allowable chemotypes for sloppy models

can be notoriously difficult to populate. But this is not impossible; efforts are still underway, and if equilibrated ensembles are found, they will be posted to the website mentioned above.

### A.3.2 KaiC phosphorylation subnetwork model

In Chapter 2, we use as an example a portion of the circadian rhythm model presented in Ref. [75]. We implement the subnetwork that van Zon et al. hypothesize must have intrinsically temperature-independent rates: that which controls the phosphorylation of KaiC alone. This subnetwork models the experimental measurements of KaiC phosphorylation in the absence of KaiA and KaiB [72], in which the phosphorylation of KaiC does not oscillate, but decays at a temperature-compensated rate in the range from 25 to 35° C (see circles in Figure A.2).

The subnetwork involves an active and inactive state of KaiC, along with six phosphorylation sites for each state, as depicted in Figure A.1. Including forward and backward “flip” rates between active and inactive states along with (de)phosphorylation rates that are each constant for the two states, there are 18 independent rates. To assess the temperature dependence, we assume that each transition rate follows an Arrhenius law, with constant energy barrier  $E$  and prefactor  $\alpha$ : the  $i$ th rate is  $\alpha_i e^{E_i/kT}$ . This then gives a 36-dimensional chemotype space in which to search for solutions.

Temperature-independent solutions can be trivially found in this space if the energy barriers are chosen to be small, since this produces rates that are inherently weakly dependent on temperature. In order to avoid this trivial temperature compensation, we apply a prior that favors solutions with phosphorylation energy

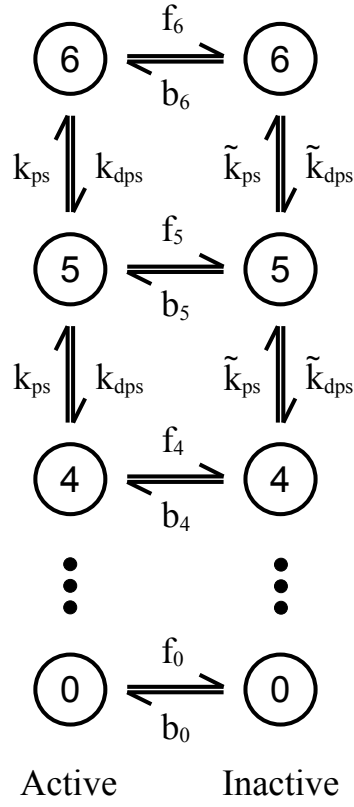


**Figure A.1: KaiC phosphorylation subnetwork.** This schematic depicts the KaiC network used as an example in the main text. It is a portion of the full circadian rhythm model presented in Ref. [75]. The numbers represent the degree of phosphorylation, and the two columns represent two different conformational states, “active” and “inactive.” The labels on the arrows represent reaction rates for changing among the phosphorylation and conformation states. Each conformation state has one phosphorylation and one dephosphorylation rate, independent of the degree of phosphorylation. Each of the 14 “flip” rates between conformational states ( $b_i$  and  $f_i$ ) is allowed to vary independently. This gives a total of 18 reaction rates.

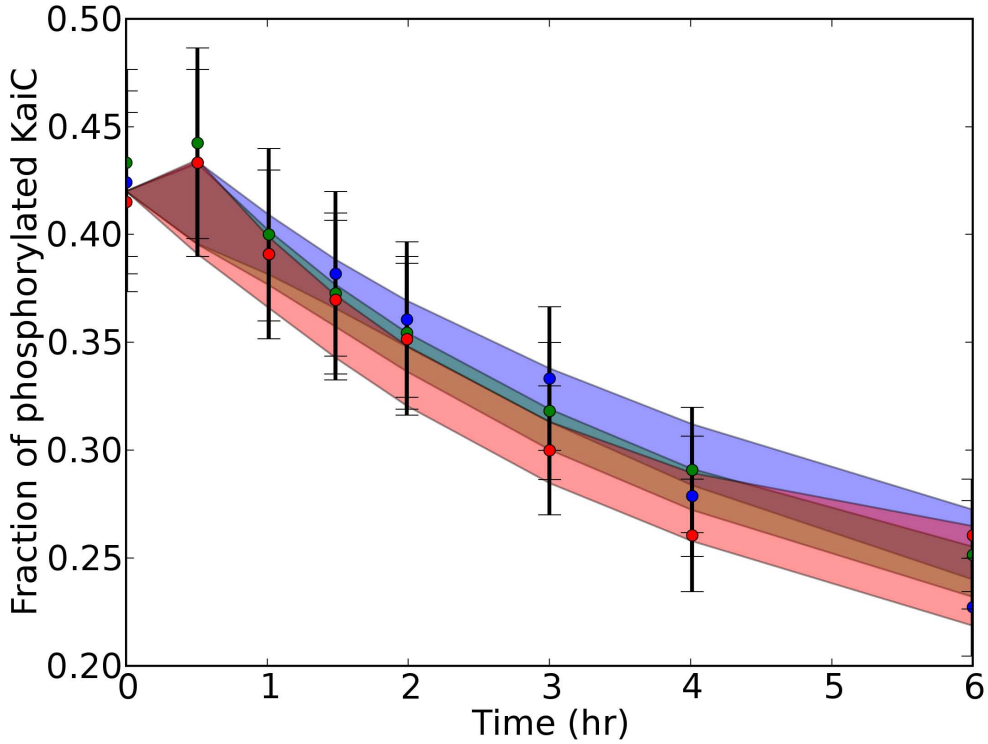


Figure A.2: **KaiC phosphorylation network: temperature-compensated output.** Shown is the net phosphorylation of KaiC over time, comparing experimental data (circles with error bars, from Ref. [72]) with output from an ensemble of chemotypes (filled colored regions, showing the mean plus or minus one standard deviation over the ensemble for the net phosphorylation at each time-point). Different colors correspond to different temperatures: blue = 25°, green = 30°, red = 35°. Note that the chemotypes describe the data well at all three temperatures, even though the rates are strongly dependent on temperature.

barriers near the expected  $E_0 = 23 \text{ } kT$ , similar to those found in other kinases [10] and appropriate for reactions that break covalent bonds. We choose this prior as a quartic in  $\log E$ :

$$C_{prior} = \frac{25}{2} \left[ \log \left( \frac{E}{E_0} \right) \right]^4. \quad (\text{A.4})$$

The form was chosen to severely penalize barriers less than 10  $kT$ , but to be reasonably flat around  $E_0$ ; other prior choices would presumably perform similarly.

Using this method, we find that it is possible to fit the experimental data even with (de)phosphorylation rates that are strongly temperature-dependent. The phosphorylation and dephosphorylation rates that provided a best fit to all temperatures simultaneously were all above  $21 \text{ } kT$ . We used Bayesian Monte-Carlo sampling of chemotype space to create an ensemble of parameter sets that each produce phosphorylation dynamics that match the experimental data at 25, 30, and 35° C. As explained above, our ensemble has not yet sampled all the space available, but we still find many such acceptable chemotypes. The minimum (de)phosphorylation rate for the ensemble was just under  $10 \text{ } kT$ , so the prior worked as designed to confine the barriers to physically reasonable values. Figure A.2 shows the output of the model over this ensemble of parameter sets compared with the experimental data from Ref. [72].

We mention in a footnote that, in our model, “successful chemotypes favor dephosphorylation in the active state and phosphorylation in the inactive state.” This can be seen in the ratio of phosphorylation to dephosphorylation rates, shown in Figure A.3, for the ensemble of successful chemotypes. Note that most members of the ensemble have an inactive state with higher phosphorylation rate than dephosphorylation, and vice versa for the active state. This matches with an intuitive temperature-compensation mechanism: with flip rates that are also temperature-dependent, higher temperatures can lead to more KaiC being in the inactive state, leading to a slower overall decay in phosphorylation that compensates for the speedup in reaction rates.

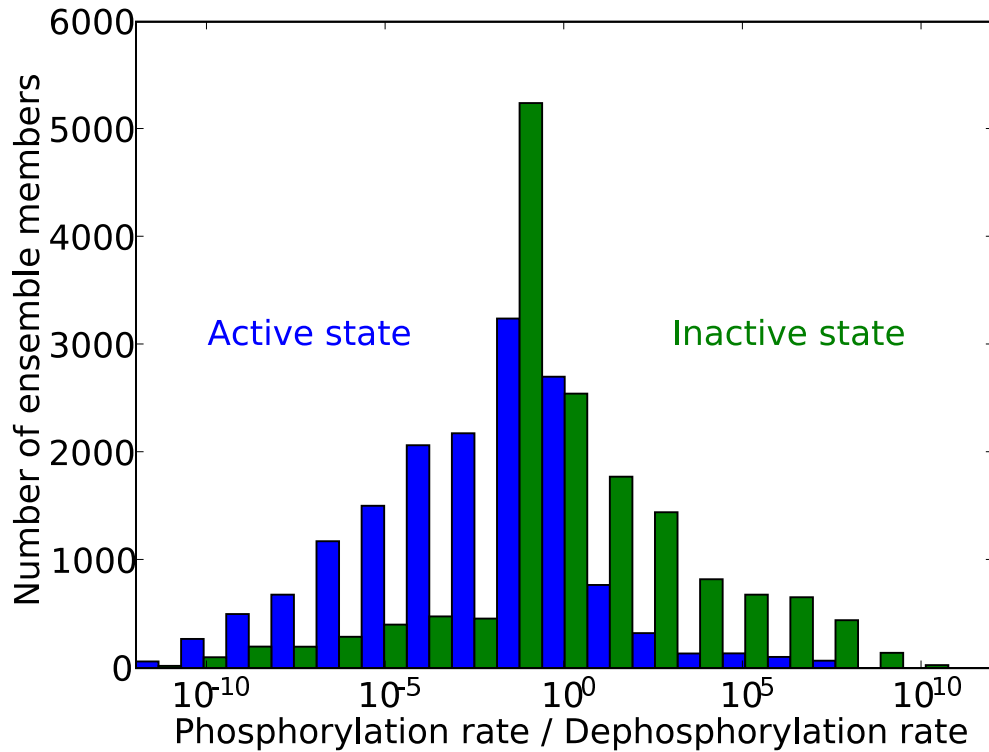


Figure A.3: **KaiC phosphorylation network: temperature-compensation mechanism.** This plot shows the ratios of phosphorylation rates to dephosphorylation rates for the active and inactive states – the distribution of  $k_{ps}/k_{dps}$  is shown in blue for the active state, and the distribution of  $\tilde{k}_{ps}/\tilde{k}_{dps}$  is shown in green for the inactive state (see Figure A.1 for definitions of rate constants). The distribution is over the same (non-equilibrated) ensemble as was used to generate Figure A.2. Note that phosphorylation is favored in the inactive state, while dephosphorylation is favored in the active state. This suggests a temperature-compensation mechanism, as described in the text.

### A.3.3 Figure 2.3: Sloppy model eigenvalues

The PCA shown in Figure 2.3 column *SP PCA* was produced after taking logarithms of the parameter values that von Dassow *et al.* used in their analysis. This measures parameter fluctuations in terms of fractional changes in parameter, rather than absolute sizes of fluctuations – allowing fluctuations in parameters with different units, for example, to be compared. The parameters used in column *SP* were chosen (logarithmic or otherwise) as defined by the original authors. Taking logarithms and/or changing units does not typically change the qualitative spectra of sloppy models, as their spectra already span so many decades.

## A.4 Chemotype robustness and sloppiness

### A.4.1 Derivation of robustness equation

In Chapter 2, the robustness is defined as

$$R_c = \prod_{\lambda_n > \lambda_{crit}} \sqrt{\frac{\lambda_{crit}}{\lambda_n}}. \quad (2.2)$$

We now proceed to derive this result. We measure robustness as the fraction of mutations of a given size  $\delta$  in  $C$  (chemotype space) that do not change the behavior beyond a given threshold (survival after a mutation), which we designate as an  $\epsilon$ -ball around the optimum in  $D$  (dynatype space). Therefore we want an estimate of the fraction of the  $\delta$ -ball in  $C$  that maps into the  $\epsilon$ -ball in  $D$ . It is difficult to calculate this geometrically, since we would need to find the volume of an ellipsoid intersecting a sphere. Fortunately, for sloppy systems, the  $\lambda_i$  vary over many orders of magnitude, so we can simplify the calculation by smearing

the  $\delta$ -ball and  $\epsilon$ -ball into Gaussians. Namely, we say a mutation  $\Delta\boldsymbol{\theta}$  in  $C$  has probability  $e^{-(\Delta\boldsymbol{\theta})^2/2\delta^2}/(\sqrt{2\pi}\delta)^N$ , and the probability of “survival” in  $D$  is given by  $e^{-r^2/2\epsilon^2}$ . We then measure the robustness as the overall probability  $P(\delta, \epsilon)$  of surviving after a mutation:

$$\begin{aligned} R_c &= P(\delta, \epsilon) \\ &= \left( \frac{1}{\sqrt{2\pi}\delta} \right)^N \int_C d\Delta\boldsymbol{\theta} \exp(-(\Delta\boldsymbol{\theta})^2/2\delta^2) \exp(-(\Delta\boldsymbol{\theta})^T J^T J(\Delta\boldsymbol{\theta})/2\epsilon^2) \\ &= \prod_n \frac{1}{\sqrt{1 + \lambda_n \delta^2/\epsilon^2}}. \end{aligned} \quad (\text{A.5})$$

For sloppy systems,  $\lambda$  varies over many orders of magnitude. Notice that if  $\lambda_n \ll \epsilon^2/\delta^2$ , its component in the product will be close to 1, and if  $\lambda_n \gg \epsilon^2/\delta^2$ , we can approximate the components in the product as  $\sqrt{\epsilon^2/\delta^2 \lambda_n}$ . Therefore, using our definition  $\lambda_{crit} \equiv \epsilon^2/\delta^2$  we can approximate this formula as:

$$R_c \approx \prod_{\lambda_n > \epsilon^2/\delta^2} \sqrt{\frac{\epsilon^2}{\delta^2 \lambda_n}} = \prod_{\lambda_n > \lambda_{crit}} \sqrt{\frac{\lambda_{crit}}{\lambda_n}}, \quad (\text{A.6})$$

with small corrections for eigenvalues  $\lambda_n \approx \epsilon^2/\delta^2$ . Since this result agrees with the “slab” argument given in Chapter 2 for hard walls, we see that hard  $\epsilon$ -balls and hard  $\delta$ -balls will have approximately the same amount of overlap as Gaussians.

## A.5 Robustness, evolvability, and sloppiness

### A.5.1 Derivation of chemotype evolvability

In Chapter 2, we provide a formula for the “maximum fitness change among mutations of size  $\delta$  in chemotype space”

$$e_c(\mathbf{F}, \boldsymbol{\theta}) = \sqrt{\mathbf{F}^T J J^T \mathbf{F}} \delta \quad (2.3)$$

which we derive here using a Lagrange multiplier. To derive this, we use the definition of the chemotype evolvability as the maximum response  $\mathbf{r} \cdot \mathbf{F}$  in  $R$  for moves in  $C$  of size  $|\Delta\boldsymbol{\theta}| = \delta$ :

$$e_c(\mathbf{F}, \boldsymbol{\theta}) = \max_{|\Delta\boldsymbol{\theta}|=\delta} (\mathbf{r} \cdot \mathbf{F}). \quad (\text{A.7})$$

Next, notice that

$$\mathbf{r} \cdot \mathbf{F} = (J\Delta\boldsymbol{\theta}) \cdot \mathbf{F} = \sum_i \sum_{\alpha} F_i J_{i\alpha} \Delta\theta_{\alpha}. \quad (\text{A.8})$$

We find the optimal  $\Delta\boldsymbol{\theta}$  using a Lagrange multiplier  $\Lambda$ . With  $(\Delta\boldsymbol{\theta})^2 = \delta^2$  as our constraint, we maximize

$$F_i J_{i\alpha} \Delta\theta_{\alpha} + \Lambda((\Delta\boldsymbol{\theta})^2 - \delta^2) = F_i J_{i\alpha} \Delta\theta_{\alpha} + \Lambda(\Delta\theta_{\beta} \Delta\theta_{\beta} - \delta^2) \quad (\text{A.9})$$

where we use the Einstein summation convention (summing over repeated indices). Differentiating with respect to  $\Delta\theta_{\alpha}$ , we can find the change  $\Delta\theta_{\alpha}^{max}$  giving the maximum response:

$$\Delta\theta_{\alpha}^{max} = \frac{F_j J_{j\alpha}}{2\Lambda} \quad (\text{A.10})$$

and hence

$$(\Delta\boldsymbol{\theta}^{max})^2 = \frac{F_i J_{i\alpha} J_{j\alpha} F_j}{4\Lambda^2} = \delta^2, \quad (\text{A.11})$$

which implies

$$\Lambda^2 = \frac{\mathbf{F}^T J J^T \mathbf{F}}{4\delta^2}. \quad (\text{A.12})$$

Therefore, the evolvability is:

$$\begin{aligned} e_c(\mathbf{F}, \boldsymbol{\theta}) &= F_i J_{i\alpha} \Delta\theta_{\alpha}^{max} = \frac{F_i J_{i\alpha} F_j J_{j\alpha}}{2\Lambda} \\ &= \frac{\mathbf{F}^T J J^T \mathbf{F}}{\sqrt{\mathbf{F}^T J J^T \mathbf{F}}} \delta = \sqrt{\mathbf{F}^T J J^T \mathbf{F}} \delta. \end{aligned} \quad (\text{A.13})$$

### A.5.2 RMS dynatype evolvability

In Equation (2.5), to measure overall evolvability, we defined  $E_c(\boldsymbol{\theta}_\alpha)$  as a root-mean-square (RMS) average over a uniform (hyper)spherical distribution of environmental forces  $\mathbf{F}$  in dynatype space. We use the RMS  $\sqrt{\langle e_c(\mathbf{F}, \boldsymbol{\theta}_\alpha)^2 \rangle}$  rather than the average  $\langle e_c(\mathbf{F}, \boldsymbol{\theta}_\alpha) \rangle$  because the RMS definition has an elegant result in terms of the eigenvalues  $\lambda_i$  of  $J^T J$ :

$$\begin{aligned}
E_c(\boldsymbol{\theta}_\alpha)^2 &= \langle e_c(\mathbf{F}, \boldsymbol{\theta}_\alpha)^2 \rangle_{\mathbf{F}} = \langle \mathbf{F}^T J J^T \mathbf{F} \delta^2 \rangle_{\mathbf{F}} \\
&= \sum_i \frac{\int \lambda_i F_i^2 d^N \mathbf{F}}{\int d^N \mathbf{F}} \delta^2 \\
&= \sum_i \lambda_i \langle F_i^2 \rangle \delta^2 = \frac{\sum_i \lambda_i \langle \mathbf{F}^2 \rangle}{N} \delta^2 \\
&= \frac{\text{Tr}(J^T J) \langle \mathbf{F}^2 \rangle}{N} \delta^2 \approx \frac{\text{Tr}(H) \langle \mathbf{F}^2 \rangle}{N} \delta^2.
\end{aligned} \tag{A.14}$$

Therefore, the overall evolvability is directly related to the trace of the Hessian:

$$E_c(\boldsymbol{\theta}_\alpha) = \sqrt{\frac{\text{Tr}(H) \langle \mathbf{F}^2 \rangle}{N}} \delta. \tag{A.15}$$

Our measures of robustness and evolvability depend upon our level of description, just as for Wagner’s genotype and phenotype evolvabilities of RNA sequences [80]. Our choice of an isotropic distribution of selective dynatype forces  $\mathbf{F}$  is not intended as an accurate representation of actual selective forces at the phenotype level, but as an exhaustive study of all possible forces at the dynatype level of description.

Information about phenotypic selective pressures might suggest a different distribution of dynatype forces  $\mathbf{F}$ . Indeed, this formalism provides a mechanism for coupling maps across scales, which is an important unsolved problem. Just as the genotype-to-chemotype ( $G \rightarrow C$ ) and chemotype-to-dynatype ( $C \rightarrow D$ ) maps are

many-to-one, so is the dynatype-to-phenotype map ( $D \rightarrow P$ ). In the segment polarity model, for example, one might construe the phenotype as the steady-state pattern, whereas the dynatype will include information about all transient paths to that steady state. This is also closely analogous to measuring evolvability of RNA sequences by counting distinct folded structures [80], as many different structures may be equally nonfunctional at the higher level of biological phenotype. Ultimately, understanding the nature of the complex  $D \rightarrow P$  maps will be required to estimate evolvability using more realistic distributions of selective dynatypic forces **F**.

### A.5.3 Figure 2.4: Evolvability and robustness in a sloppy system

When calculating the chemotype robustness  $R_c$ , we have a choice to make for the value of  $\lambda_{crit}$  (see Equation 2.2). This choice corresponds to setting the ratio of the size of acceptable changes in dynatype  $\epsilon$  to the typical size of mutations  $\delta$  in chemotype space:  $\lambda_{crit} = \epsilon^2/\delta^2$ . Equivalently,  $\lambda_{crit}$  sets a cutoff between stiff and sloppy eigenvalues, since we assume that, in  $D$  space, the image of the  $\delta$ -ball fully overlaps with the  $\epsilon$ -ball in sloppy directions (with eigenvalues below  $\lambda_{crit}$ ), and it extends far beyond the edge of the  $\epsilon$ -ball in stiff directions (with eigenvalues above  $\lambda_{crit}$ ).

In calculating  $R_c$  for the inset of Figure 2.4, we chose  $\lambda_{crit}$  as the fourth stiffest eigenvalue of  $J^T J$  at the best fit parameters. This matches with the idea that there are only a few stiff directions that appreciably constrain parameters in chemotype space: the eigenvalues are spaced by roughly factors of three (Figure 2.3), meaning

mutations in sloppier directions in chemotype space quickly become irrelevant in dynatype space. The choice of  $\lambda_{crit}$  within a reasonable range (between, say, the second stiffest and eighth stiffest eigenvalue of  $J^T J$ ) does not qualitatively change the plot of evolvability vs. robustness.

APPENDIX B  
SUPPLEMENTARY MATERIAL FOR CHAPTER 3

### B.1 Behavior of extended DNA with fluctuations

The behavior of extended DNA is appreciably affected by thermal fluctuations. For the applied forces in the range considered in this experiment, we can use the following fixed-torque free energy:

$$\frac{\mathcal{G}(\tau)}{L} = -F - \frac{\tau^2}{2C_{bare}} + \frac{kT}{B} \sqrt{BF - \frac{\tau^2}{4}}, \quad (\text{B.1})$$

where the last term is the lowest-order correction due to fluctuations [53].

The fluctuations decrease the extension:

$$-\frac{\partial \mathcal{G}}{\partial F} = L \left[ 1 - \frac{kT}{2} \left( BF - \frac{\tau^2}{4} \right)^{-1/2} \right]. \quad (\text{B.2})$$

(The  $-1/32$  in Eq. (1) comes from an approximation to a higher-order correction [53].)

Expanding the last term of Eq. (B.1) to match the form of a “zero-temperature” chain, we can instead write

$$\frac{\mathcal{G}(\tau)}{L} = -F_{\text{eff}} - \frac{\tau^2}{2C_{\text{eff}}}, \quad (\text{B.3})$$

where the effective force and twist elastic constant are given by

$$F_{\text{eff}} = F - kT \sqrt{\frac{F}{B}} \quad (\text{B.4})$$

$$C_{\text{eff}} = C_{\text{bare}} \left( 1 + kT \frac{C_{\text{bare}}}{4B\sqrt{BF}} \right)^{-1}. \quad (\text{B.5})$$

Note that  $C_{\text{eff}}$  is a function of force: there is less “softening” at higher forces. In the experiments of Forth *et al.*, the renormalized  $C_{\text{eff}}$  was measured directly via

the torque. However, the range of applied forces was small enough that  $C_{\text{eff}}$  did not change appreciably, and a single value of  $C = (89 \text{ nm})kT$  was quoted. Here, we also use the same renormalized but force-independent value for  $C$ .

Changing Eq. (B.3) to a fixed-linking-number expression via a Legendre transformation, we arrive at our expression for the straight state free energy (also found in Ref. [49]):

$$\mathcal{F}_s(K, L) = \frac{C}{2} \left( 2\pi \frac{K}{L} \right)^2 L - F_{\text{eff}} L. \quad (\text{B.6})$$

## B.2 Derivation of linear expressions for $\mathcal{F}_{\text{CS}}$ and $z_{\text{CS}}$

We first write down the linear scaling of the free energy and extension with linking number. For any  $\delta K$  that does not take the system out of the CS,

$$\mathcal{F}_{\text{CS}}(K + \delta K, L) = \mathcal{F}_{\text{CS}}(K, L) + 2\pi\tau\delta K; \quad (\text{B.7})$$

$$z_{\text{CS}}(K + \delta K, L) = z_{\text{CS}}(K, L) - q\delta K, \quad (\text{B.8})$$

where  $q$  is the slope of extension versus linking number and  $\tau$  is the CS torque. Next, to find the scaling with increasing  $L$ , we imagine adding a piece of stretched DNA of length  $\delta L$  at the coexisting torque (keeping the system in a stable CS). This also adds an amount of linking number that scales with  $\delta L$ ,  $\delta K[\delta L] = \tau\delta L/(2\pi C)$ , which we will have to unwind to get back to the original  $K$ . First adding the piece of stretched DNA, and then unwinding to find the dependence on  $L$  only, we find

$$\mathcal{F}_{\text{CS}}(K, L + \delta L) = \mathcal{F}_{\text{CS}}(K, L) - \left( \frac{\tau^2}{2C} + F_{\text{eff}} \right) \delta L. \quad (\text{B.9})$$

Similarly for the extension, [using  $\xi(\tau)$  from Eq. (1)]

$$z_{\text{CS}}(K, L + \delta L) = z_{\text{CS}}(K, L) + \left( \xi(\tau) + \frac{\tau}{2\pi C} q \right) \delta L. \quad (\text{B.10})$$

Combining Eqs. (B.7) and (B.8) with Eqs. (B.9) and (B.10), we can write the free energy and extension of the CS as linear in  $K$  and  $L$ , each with a slope and an intercept:

$$\mathcal{F}_{\text{CS}}(K, L) = \mathcal{F}_0 + 2\pi\tau K - \left( \frac{\tau^2}{2C} + F_{\text{eff}} \right) L; \quad (\text{B.11})$$

$$z_{\text{CS}}(K, L) = -z_0 - qK + \left( \xi(\tau) + \frac{\tau}{2\pi C} q \right) L. \quad (\text{B.12})$$

Note that  $C$  and  $\xi(\tau)$  are known from experiments on stretched DNA, leaving the four anticipated force-dependent quantities to be described by a theory of supercoiling:  $\tau$ ,  $q$ ,  $\mathcal{F}_0$ , and  $z_0$ .

### B.3 Self-repulsion

It is essential to include a repulsive force between sections of the DNA that come near each other; without it, the rod can pass through itself, unphysically removing linking number in the process and preventing the formation of plectonemes. The physical origins of repulsive forces in DNA include both electrostatic and entropic effects. We use discretized versions of the repulsive interactions described in Ref. [48].

Electrostatic forces are modeled using a Debye-Huckel screened Coulomb interaction:

$$E_{\text{SC}}(r) = \frac{|e_- \nu d|^2}{\epsilon} \frac{e^{-r/\lambda_D}}{r}, \quad (\text{B.13})$$

where  $\nu = 8.4 \text{ nm}^{-1}$  is the effective number of electron charges per unit length,  $\lambda_D = 0.8 \text{ nm}$  is the Debye screening length, and  $e_-^2/\epsilon = 2.9 \text{ pN nm}^2$ . (These values are dependent on the ionic concentration of the buffer, and were picked to match with  $\approx 150 \text{ mM NaCl}$ .)

The entropic free energy of a helical structure is calculated in Ref. [48], coming from the increasing confinement of fluctuations in more tightly coiled structures. We use the same free energy, written as a pairwise interaction between segments:

$$E_{\text{ent}}(r) = \frac{2^{5/3}\sqrt{\pi}\Gamma(1/3)}{\Gamma(5/6)} \frac{kTd^2}{(B/kT)^{1/3}r^{5/3}}. \quad (\text{B.14})$$

Since we also include straight parts of the DNA that should not have the same entropic interaction, we cut off the entropic potential at a distance of  $2B/kT$ , where the argument for the form of the potential breaks down [48].

## B.4 Extra terms in the circular end-loop model

Extra terms in the free energy that we have not considered would change the predictions of the circular end-loop model — these could include electrostatic interactions, entropic effects, etc. In fact, we can solve for the properties that such an extra free energy term (call it  $\mathcal{F}_{\text{extra}}$ ) would need to have in order to make the model match the experimental data.

Adding this unknown term, we have

$$\mathcal{F}_l(K_l, L_l) = \frac{C}{2L_l} [2\pi(K_l - \text{Wr}_{\text{loop}})]^2 + (2\pi)^2 \frac{B}{2L_l} + \mathcal{F}_{\text{extra}}(K_l, L_l). \quad (\text{B.15})$$

Since the terms we will imagine adding will not depend on  $K_l$ , we will assume that  $\mathcal{F}_{\text{extra}}$  is only a function of  $L_l$ . Setting the force and torque equal to the coexisting state values ( $d\mathcal{F}_l/dL_l = -(F_{\text{eff}} + \tau^2/(2C))$ ;  $d\mathcal{F}_l/dK_l = 2\pi\tau$ ) then gives

$$L_l^* = 2\pi \sqrt{\frac{B}{2(F_{\text{eff}} + d\mathcal{F}_{\text{extra}}/dL_l)}} \quad (\text{B.16})$$

$$K_l^* = \frac{\tau L_l^*}{2\pi C} + \text{Wr}_{\text{loop}}. \quad (\text{B.17})$$

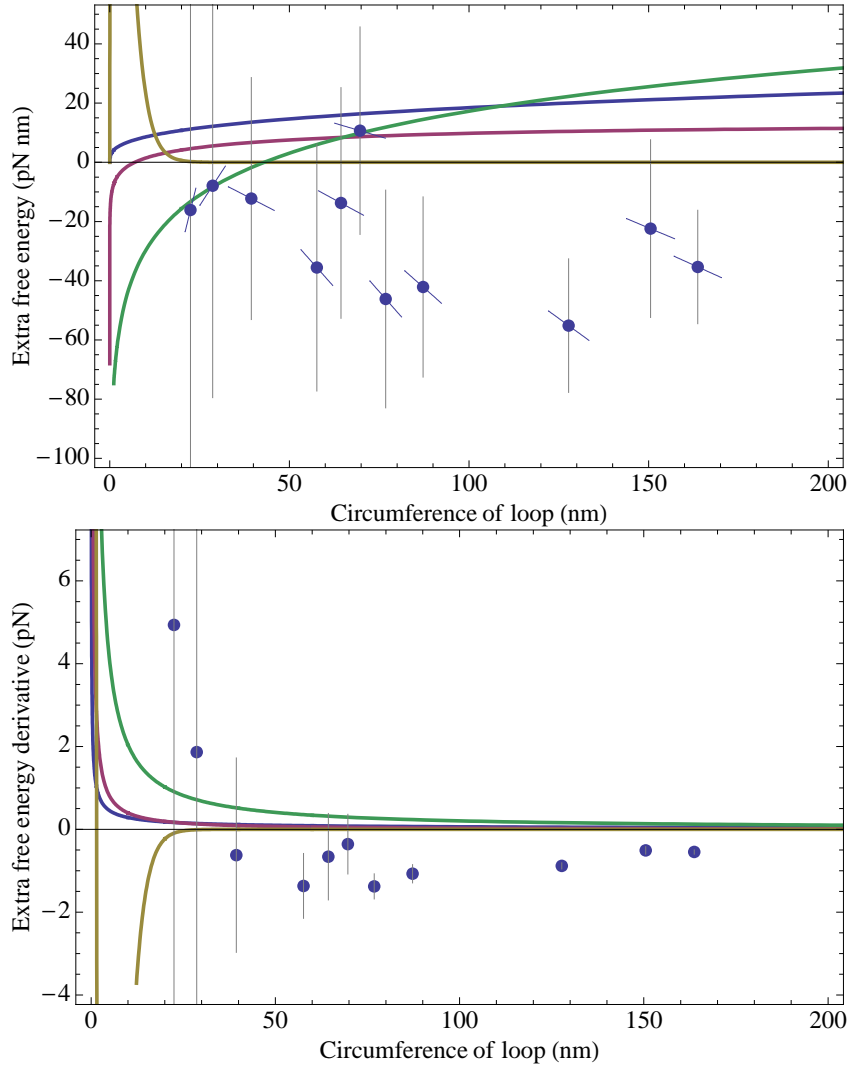


**Figure B.1: Testing entropic corrections.** Entropic corrections from the literature do not help the circular end-loop model fit the data. The dots show the required free energy contribution  $\mathcal{F}_{\text{extra}}$  (top plot) and its derivative with respect to end-loop circumference  $d\mathcal{F}_{\text{extra}}/dL_l$  (bottom plot) that would produce an  $\mathcal{F}_0$  and  $z_0$  that match with the experiment (with  $W_{\text{loop}} = 0.8$ ). Bars on the top plot show the required derivative, the value of which is shown on the bottom plot. Vertical grey lines show one standard deviation error bars. Note especially the inability of any of the proposed entropic terms to match the well-constrained negative derivative at large end-loop circumferences (which happen at low force in the experiment); this produces  $L_l$  (and thus  $z_0$ ) that are too small at low forces. A lessening of the effective force felt by the end-loop of about 0.5 pN would help agreement, but none of the proposed corrections provides this.

We now use the fact that

$$\mathcal{F}_0 = \mathcal{F}_l^* + \left( F_{\text{eff}} + \frac{\tau^2}{2C} \right) L_l^* - 2\pi\tau K_l^* \quad (\text{B.18})$$

$$z_0 = \xi(\tau)L_l^* - q \left( K_l^* - \frac{\tau L_l^*}{2\pi C} \right) \quad (\text{B.19})$$

to solve for the necessary values of  $\mathcal{F}_{\text{extra}}$  and  $d\mathcal{F}_{\text{extra}}/dL_l$  in order to match with the experimental  $\mathcal{F}_0$  and  $z_0$ . We find

$$\mathcal{F}_{\text{extra}} = \mathcal{F}_0 + 2\pi\tau W_{\text{loop}} - F_{\text{eff}} L_l^* - \frac{2\pi^2 B}{L_l^*} \quad (\text{B.20})$$

$$\frac{d\mathcal{F}_{\text{extra}}}{dL_l} = \frac{2\pi^2 B}{L_l^{*2}} - F_{\text{eff}}, \quad (\text{B.21})$$

where

$$L_l^* = \frac{z_0 + qW_{\text{loop}}}{\xi(\tau)}. \quad (\text{B.22})$$

These required properties of the added free energy term are plotted in Figure B.1 for  $W_{\text{loop}} = 0.8$ .

We can then test whether different possible extra free energy terms would match the requirements. Here we try four possibilities taken from the literature. First, there is electrostatic repulsion coming from like charges on opposite sides of the DNA circle. This looks like (using the Debye-Hückel formulation from Ref. [48])

$$\mathcal{F}_{\text{extra}}^{\text{electrostatic}} = kT l_B \nu^2 K_0 \left( \frac{L_l}{\pi \lambda_D} \right) L_l \quad (\text{B.23})$$

and is plotted in yellow in Figure B.1. Second, Odijk calculates the free energy for a circular DNA loop and finds terms in the free energy [60] [Eq. (2.13)]

$$\mathcal{F}_{\text{extra}}^{\text{Odijk}} = kT \log \frac{2\pi L}{B/(kT)} - \frac{(kT)^2}{8B} L; \quad (\text{B.24})$$

this is plotted in purple in Figure B.1. Third, a similar term is found by Tkachenko in solving for the J-factor for unconstrained DNA cyclization [71] [Eq. (4)]:

$$\mathcal{F}_{\text{extra}}^{\text{Tkachenko}} = 5kT \log \frac{L}{B/(kT)}; \quad (\text{B.25})$$

this is plotted in green in Figure B.1. Finally, we could imagine that entropic contributions from confinement similar to the one used by us for our elastic simulation could be important. Although the form was derived for a different configuration (superhelical DNA), we could try it to see if something similar might help. Integrating the confinement entropy from Marko and Siggia [48] over a circle gives

$$\mathcal{F}_{\text{extra}}^{\text{confinement}} = \frac{kT}{(B/kT)^{1/3}(L/(2\pi))^{2/3}} L, \quad (\text{B.26})$$

which is plotted in blue in Figure B.1.

Although these possible terms are only initial guesses at the possible corrections due to entropic and other effects, we see that they are all qualitatively unable to help, especially at long loop lengths, which is where the circular loop model fares worst at fitting the data.

## B.5 Calculating entropic contributions from fluctuations in plectoneme location, length, and linking number

To investigate entropic effects, we would like to find the free energy of states with multiple plectonemes,<sup>1</sup> including fluctuations of linking number and length both within individual plectonemes and moving among different plectonemes. We can achieve this by calculating the partition function for a state with  $n$  plectonemes, identifying unique states by the plectoneme positions  $s_i$ , the plectoneme lengths

---

<sup>1</sup> If the free energy necessary to nucleate a plectoneme is large compared to  $kT$ , then the coexisting state will contain a single plectoneme. If this is not the case, however (for example, when  $L$  becomes large), we will need to consider equilibrium states in which multiple plectonemes coexist.

$L_{pi}$ , and the plectoneme linking numbers  $K_{pi}$ :

$$\begin{aligned} Z_n(K, L) = & \frac{1}{L_0^n} \int_0^L ds_1 \int_{s_1}^L ds_2 \dots \int_{s_{n-1}}^L ds_n \\ & \frac{1}{L_0^n} \int_0^L dL_{p1} \int_0^L dL_{p2} \dots \int_0^L dL_{pn} \\ & \frac{1}{K_0^n} \int_{-\infty}^{\infty} dK_{p1} \int_{-\infty}^{\infty} dK_{p2} \dots \int_{-\infty}^{\infty} dL_{Kn} \\ & \exp [-\mathcal{F}_n(L, K, L_{pi}, K_{pi})/kT], \end{aligned} \quad (\text{B.27})$$

where we have neglected the complications coming from the possibility that plectonemes could overlap. The constants  $L_0$  and  $K_0$  set the length change and linking number change, respectively, that produce an independent state. Since we are only concerned with the free energy difference between the straight state and coexisting state, these constants would be set by the change in entropy of the degrees of freedom in the straight state that are lost to the collective modes we are integrating over in the coexisting state.

The first line of integrals represents the choice of where to put each plectoneme, which does not change the free energy ( $\mathcal{F}_n$  does not depend on  $s_i$ ). We therefore simply get a factor of  $L^n$ , divided by  $n!$  since plectonemes are indistinguishable:

$$\begin{aligned} Z_n(K, L) = & \frac{(L/L_0)^n}{n!} \frac{1}{L_0^n K_0^n} \int_0^L \prod_i dL_{pi} \\ & \int_{-\infty}^{\infty} \prod_i dK_{pi} \exp [-\mathcal{F}_n(L, K, \{L_{pi}\}, \{K_{pi}\})/kT]. \end{aligned} \quad (\text{B.28})$$

Next we need to know the free energy of coexisting states that are away from the equilibrium plectoneme length and linking number. Assuming that the plectoneme free energy density is quadratic in linking number density (as in Marko's model

[49]), this turns out to be

$$\begin{aligned}\mathcal{F}_n(L, K, \{L_{pi}\}, \{K_{pi}\}) &= \sum_{i=1}^n \frac{C}{2} \left( \frac{1}{1+v} \right) \left( 2\pi \frac{K_{pi}}{L_{pi}} \right)^2 L_{pi} \\ &\quad + \frac{C}{2} \left( 2\pi \frac{K - \sum K_{pi}}{L - \sum L_{pi}} \right)^2 (L - \sum L_{pi}) \\ &\quad - F_{\text{eff}}(L - \sum L_{pi}) + n\mu,\end{aligned}\quad (\text{B.29})$$

where  $\mu$  is the chemical potential for plectoneme ends and  $v \equiv 2CF_{\text{eff}}/\tau^2$ .

We first evaluate the integrals over  $K_{pi}$ , which amount to  $n$  Gaussian integrals; this gives

$$\begin{aligned}Z_n(K, L) &= \frac{(L/L_0)^n}{n!} \frac{1}{L_0^n K_0^n} \pi^{n/2} \int_0^L \prod_i dL_{pi} \left( \frac{\prod_i L_{pi}/c_1}{1 + (1+v) \frac{\sum L_{pi}}{L - \sum L_{pi}}} \right)^{1/2} \\ &\quad \exp \left( -\frac{1}{kT} \left[ \frac{\frac{C}{2}(2\pi K)^2}{L - \sum L_{pi} + (1+v)(\sum L_{pi})} - F_{\text{eff}}(L - \sum L_{pi}) + n\mu \right] \right).\end{aligned}\quad (\text{B.30})$$

Now changing to unitless variables  $x_i = L_{pi}/L_p$  and  $y = L_p/L$ , and rearranging to move all the factors that depend on the sum of the plectoneme lengths  $y$  into the exponent, the term in the exponent becomes

$$f(y) = \frac{1}{kT} \left( \frac{\frac{C}{2}(2\pi K)^2/L}{1+vy} - F_{\text{eff}}L(1-y) + n\mu \right) + \frac{1}{2} \log \left( \frac{1+vy}{1-y} \right), \quad (\text{B.31})$$

and we have (with  $\chi = \frac{(L/L_0)^n}{n!} \frac{1}{L_0^n K_0^n} \pi^{n/2}$ ),

$$\begin{aligned}Z_n(K, L) &= \chi \int_0^L \prod_i dx_i \sqrt{\prod_i L_{pi}/c_1} \exp [-f(\sum L_{pi}/L)] \\ &= \chi \int_0^L dL_p \delta \left( \sum L_{pi} - L_p \right) \int_0^{L_p} \prod_i dL_{pi} \sqrt{\prod_i L_{pi}/c_1} \exp [-f(L_p/L)] \\ &= \chi \int_0^L dL_p \frac{L_p^n}{L_p} \left( \frac{L_p}{c_1} \right)^{\frac{n}{2}} \left[ \int_0^1 \prod_i dx_i \sqrt{\prod_i x_i} \delta(\sum x_i - 1) \right] \exp [-f(L_p/L)] \\ &= \frac{(L/L_0)^{2n} (L/c_1)^{n/2}}{K_0^n} \frac{\pi^{n/2} \gamma_n}{n!} \int_0^1 dy \exp [-(f(y) - \frac{3n-2}{2} \log y)].\end{aligned}\quad (\text{B.32})$$

The integral in large square brackets (characterizing fluctuations in the individual plectoneme lengths that do not change the total plectoneme length) gives a numerical constant  $\gamma_n = \pi^{n/2}/(2^n \Gamma(3n/2)) = 2^{\lfloor \frac{n-1}{2} \rfloor} \pi^{\lfloor \frac{n}{2} \rfloor}/(3n - 2)!!$ . To evaluate the  $y$  integral over total plectoneme length, we make a Gaussian approximation [noting that the total length is well-constrained by  $f(y)$ ]. Then the fluctuations in the (fractional) total length of plectonemic DNA are of size

$$\sigma_y = \left( \frac{d^2}{dy^2} \left[ f(y) - \frac{3n-2}{2} \log y \right] \Big|_{y^*} \right)^{-1/2}, \quad (\text{B.33})$$

where  $y^*$  is the equilibrium value of  $y$ , and the derivative is

$$\frac{d^2}{dy^2} \left[ f(y) - \frac{3n-2}{2} \log y \right] = \frac{1}{2} \left( \frac{1}{(1-y)^2} + \frac{3n-2}{y^2} - \frac{v^2 \left( 1 - \frac{8\pi^2 CK^2}{LkT(1+vy)} \right)}{(1+vy)^2} \right). \quad (\text{B.34})$$

Without the entropic corrections, the equilibrium length is  $y^* = (u-1)/v$ , where  $u = 2\pi CK/(\tau L)$ . We can safely use this value if we are far from  $y^* = 0$  and  $y^* = 1$ , and get

$$\sigma_y = \frac{\sqrt{2}}{v} \left( \frac{1}{u} \frac{2\tau^2 L}{kTC} - \frac{1}{u^2} + \frac{1}{(v-u+1)^2} + \frac{3n-2}{(u-1)^2} \right)^{-1/2}. \quad (\text{B.35})$$

[Since we are usually near  $y^* = 0$  at the transition, to calculate the length-dependence shown in Fig. 4 (left), we approximate  $y^*$  numerically and use Eq. (B.33) instead of Eq. (B.35).] In the end, we have

$$Z_n(K, L) = \frac{(L/L_0)^{2n} (L/c_1)^{n/2}}{K_0^n} \frac{\pi^{n/2} \gamma_n}{n!} \sqrt{2\pi} \sigma_y \times \left( \frac{u-1}{v} \right)^{(3n-2)/2} \left( \frac{v-u+1}{uv} \right)^{1/2} \exp[-\mathcal{F}(K, L)/kT]. \quad (\text{B.36})$$

The full partition function for all plectonemic states is then

$$Z(K, L) = \sum_{n=1}^{\infty} Z_n(K, L) \quad (\text{B.37})$$

(which we can numerically approximate by truncating the series at a reasonable  $n$ ), such that the coexisting state free energy is given by  $\mathcal{F}_{\text{CS}}(K, L) = -kT \log Z(K, L)$ . For the experimental values, we find that only the single plectoneme  $n = 1$  state contributes significantly near the transition.

## B.6 Independence of results on entropic effects

In the paper, we have set the entropy from the previous section to zero ( $S = 0$ ) for most of the calculations. How would we expect that including  $S$  would change any of the results?

First,  $S$  would create a shift between the experimental  $\mathcal{F}_0$  and the predictions from models that do not include fluctuations. We find that this shift is largely independent of force, and is mostly dependent on  $L_0$ . We do not currently have a way of calculating  $L_0$ , but we expect that it should be on the order of the persistence length of DNA, about 50 nm. We find that setting  $L_0$  to about 100 nm makes the prefactor equal to 1, or equivalently sets  $S = 0$ . If we assume that  $L_0$  is about equal to the persistence length of DNA, we expect that we would need to shift the model predictions by at most about  $kT \log 2 \approx 5$  pN nm.

Second, we find that  $S$  has a logarithmic dependence on  $L$ . This means that we expect  $\mathcal{F}_0$  to decrease by something on the order of  $kT \log(L_2/L_1)$  when we increase the length from  $L_1$  to  $L_2$ . For the experimental lengths (with  $L_2 \approx 2L_1$ ), this again corresponds to a shift of about 5 pN nm.

Shifting  $\mathcal{F}_0$  by these amounts would slightly change only the theory curves for  $\mathcal{F}_0$  (about 5 pN nm),  $\Delta z$  (about 10 nm), and  $\Delta\tau$  (about 1 pN nm).

## REFERENCES

- [1] U. Alon, M. G. Surette, N. Barkai, and S. Leibler. Robustness in bacterial chemotaxis. *Nature*, 397(6715):168–171, 1999.
- [2] A. Balaeff, C. R. Koudella, L. Mahadevan, and K. Schulten. Modelling dna loops using continuum and statistical mechanics. *Phil. Trans. R. Soc. Lond. A*, 362:1355, 2004.
- [3] N. Barkai and S. Leibler. Robustness in simple biochemical networks. *Nature*, 387(6636):913–917, 1997.
- [4] Jan Bednar, Patrick Furrer, Vsevolod Katritch, Alicja Z. Stasiak, Jacques Dubochet, and Andrzej Stasiak. Determination of dna persistence length by cryo-electron microscopy. separation of the static and dynamic contributions to the apparent persistence length of dna. *J. Mol. Biol.*, 254:579, 1995.
- [5] Aviv Bergman and Mark L. Siegal. Evolutionary capacitance as a general feature of complex gene networks. *Nature*, 424(6948):549–552, 2003.
- [6] K S Brown, C C Hill, G A Calero, C R Myers, K H Lee, J P Sethna, and R A Cerione. The statistical mechanics of complex signaling networks: nerve growth factor signaling. *Phys Biol*, 1(3):184, 2004.
- [7] Kevin S. Brown and James P. Sethna. Statistical mechanical approaches to models with many poorly known parameters. *Phys. Rev. E*, 68:021904, August 12 2003.
- [8] Hergen Brutzer, Nicholas Luzzietti, Daniel Klaue, and Ralf Seidel. Energetics at the dna supercoiling transition. *Biophys. J.*, 98:1267, 2010.
- [9] Madalena Chaves, Eduardo D. Sontag, and Anirvan M. Sengupta. Shape, size and robustness: feasible regions in the parameter space of biochemical networks. arXiv.org:0710.4269, 2007.
- [10] Yuhui Cheng, Yingkai Zhang, and J. Andrew McCammon. How does activation loop phosphorylation modulate catalytic activity in the cAMP-dependent protein kinase: A theoretical study. *Protein Sci*, 15(4):672–683, 2006.
- [11] S. Ciliberti, O. C. Martin, and A. Wagner. Innovation and robustness in complex regulatory gene networks. *Proc Natl Acad Sci U S A*, 104(34):13591–13596, 2007.

- [12] Stefano Ciliberti, Olivier C Martin, and Andreas Wagner. Robustness can evolve gradually in complex regulatory gene networks with varying topology. *PLoS Comput Biol*, 3(2):e15, 2007.
- [13] N. Clauvelin, B. Audoly, and S. Neukirch. Mechanical response of plectonemic dna: An analytical solution. *Macromolecules*, 41:4479–4483, 2008.
- [14] R. G. Cox. The motion of long slender bodies in a viscous fluid : Part 1. general theory. *J. Fluid Mech.*, 44:791, 1970.
- [15] Aurélien Crut, Daniel A. Koster, Ralf Seidel, Chris H. Wiggins, and Nynke H. Dekker. Fast dynamics of supercoiled dna revealed by single-molecule experiments. *Proc. Natl. Acad. Sci. USA*, 104(29):11957, 2007.
- [16] Bryan C Daniels, Yan-Jiun Chen, James P Sethna, Ryan N Gutenkunst, and Christopher R Myers. Sloppiness, robustness, and evolvability in systems biology. *Curr Opin Biotech*, 19:389, 2008.
- [17] Bryan C. Daniels, Scott Forth, Maxim Y. Sheinin, Michelle D. Wang, and James P. Sethna. Discontinuities at the dna supercoiling transition. *Phys. Rev. E*, 80:040901(R), 2009.
- [18] J. Arjan G. M. de Visser, Joachim Hermisson, Günter P. Wagner, Lauren Ancel Meyers, Homayoun Bagheri-Chaichian, Jeffrey L. Blanchard, Lin Chao, James M. Cheverud, Santiago F. Elena, Walter Fontana, Greg Gibson, Thomas F. Hansen, David Krakauer, Richard C. Lewontin, Charles Ofria, Sean H. Rice, George von Dassow, Andreas Wagner, and Michael C. Whitlock. Perspective: Evolution and detection of genetic robustness. *Evolution*, 57(9):1959–1972, 2003.
- [19] John Doyle and Marie Csete. Motifs, control, and stability. *PLoS Biol*, 3(11):e392, 2005.
- [20] P. S. Doyle and P. T. Underhill. Brownian dynamics simulations of polymers and soft matter. In S. Yip, editor, *Handbook of Materials Modeling*, page 2619. Springer, 2005.
- [21] Quan Du, Alexander Kotlyar, and Alexander Vologodskii. Kinking the double helix by bending deformation. *Nucleic Acids Res.*, 36(4):1120–1128, 2008.
- [22] Gerald M. Edelman and Joseph A. Gally. Degeneracy and complexity in biological systems. *Proc Natl Acad Sci U S A*, 98(24):13763–13768, 2001.

- [23] B. Fain, J. Rudnick, and S. Ostlund. Conformations of linear dna. *Phys. Rev. E*, 55(6):7364, 1997.
- [24] Iman Famili, Radhakrishnan Mahadevan, and Bernhard O. Palsson. k-cone analysis: Determining all candidate values for kinetic parameters on a network scale. *Biophys J*, 88(3):1616–1625, 2005.
- [25] M-A Felix and A Wagner. Robustness and evolution: concepts, insights and challenges from a developmental model system. *Heredity*, 100(2):132–140, 2008.
- [26] W. Fontana. Modelling ‘evo-devo’ with RNA. *Bioessays*, 24(12):1164–1177, 2002.
- [27] Scott Forth, Christopher Deufel, Maxim Y. Sheinin, Bryan Daniels, James P. Sethna, and Michelle D. Wang. Abrupt buckling transition observed during the plectoneme formation of individual dna molecules. *Phys. Rev. Lett.*, 100:148301, April 2008.
- [28] Mark Goulian. Robust control in bacterial regulatory circuits. *Curr Opin Microbiol*, 7(2):198–202, 2004.
- [29] Sergio Grimsbs, Joachim Selbig, Sascha Bulik, Hermann-Georg Holzhutter, and Ralf Steuer. The stability and robustness of metabolic states: identifying stabilizing sites in metabolic networks. *Mol Syst Biol*, 3:146, 2007.
- [30] Ryan N. Gutenkunst, Fergal P. Casey, Joshua J. Waterfall, Christopher R. Myers, and James P. Sethna. Extracting falsifiable predictions from sloppy models. *Ann NY Acad Sci*, 1115(1):203–211, 2007.
- [31] Ryan N. Gutenkunst and James P. Sethna. Adaptive mutation in a geometrical model of chemotype evolution. arXiv.org:0712.3240, 2007.
- [32] Ryan N Gutenkunst, Joshua J Waterfall, Fergal P Casey, Kevin S Brown, Christopher R Myers, and James P Sethna. Universally sloppy parameter sensitivities in systems biology models. *PLoS Comput Biol*, 3(10):e189, 2007.
- [33] Peter Hänggi, Peter Talkner, and Michal Borkovec. Reaction-rate theory: fifty years after kramers. *Rev. Mod. Phys.*, 62(2):251, 1990.
- [34] Christian I. Hong, Emery D. Conrad, and John J. Tyson. A proposal for

- robust temperature compensation of circadian rhythms. *Proc Natl Acad Sci U S A*, 104(4):1195–1200, 2007.
- [35] Nicholas T Ingolia. Topology and robustness in the Drosophila segment polarity network. *PLoS Biol*, 2(6):e123, Jun 2004.
- [36] Erica Jen. Stable or robust? What’s the difference? *Complexity*, 8(3):12–18, January 2003.
- [37] Erica Jen, editor. *Robust Design: A Repertoire of Biological, Ecological, and Engineering Case Studies*. Santa Fe Institute Studies in the Sciences of Complexity. Oxford University Press, 2005.
- [38] J. Kim, D. G. Bates, I. Postlethwaite, L. Ma, and P. A. Iglesias. Robustness analysis of biochemical network models. *IEEE P Syst Biol*, 153(3):96–104, 2006.
- [39] Hiroaki Kitano. Towards a theory of biological robustness. *Mol Syst Biol*, 3:137, 2007.
- [40] Konstantin Klenin, Holger Merlitz, and Jörg Langowski. A brownian dynamics program for the simulation of linear and circular dna and other wormlike chain polyelectrolytes. *Biophys. J.*, 74:780, 1998.
- [41] Daniel A. Koster, Komaraiah Palle, Elisa S. M. Bot, Mary-Ann Bjornsti, and Nynke H. Dekker. Antitumour drugs impede dna uncoiling by topoisomerase i. *Nature*, 448:213, 2007.
- [42] D.C. Krakauer and J.B. Plotkin. Principles and parameters of molecular robustness. In Erica Jen, editor, *Robust Design: A Repertoire of Biological, Ecological, and Engineering Case Studies*, pages 71–104. Oxford University Press, 2005.
- [43] Igor M. Kulić, Hervé Mohrbach, Rochish Thaokar, and Helmut Schiessel. Equation of state of looped dna. *Phys. Rev. E*, 75:011913, 2007.
- [44] Hiroyuki Kurata, Hana El-Samad, Rei Iwasaki, Hisao Ohtake, John C. Doyle, Irina Grigorova, Carol A. Gross, and Mustafa Khammash. Module-based analysis of robustness tradeoffs in the heat shock response system. *PLoS Comput Biol*, 2(7):e59, 2006.
- [45] Richard E. Lenski, Jeffrey E. Barrick, and Charles Ofria. Balancing robustness and evolvability. *PLoS Biol*, 4(12):e428, 2006.

- [46] W. Liebermeister and E. Klipp. Biochemical networks with uncertain parameters. *IEE P Syst Biol*, 152(3):97–107, 2005.
- [47] Wenzhe Ma, Luhua Lai, Qi Ouyang, and Chao Tang. Robustness and modular design of the Drosophila segment polarity network. *Mol Syst Biol*, 2:70, 2006.
- [48] J. F. Marko and E. D. Siggia. Statistical mechanics of supercoiled dna. *Phys. Rev. E*, 52(3):2912, September 1995.
- [49] John F. Marko. Torque and dynamics of linking number relaxation in stretched supercoiled dna. *Phys. Rev. E*, 76:021926, August 2007.
- [50] John F. Marko. Micromechanics of single supercoiled dna molecules. *Proceedings of the Institute of Mathematics and its Applications*, :in press, 2009.
- [51] John F. Marko and Eric D. Siggia. Stretching dna. *Macromolecules*, 28:8759–8770, 1995.
- [52] Eli Meir, Edwin M. Munro, Garrett M. Odell, and George Von Dassow. In-geneue: A versatile tool for reconstituting genetic networks, with examples from the segment polarity network. *J Exp Zool*, 294(3):216–251, 2002.
- [53] J. D. Moroz and P. C. Nelson. Entropic elasticity of twist-storing polymers. *Macromolecules*, 31:6333, 1998.
- [54] J. David Moroz and Philip Nelson. Torsional directed walks, entropic elasticity, and dna twist stiffness. *Proc. Natl. Acad. Sci. USA*, 94(26):14418–14422, December 1997.
- [55] Cornel Mülhardt. *Molecular Biology and Genomics*. Academic Press, 2006.
- [56] Christopher R. Myers. Satisfiability, sequence niches, and molecular codes in cellular signaling. arXiv/q-bio/0702042, 2007.
- [57] Christopher R. Myers, Ryan N. Gutenkunst, and James P. Sethna. Python unleashed on systems biology. *Comput Sci Eng*, 9(3):34–37, 2007.
- [58] Philip Nelson. Sequence-disorder effects on dna entropic elasticity. *Phys. Rev. Lett.*, 80(26):5810, 1998.
- [59] Sébastien Neukirch. Extracting dna twist rigidity from experimental supercoiling data. *Phys. Rev. Lett.*, 93(19):198107, November 2004.

- [60] Theo Odijk. Dna in a liquid-crystalline environment: Tight bends, rings, supercoils. *J. Chem. Phys.*, 105(3):1270, 1996.
- [61] Matthew Piazza, Xiao-Jiang Feng, Joshua D. Rabinowitz, and Herschel Rabitz. Diverse metabolic model parameters generate similar methionine cycle dynamics. *J Theor Biol*, 251(4):628–639, April 2008.
- [62] Colin S. Pittendrigh. On temperature independence in the clock system controlling emergence time in *Drosophila*. *Proc Natl Acad Sci U S A*, 40(10):1018–1029, 1954.
- [63] Jens Rotne and Stephen Prager. Variational treatment of hydrodynamic interaction in polymers. *J. Chem. Phys.*, 50(11):4831, 1969.
- [64] P Ruoff, L Rensing, R Kommedal, and S Mohsenzadeh. Modeling temperature compensation in chemical and biological oscillators. *Chronobiol Int*, 14(5):499–510, 1997.
- [65] Peter Schuster and Walter Fontana. Chance and necessity in evolution: lessons from rna. *Physica D*, 133(1-4):427–452, 1999.
- [66] Jiro Shimada and Hiromi Yamakawa. Ring-closure probabilities for twisted wormlike chains. application to dna. *Macromolecules*, 17:689, 1984.
- [67] Jorg Stelling, Uwe Sauer, Zoltan Szallasi, Francis J. Doyle, and John Doyle. Robustness of cellular functions. *Cell*, 118(6):675–685, 2004.
- [68] Ralf Steuer, Thilo Gross, Joachim Selbig, and Bernd Blasius. Structural kinetic modeling of metabolic networks. *Proc Natl Acad Sci U S A*, 103(32):11868–11873, 2006.
- [69] T. R. Strick, J.-F. Allemand, D. Bensimon, A. Bensimon, and V. Croquette. The elasticity of a single supercoiled dna molecule. *Science*, 271(5257):1835, 1996.
- [70] Sumedha, Olivier C. Martin, and Andreas Wagner. New structural variation in evolutionary searches of RNA neutral networks. *Biosystems*, 90(2):475–485, 2007.
- [71] Alexei V. Tkachenko. Role of boundary constraints in dna cyclization. arXiv.org:q-bio/0703026, 2007.

- [72] Jun Tomita, Masato Nakajima, Takao Kondo, and Hideo Iwasaki. No transcription-translation feedback in circadian rhythm of KaiC phosphorylation. *Science*, 307(5707):251–254, 2005.
- [73] E. N. Trifonov, R. K.-Z. Tan, and S. C. Harvey. In W. K. Olson, M. H. Sarma, and M. Sundaralingam, editors, *DNA Bending and Curvature*, pages 243–254. Adenine Press, 1987.
- [74] G. H. M. van der Heijden, S. Neukirch, V. G. A. Goss, and J. M. T. Thompson. Instability and self-contact phenomena in the writhing of clamped rods. *Int. J. Mech. Sci.*, 45:161, 2003.
- [75] Jeroen S. van Zon, David K. Lubensky, Pim R. H. Altena, and Pieter Rein ten Wolde. An allosteric model of circadian KaiC phosphorylation. *Proc Natl Acad Sci U S A*, 104(18):7420–7425, 2007.
- [76] Maria Vologodskiaia and Alexander Vologodskii. Contribution of the intrinsic curvature to measured dna persistence length. *J. Mol. Biol.*, 317:205, 2002.
- [77] Alexander V. Vologodskii and John F. Marko. Extension of torsionally stressed dna by external force. *Biophys. J.*, 73:123, 1997.
- [78] George von Dassow, Eli Meir, Edwin M. Munro, and Garrett M. Odell. The segment polarity network is a robust developmental module. *Nature*, 406(6792):188–192, 2000.
- [79] A. Wagner. *Robustness and Evolvability in Living Systems*. Princeton University Press, 2005.
- [80] Andreas Wagner. Robustness and evolvability: a paradox resolved. *Proc R Soc Lond B Biol Sci*, 275(1630):91–100, 2008.
- [81] Michelle D. Wang, Hong Yin, Robert Landick, Jeff Gelles, and Steven M. Block. Stretching dna with optical tweezers. *Biophys. J.*, 72:1335, 1997.
- [82] Joshua J. Waterfall, Fergal P. Casey, Ryan N. Gutenkunst, Kevin S. Brown, Christopher R. Myers, Piet W. Brouwer, Veit Elser, and James P. Sethna. Sloppy-model universality class and the Vandermonde matrix. *Phys Rev Lett*, 97(15):150601, 2006.
- [83] Tau-Mu Yi, Yun Huang, Melvin I. Simon, and John Doyle. Robust perfect

adaptation in bacterial chemotaxis through integral feedback control. *Proc Natl Acad Sci U S A*, 97(9):4649–4653, 2000.